Thèse de doctorat

Université de Limoges

Université de Limoges

ED 653 - Sciences et Ingénierie (SI)

Institut de Recherche sur les Céramiques - IRCER

Thèse pour obtenir le grade de

Docteur de l'Université de Limoges

Matériaux Céramiques et Traitements de Surface

Présentée et soutenue par

María Catalina GALEANO CAMACHO

Le 16 décembre 2025

SYNTHÈSE DE CÉRAMIQUES ET ÉLABORATION DE REVÊTEMENTS À BASE DE ZIRCONE POUR APPLICATIONS EN BARRIÈRES THERMIQUES

Thèse dirigée par **Hélène AGEORGES et Juan MUÑOZ**

JURY :

Rapporteurs

Marie Pierre PLANCHE, Full professor Université Technologique de Belfort-Montbéliard

Juan ZÁRATE MEDINA, Full professor, UMSNH

José de Jesús PÉREZ BUENO, Full profesor, CIDETEQ

Examinateurs

Juan MUÑOZ SALDAÑA, Full profesor, CINVESTAV

Hélène AGEORGES, Associate professor, Université de Limoges

Astrid Lorena GIRALDO BETANCUR, Full profesor, CINVESTAV

Jesús GONZÁLEZ HERNÁNDEZ, Full professor, CINVESTAV

Fabio VARGAS GALVIS, Full professor, Universidad de Antioquia

Invités

Julie BOURRET. Associate professor, IRCER

Droits d’auteurs

Cette création est mise à disposition selon le Contrat :
« **Attribution-Pas d'Utilisation Commerciale-Pas de modification 4.0 France** »
disponible en ligne https://creativecommons.org/licenses/by-nc-nd/4.0



Licence CC BY-NC-ND 4.0

Aknowledges

I gratefully acknowledge the financial support from Secretaría de Ciencia, Humanidades, Tecnología e Innovación, (SECIHTI), which allowed me to pursue my studies under the same conditions as national students.

This work was additionally supported by the French National Research Agency (ANR) under the Investments for the Future Program, reference ANR-18-EURE-0017 TACTIC.

My deepest gratitude to CINVESTAV, which for the past eight years has seen me walking its halls between my master's and doctoral degrees, for giving me all the academic and financial tools I need to face the academic world with excellence. I would like to thank the laboratories LIDTRA and CENAPROT, and especially Ing. Eleazar Urbina and Ing. Liliana Naranjo, for their technical assistance and collaboration throughout this project. Many thanks to Dr. Emma Santillán from the CINVESTAV unit library, who tirelessly supported me throughout the thesis review process. My gratitude extends to the University of Limoges, IRCER laboratory and the entire team for providing the resources and environment needed to carry out this research. I am especially thankful to Geoffroy Rivaud for his guidance during the spraying experiments.

My sincere appreciation goes to my advisors, Dr. Hélène Ageorges and Dr. Juan Muñoz. Thank you for your guidance, patience, and trust during these years. This was a demanding and transformative experience, and I am completely sure I could not have completed it without your support. I am especially thankful to Dr. Juan for standing beside me during the hardest moments and for believing in me wholeheartedly, and to Dr. Hélène once again for welcoming me into her group and allowing me to experience French culture, landscapes, and scientific community.

I would also like to thank my committee members, Dr. Astrid Giraldo (for always being ready to listen to me), Dr. Jesús González (for pushing me to do better every time), Dr. Juan Zárate, and Dr. José de Jesús Pérez, for your time, feedback, and continuous encouragement. Their contributions strengthened this work in meaningful ways.

Thanks to my team at CENAPROT, where I found a support network that has also brought me where I am today. Thank you for all the laughter and learning together.

Thanks to my friends Sugey, Deimer, and Dorian, who, with their care and attention, have taught me that friendship has no boundaries, no time limits, and no schedules.

To the friends I met in France, thank you for making this experience meaningful. To my “chicas del cable” Xime, Cami, and Caro, thank you for being my family away from home and for lifting me up whenever I needed it. To Cris and Mossaab, my unconditional friends and Solange, thank you for your motherly welcome, kindness, and generosity.

Thanks to Arkansas State University for being part of the final steps of this journey. Special thanks to my friend Charly, who in recent months has motivated me to reach the next level and has believed in me more than I have believed in myself. I am equally grateful to my friends in México especially Lily and Oscar, who have welcomed me as if I were part of their family since I first set foot on Mexican lands and my friends in Colombia for their support, patience, and love across distances.

I am deeply grateful to my family for their constant support. To my parents, thank you for believing in me unconditionally and for encouraging me every step of the way. To my siblings, thank you for keeping me grounded and for reminding me who I am throughout this challenging process.

Last but not least, I want to thank God. His strength and guidance sustained me through every stage of this journey, especially in the moments when I felt close to giving up.

To everyone who was part of this journey and I didn’t mention, thank you.

Dedication

To all the versions of me that died along the way, and to those that were born with more spirit.

Resumen

Las turbinas de gas utilizadas en los sectores del transporte, la defensa y la energía utilizan recubrimientos de barrera térmica (RBT) para proteger los componentes metálicos expuestos a condiciones de alta temperatura. Esta tesis se centra en la síntesis, la caracterización y el depósito de cerámicos base zirconia, con el objetivo de optimizar su desempeño en aplicaciones de barreras térmicas. El trabajo se divide en dos secciones. La primera aborda el desarrollo de cerámicos densos, desde la síntesis del sistema ternario ZrO_2-Y_2O_3-Ta_2O_5 (YTZ) hasta su caracterización microestructural, mecánica y térmica. La segunda se enfoca en el rociado y evaluación de recubrimientos depositados mediante plasma por suspensión (SPS) y su resistencia a altas temperaturas.

Para los cerámicos densos, se seleccionaron cinco composiciones del sistema ZrO_2-xY_2O_3-xTa_2O_5 (donde x = 15.4, 16, 16.6, 17.2 y 17.8% mol) dentro de la región de fase tetragonal no transformable (*t'*) del sistema YTZ. Los polvos precursores se caracterizaron mediante tamaño de partícula, difracción de rayos X (DRX) y microscopía electrónica de barrido (MEB). Posteriormente, se activaron mecánicamente mediante un molino planetario (240 RPM, 12 horas) y un molino de alta energía Emax (1700 RPM, 20 minutos), para luego llevar a cabo la compactación de los polvos en una prensa uniaxial para la obtención de los cerámicos. Estos se llevan a 1500 °C por 2 y 20 horas en un horno de alta temperatura para promover la formación de la fase *t'*. La activación de los polvos con Emax demostró ser más eficiente, promoviendo la formación de la fase *t'* en menor tiempo. Los cerámicos se evaluaron mediante DRX, MEB, Raman, micro/nanodureza, tenacidad a fractura, ferroelasticidad y conductividad térmica.

Finalmente, se seleccionó una composición (16% mol de Y_2O_3 y Ta_2O_5) para los recubrimientos y se utilizaron suspensiones preparadas con polvo activado por Emax. El proceso SPS se llevó a cabo sobre sustratos de acero inoxidable 304L, utilizando distancias de rociado entre 60 y 80 mm y Ar/He como gases formadores. Los recubrimientos depositados a 60 mm presentaron porosidades inferiores al 5%, con una tasa de depósito de 33 µm/min.

Palabras clave: Fase tetragonal no transformable, Mecanoactivación, Plasma por suspensión, Recubrimientos de barreras térmicas, Zirconia-itria-tantala.

Abstract

Gas turbines used in the transportation, defense and energy sectors use thermal barrier coatings (TBCs) to protect metallic components exposed to high temperature conditions. This thesis focuses on the synthesis, deposit and analysis of the high temperature behavior of zirconia-based dense ceramics and coatings, with the objective of optimizing their performance in thermal barrier applications.

The work is divided into two main sections. The first one is about the development of dense ceramics, from the synthesis of the ZrO_2-Y_2O_3-Ta_2O_5 (YTZ) ternary system to its microstructural, mechanical and thermal characterization. The second focuses on the deposit and evaluation of coatings developed by suspension plasma spray (SPS) and their resistance to high temperatures.

For dense ceramics, five compositions of the ZrO_2-xY_2O_3-xTa_2O_5 system (where x = 15.4, 16, 16.6, 16.6, 17.2 and 17.8% mol) were selected within the non-transformable tetragonal phase region (*t'*) of the YTZ system. The precursor powders were initially characterized by particle size, X-ray diffraction (XRD) and scanning electron microscopy (SEM). Subsequently, mechanically activated by a planetary ball mill (240 RPM, 12 h) and a high-energy ball mill, Emax, (1700 RPM, 20 min). Then, the powders were used to obtain densified samples through sintering at 1500 °C for 2 and 20 h in a high temperature furnace to promote the formation of the *t'*-phase. The activation of the powders with Emax showed to be more efficient, promoting the formation of the *t'*-phase in less time. Dense ceramics were evaluated by XRD, SEM, Raman, micro/nanohardness, fracture toughness, ferroelastic behavior and thermal conductivity.

Finally, for the coatings, one composition (16% mol of Y_2O_3 and Ta_2O_5) was selected and suspensions prepared with Emax activated powder were used. The SPS process was carried out on 304L stainless steel substrates, using spray distances between 60 and 80 mm and Ar/He as forming gases. Coatings deposited at a stand-off distance of 60 mm showed porosities below 5%, with a deposition rate of 33 μm/min.

Keywords: Mechanoactivation, Non-transformable tetragonal phase, Suspension plasma spraying, Thermal barrier coatings, Zirconia-yttria-tantala.

Résumé

Les turbines à gaz utilisées dans les secteurs du transport, de la défense et de l'énergie emploient des revêtements à barrière thermique (TBC) afin de protéger les composants métalliques exposés à des conditions de hautes températures. Cette thèse porte sur la synthèse, le dépôt et l'analyse du comportement à haute température de céramiques denses et de revêtements à base de zircone, dans le but d'optimiser leurs performances pour les applications de barrières thermiques. Le travail est divisé en deux grandes parties. La première concerne le développement de céramiques denses, depuis la synthèse du système ternaire ZrO_2–Y_2O_3–Ta_2O_5 (YTZ) jusqu'à sa caractérisation microstructurale, mécanique et thermique. La seconde partie est consacrée à la réalisation et à l'évaluation de revêtements obtenus par projection plasma de suspension (SPS) et à leur résistance aux hautes températures.

Pour les céramiques denses, cinq compositions du système ZrO_2–xY_2O_3–xTa_2O_5 (où x = 15,4 ; 16 ; 16,6 ; 17,2 et 17,8 % mol) ont été sélectionnées dans la région de la phase tétragonale non transformable (t') du système YTZ. Les poudres précurseurs ont d'abord été caractérisées en termes de taille de particules, de diffraction des rayons X (DRX) et de microscopie électronique à balayage (MEB). Elles ont ensuite été activées mécaniquement à l'aide d'un broyeur planétaire à billes (240 tr/min, 12 heures) et d'un broyeur à haute énergie Emax (1700 tr/min, 20 min). Ces poudres ont été utilisées pour obtenir des échantillons densifiés par frittage à 1500 °C pendant 2 et 20 heures dans un four à haute température, afin de favoriser la formation de la phase *t'*. L'activation des poudres avec le broyeur Emax s'est révélée plus efficace, favorisant la formation de la phase *t'*en un temps réduit. Les céramiques denses ont été évaluées par DRX, MEB, spectroscopie Raman, micro/nanodureté, ténacité à la rupture, comportement ferroélastique et conductivité thermique.

Concernant les revêtements, une composition (16 % mol de Y_2O_3 et Ta_2O_5) a été sélectionnée, et les suspensions préparées à partir des poudres activées par Emax ont été utilisées. Le procédé SPS a été utilisé pour réaliser les revêtements sur des substrats en acier inoxydable 304L, avec des distances de projection comprises entre 60 et 80 mm et un mélange de gaz Ar/He comme gaz plasmagène. Les

revêtements déposés à 60 mm ont présenté des porosités inférieures à 5 %, avec une vitesse de dépôt de 33 µm/min.

Mots clés : Mécano-activation, Phase tétragonale non transformable, Projection plasma de suspension, Revêtements pour barrière thermique, Zircone-yttrium-tantale.

TABLE OF CONTENTS

Aknowledges ..... **iii**
Dedication ..... **v**
Resumen ..... **vi**
Abstract ..... **vii**
Résumé ..... **viii**
List of Tables ..... **xiii**
List of Figures ..... **xiv**
Abbreviations ..... **xix**
Introduction **1**
Justification **4**
Objectives **5**
General objective 5
Specific objectives 5
Hypothesis **6**
CHAPTER 1: Background **7**
1.1. Zirconia: structure, polymorphism and fundamental characteristics 9
1.1.1. Crystal structure and polymorphic forms 9
1.1.2. Thermodynamics and phase transformation mechanisms 10
1.1.3. Physical and chemical properties of pure zirconia 11
1.2. Phase stabilization and dopant mechanisms 13
1.2.1. Yttria-stabilized zirconia (YSZ) 13
1.2.2. Role of pentavalent dopants (Ta^{5+}, Nb^{5+}, etc.) 15
1.2.3. The ZrO_2–Y_2O_3–Ta_2O_5 (YTZ) system 17
1.3. Microstructural Control and Mechanical Behavior in Tetragonal Zirconia Systems 21
1.3.1. Microstructural stability and its influence 21
1.3.2. Mechanoactivation of powders 22
1.3.2.1. Planetary ball milling 23
1.3.2.2. High energy ball milling 24
1.3.3. Ferroelasticity and toughening mechanisms 27
1.4. Zirconia-based ceramics for thermal barrier coatings (TBCs) 30

1.4.1. Thermal barrier coatings and their requirements 30
1.4.2. Thermal Spray Techniques 32
1.4.2.1. Suspension Plasma Spraying (SPS) 35
CHAPTER 2: Experimental procedure 38
2.1. Synthesis and characterization of ZrO_2-Y_2O_3-Ta_2O_5 dense ceramics 40
2.1.1. Powder milling, pressing and sintering of dense ceramics 40
2.1.2. Microstructural analysis 42
2.1.3. Mechanical analysis 43
2.1.4. Thermal properties 46
2.2. Plasma spraying coatings of YTZ systems 47
2.3. Samples nomenclature 51
CHAPTER 3: Results – Characterization of raw materials 52
3.1. Characterization of the precursors ZrO_2, Y_2O_3 and Ta_2O_5 54
3.2. Characterization of YTZ powders compositions used for dense ceramics 58
CHAPTER 4: Results – Dense ceramics 69
4.1. Characterization of YTZ dense ceramics 71
4.1.1. Microstructural properties of YTZ system 71
4.1.2. Mechanical properties of YTZ system 84
4.1.3. Thermal properties of YTZ system 100
CHAPTER 5: Results – Coatings 104
5.1. Characterization of the substrate 106
5.2. Preliminary deposition trials using YSZ coatings 107
5.3. Phase stability and microstructure of 16YTZ coatings 110
LIMITATIONS AND FUTURE WORKS 116
CONCLUSIONS 118
REFERENCES 121
ANNEXES 133
ANNEX 1 139
ANNEX 2 134
ANNEX 3 139
VITA OF MARIA CATALINA GALEANO CAMACHO 141

List of Tables

Table 1.1 Summary of properties of pure zirconia (ZrO_2) reported in the literature ...12
Table 1.2 Comparison between Planetary Ball Milling and High-Energy Ball Milling. (Data summarized from Retsch, The Art of Milling).....26
Table 2.1. Conditions used for sintering samples at 1500 °C. 41
Table 2.2 Plasma spraying parameters used in this project. 50
Table 2.3 Conversion of molar scale from ZrO_2-$YO_{1.5}$-$TaO_{2.5}$ Ternary phase diagram to $YTaO_4$-ZrO_2 quasi-binary phase diagram. 51
Table 3.1. Particle size values calculated from SEM micrographs and particle size distribution of precursor powders without preheating and preheated to 1000 °C. 57
Table 3.2. Mass percentages of each phase present in the 16YTZ composition before sintering. 59
Table 3.3. Mass percentages of each phase present in the 16YTZ composition and lattice parameters after sintering. 61
Table 3.4. High-energy ball milling conditions for 16YTZ powders, mass percentages of each phase present in the four samples and milling times before sintering and GOF of the refinement. 65
Table 3.5. Comparison of milling conditions and particle size distribution of powders obtained by conventional and high-energy ball milling 67
Table 4.1 Apparent density, apparent solid density, open porosity, and theoretical density (XRD) of the sintered dense ceramics. 75
Table 4.2 Characteristic tetragonal peaks in the Raman spectra of 16P1, 16P2, 16P20 ceramics and their vibrational modes 83
Table 5.1 Experimental parameters used for the preliminary YSZ coatings deposited from suspensions prepared with commercial YSZ powder. 108
Table 5.2 Characteristics of the coatings obtained using 16E30 and 16E40 powder feedstock 111
Table A1.1.1 Structural information used for the Rietveld refinement 134
Table A1.1.2 Modified structural information for 16YTZ, according to ZrO_2 tetragonal 134
Table A1.1.3 Structural information for ZrO_2, Cubic (Y-Doped) 135
Table A1.1.4 Structural information for ZrO_2, Monoclinic 135
Table A1.1.5 Structural information for Y_2O_3. Cubic 135
Table A1.1.6 Structural information for Ta_2O_5, Orthorhombic 135
Table A1.2.1 Parameters obtained in Rietveld refinement for dense ceramics (16P1, 16P2 and 16P20) and for coatings (A1, B2, B2 and B3). 138
Table A2.1 Mass percentages of each phase present in the 16YTZ composition after sintering at 2 and 8 h at 1500 °C. 140

List of Figures

Figure 1.1 Crystal structures of zirconia polymorphs and their temperature stability ranges. The monoclinic phase is stable below 850 °C, the tetragonal phase between approximately 1150 °C and 2370 °C, and the cubic fluorite structure above 2370 °C 9
Figure 1.2 ZrO_2-Y_2O_3 phase diagram (wt.%) 14
Figure 1.3 Phase diagram of ZrO_2–Y_2O_3–Ta_2O_5 showing the extended t′ field, where it can be observed that with equimolar amounts of $YO_{1.5}$ and $TaO_{2.5}$ in a range between 14-18 mol%, a *t′*-phase can be obtained (the area marked with red dotted lines).....18
Figure 1.4 SEM micrographs comparing (a) YTZ and (b) YSZ microstructures after annealing at ~1500 °C.....19
Figure 1.5 Thermal conductivity as a function of temperature for YSZ and YTZ compositions, showing the lower and more stable thermal conductivity of YTZ even after long-term annealing (samples indicated with dotted lines) 20
Figure 1.6 Schematic representation of stress distribution as a function of grain morphology in tetragonal zirconia. (a) Fine, equiaxed grains show homogeneous stress fields that promote ferroelastic domain stability. (b) Elongated grains generate localized stress concentrations that facilitate domain switching or *t* → *m* transformation. 22
Figure 1.7 Schematic representation of the planetary ball milling process, showing the generation of centrifugal forces, powder movement, and successive stages of fracturing and welding leading to homogeneous submicrometric powders 24
Figure 1.8 Schematic representation of the motion pattern in the Emax high-energy ball mill. The jars follow a circular trajectory controlled by two synchronized discs, generating simultaneous impact and shear forces through their oval geometry. This configuration results in high-frequency collisions, efficient frictional mixing, and uniform mechanical activation of zirconia-based powders.....25
Figure 1.9 Illustration of ferroelastic domain reorientation and local strain accommodation near a crack tip in tetragonal zirconia. Domain switching and limited transformation contribute to stress relaxation and crack-tip shielding. 27
Figure 1.10 (a) Schematic of a ferroelastic process zone near a crack tip. (b) Corresponding stress–strain curve showing the hysteretic response of *t′*-YSZ during domain nucleation and switching. The mechanism activates when shear stress ($\boldsymbol{\tau}$) exceeds the critical stress ($\boldsymbol{\tau T}$), generating a permanent shear strain ($\boldsymbol{\gamma T}$). [59].....28
Figure 1.11 Schematic representation of a typical thermal barrier coating system showing the superalloy, bond coat, thermally grown oxide (TGO), and ceramic topcoat.....31
Figure 1.12 Main design and performance requirements for ceramic topcoats in TBCs 32

Figure 1.13 Representation of a general thermal spray process. The spray torch converts chemical or electrical energy into a high-temperature gas stream that melts and propels the coating material toward the substrate 33
Figure 1.14 Schematic comparison of topcoat typical microstructures produced by APS, SPS, and EB-PVD processes. APS yields a lamellar splat structure, SPS produces a feather-like or columnar morphology depending on parameters, and EB-PVD forms highly oriented columnar grains 34
Figure 1.15 Schematic of the Suspension Plasma Spraying (SPS) process showing the injection of a liquid suspension into a plasma jet. Molten particles impact the substrate and form the coating 35
Figure 1.16 Cross-section and top-view BSE micrographs of a typical SPS coating showing columnar growth (left) and the topographical surface morphology characterized by cauliflower-like clusters and merged microfractal structures (right).....36
Figure 2.1. Overview of the development of the project.....39
Figure 2.2. Experimental steps for obtaining and characterizing the dense ceramics developed in this project.....41
Figure 2.3 Methodology for obtaining and characterizing coatings. 47
Figure 2.4 a) SinplexPro cascaded arc design and, b) plasma torch scheme 48
Figure 2.5 Suspension injection system used in this project.....49
Figure 3.1. Scheme of the development of this chapter.....53
Figure 3.2. X-ray diffraction patterns of precursors without and with preheating at 1000 °C (a, d) ZrO_2, (b, e) Y_2O_3, and (c, f) Ta_2O_5. 54
Figure 3.3. SEM micrographs and particle size distribution of precursors without and with preheating at 1000 °C. 56
Figure 3.4. XRD patterns of a) 16M and, b) 16PM identifying their respective phases after planetary ball milling process. 58
Figure 3.5. XRD of a) 16MC and b)16PMC sintered at 1500 °C for 20 h in a chamber furnace. 60
Figure 3.6. Particle size distribution in volume percentage of the five different compositions of YTZ.....62
Figure 3.7. XRD patterns of (a) the five different compositions in powder, (b) highlights of the characteristic peaks corresponding to *t'*-phase,(c) tetragonal lattice characteristic of a *t'*-system representing the random occupancy of Y^{3+} and Ta^{5+} ions into Zr^{4+} places, and (d) tetragonality and lattice parameters of *t'*-phase in 15.4, 16, 16.6, 17.2 and 17.8PMC samples. 63
Figure 3.8. XRD patterns of the samples analyzed with the composition of 16YTZ milled by high-energy ball milling (Emax) at different powder vial filling volumes and milling times without sintering. 65
Figure 3.9. XRD patterns of powders milled by high-energy ball milling: (a) comparison of sintering times (2 h and 20 h) to evaluate *t'*-phase formation; (b) effect of milling time (10 min vs 20 min) on 16YTZ composition; (c) XRD patterns and (d) size distribution showing the influence of powder volume in the vial (30% and 40% vol.) on mechanoactivation efficiency.....66
Figure 4.1 Scheme of the development of the results for dense ceramics. 70
Figure 4.2 XRD analysis of 15.4P1, 16P1, 16.6P1, 17.2P1 and 17.8P1 dense samples. (a) XRD patterns; the characteristic peaks corresponding to *t'*-phase are

highlighted in (b), (c) tetragonality and % *t'*-phase, and (d) lattice parameters of *t'*-phase in 15.4P1, 16P1, 16.6P1, 17.2P1 and 17.8P1. 71
Figure 4.3 Microstructure of samples a) 15.4P1, b) 16P1, c) 16.6P1, d) 17.2P1 and e) 17.8P1 with their respective grain size distribution and standard deviation; and f) is the average grain size for all compositions, showing an increasing trend with the increment of dopants. 74
Figure 4.4 a) Raman spectra of the five compositions of YTZ recorded at room temperature after sintering at 1500 °C for 20 h and, b) Deconvolution of Raman spectra in the 5 different bands found in *t'*-phase for the five compositions. 76
Figure 4.5 a) Phase distribution and crystallographic orientation maps obtained by EBSD for 15.4P1 and 17.2P1 and b) Comparison between grain sizes obtained by SEM and those obtained by EBSD. 77
Figure 4.6 AFM images of the polished surface of a) 15.4P1 and b) 17.2P1 dense ceramics showing the microstructure through the topography reconstruction of mechanochemically polished surfaces. 79
Figure 4.7 XRD patterns of (a) 16P1, 16P2, and 16P20 dense samples. Moreover, (b) highlights the characteristic peaks corresponding to *t'*-phase, (c) tetragonality and % *t'*-phase, and (d) lattice parameters of *t'*-phase in 16P1, 16P2, and 16P20. 80
Figure 4.8 Microstructure of samples (a) 16P1, (b) 16P2, and (c) 16P20 with their respective grain size distribution and standard deviation. 82
Figure 4.9 Raman spectra of 16P1, 16P2, and 16P20 recorded at room temperature after sintering at 1500 °C. 83
Figure 4.10 Schematic representation of the Vickers indentation method showing (a) the indentation principle with radial cracks, (b) the top view of the imprint with diagonals and crack lengths used for toughness calculations, and (c) indentation made in one of the samples with the characteristic diagonals of Vicker's method, as a reference. 85
Figure 4.11 Mechanical properties of sintered YTZ ceramics obtained by Vickers microindentation. (a) Hardness as a function of the molar fraction of $YO_{1.5}$ and $TaO_{2.5}$, (b) toughness as a function of load and molar fraction of $YO_{1.5}$ and $TaO_{2.5}$. 86
Figure 4.12 AFM map of the indents in the (a) 15.4P1 and (b) 17.2P1 compositions with the respective 3D reconstruction; (c–d) AFM images of indentation number 1 for the 15.4P1 and 17.2P1 compositions: indent topography and 3D reconstruction with residual depth; (e–f) corresponding load–displacement curves obtained under a load of 9.3 mN. 87
Figure 4.13 AFM of Indentations 1 to 6 performed on the 15.4P1 composition under different applied loads where (a) shows 2D images and 3D reconstructions of each imprint highlighting their geometry and, (b) the corresponding height profiles displaying h_f. 90
Figure 4.14 AFM of Indentations 1 to 6 performed on the 17.2P1 composition under different applied loads where (a) shows 2D images and 3D reconstructions of each imprint highlighting their geometry and, (b) the corresponding height profiles displaying h_f. 91

Figure 4.15 Load–displacement (P–h) curves obtained by nanoindentation at different locations on the 15.4P1 and 17.2P1 compositions. Variations in penetration depth and loading slope reflect the influence of local microstructural heterogeneity, whereas the *pop-in* events indicate sudden transitions in the deformation regime associated with the activation of plastic, ferroelastic or fracture mechanisms. 92
Figure 4.16 Summary of results for hardness and reduced modulus of elasticity as a function of contact penetration depth determined by the Oliver and Pharr method for (a) 15.4P1 and (b) 17.2P1 samples. 94
Figure 4.17 Weibull plots of hardness and reduced elastic modulus results for (a) 15.4P1 and (b) 17.2P1 samples. 95
Figure 4.18 Load-displacement curves at the loading stage for (a) 15.4P1 and (b) 17.2P1 samples. Analysis is focused on regions of the appearance of the first pop-in for quantifying the nature of this transition region when compared with a simulated curve using the Hertz equation of a spherical tip. 97
Figure 4.19 Experimental correlations of a) extra penetration (h_x) and b) crack length ($\boldsymbol{c}$) as a function of $\boldsymbol{P2/3}$ for 15.4P1 and 17.2P1 compositions used to determine the empirical constant Q. 99
Figure 4.20 Thermal properties of the YTZ system evaluated at 25, 100, and 200 °C for the five compositions: (a) thermal diffusivity; (b) thermal conductivity including 7YSZ as a reference; (c) C_p as a function of temperature; and (d) Cp as a function of ZrO_2 content. 101
Figure 4.21 Thermal properties of the YTZ system are evaluated from 25 to 1000 °C for the five compositions: (a) thermal diffusivity; (b) thermal conductivity including 7YSZ as a reference; (c) C_p as a function of temperature; and (d) C_p as a function of ZrO_2 content. 103
Figure 5.1 Scheme of the YTZ coating developed in this chapter. 105
Figure 5.2 XRD pattern of the stainless-steel substrate showing the characteristic peaks of the face-centered cubic (γ) austenitic phase corresponding to AISI 304L. No secondary phases were detected. 106
Figure 5.3 EDS spectrum of the substrate showing the main peaks of Fe, Cr, and Ni, confirming the chemical composition consistent with austenitic stainless-steel grade 304L. 107
Figure 5.4 (a) XRD patterns and (b) cross-sectional SEM micrographs of YSZ coatings deposited under different spraying conditions (samples S1–S5). 109
Figure 5.5 (a) XRD patterns of A1 and B1-B3 coatings obtained by SPS technique, (b) characteristic peaks corresponding to *t'*-phase, (c) values of tetragonality and % *t'*-phase, and (d) lattice parameters of *t'*-phase of A1 and B1-B3 coatings. 112
Figure 5.6 Rietveld refinement of XRD patterns for phases quantification in the coatings: (a) close-up of the fit within the 2θ = 26-30° range, (b) full refinement fit overview, and (c) last peaks of the diffraction pattern to determine the tetragonality of the system and the lattice parameters. 113
Figure 5.7 SEM images of the cross sections of the coatings made by SPS process 114
Figure A1.2.1 XRD patterns of the coatings obtained after adjusting using the Rietveld method 137

Figure A1.2.2 a) Phase quantification (wt.%) in dense ceramics, b) phase quantification (wt.%) in coatings obtained by Rietveld's method. 137
Figure A2.1 Phase composition evolution of 16YTZ after 2 and 8 h of sintering at 1500 °C. In section a) highlights the characteristic peaks between 2θ = 27.5° and 32.5° showing the evolution of the phase contributions between the two sintering times, b) X-ray diffraction patterns and Rietveld refinement results for the 16YTZ ceramic sintered at 1500 °C for 2 h (top) and 8 h (bottom). The color-coded curves correspond to the individual crystalline phases identified in the refinement: t-ZrO_2, m-ZrO_2, c-Y_2O_3, M-$YTaO_4$ and o-Ta_2O_5 and c) Deconvolution of last peaks in the region between 2θ = 71° and 75°, highlighting the presence of minority phases such as c-Y_2O_3, o-Ta_2O_5 and m-ZrO_2 after 2 h. The refinement of the complete XRD patterns confirms that even after 8 h of sintering, considerable quantity of monoclinic phase remain, indicating that full stabilization of the *t'*-phase has not yet been achieved under these conditions. 139
Figure A2.2 Phase quantification (wt.%) in powders sintered at 1500 °C for 2 h and 8 h, based on Rietveld refinement results. The identified crystalline phases include *t*-ZrO_2 (blue), *m*-ZrO_2 (green), *c*-Y_2O_3 (red), *M*-$YTaO_4$ (gold) and *o*-Ta_2O_5 (magenta).....140

Abbreviations

AFM	Atomic Force Microscope
APS	Atmospheric Plasma Spraying
DFT	Density Functional Theroy
EB-PVD	Electron Beam Physical Vapor Deposition
EBSD	Electron Backscatter Diffraction
FIB	Focused Ion Beam
GOF	Goodness of Fit
SEM	Scanning Electron Microscope
SPS	Suspension Plasma Spraying
TBC	Thermal Barrier Coating
TGO	Thermally Grown Oxide
XRD	X-Ray Diffraction

Introduction

Thermal Barrier Coatings (TBCs) are advanced materials applied to protect metallic components in high-temperature environments, such as gas turbines, for aircraft applications or power generation engines [1]. These coatings, whose top layer is a low thermal conductivity ceramic, have as their main functions to thermally insulate and protect the metallic substrate from the high temperatures reached during operation. Simultaneously, TBCs allow to improve the lifetime and performance of components operating in these environments, such as jet engines, where temperatures can reach extreme levels during operating cycles [2], [3].

Ceramic coatings can be based on oxides, carbides, silicide, borides, and nitrides. They can also be of the cermet type or other inorganic material. Ceramic coatings based on oxides are commonly used to increase the oxidation resistance of materials exposed to high temperatures. Alumina (Al_2O_3) and Zirconia (ZrO_2) are the most widely used oxides as thermal barriers since Al_2O_3 oxides have excellent resistance to abrasion and corrosion, and ZrO_2 oxides have very low thermal conductivity [4]. The Zr-based ceramic coatings have been widely researched materials, nor only for their low thermal conductivity but the increasing of the useful life of metallic components [5], [6]. In addition, it has high wear resistance, high melting point and high hardness. However, these Zr-based coatings have limited applications due to their transformation from tetragonal (t) to monoclinic (m) phase when exposed to very high temperatures, which is often accompanied by shear stress and expansion change in volume of approximately 4%, that is not exactly beneficial because fractures can be generated and, therefore, low reliability in the coated components [7]. The t → m phase transformation can be controlled by the addition of suitable materials, usually oxides, which stabilize the zirconia, inhibiting this transformation and eliminating the change in volume [6], [7], [8].

The non-transformable tetragonal phase of zirconia (*t'*-ZrO_2) has several advantages that makes it of interest in various applications due to its properties such as high temperature stability, fracture toughness, low thermal conductivity, among others [9], [10]. Studies over the years have confirmed that the content of 6-8 wt.% yttria stabilizing zirconia (7YSZ) shows excellent behavior by maintaining stable the tetragonal phase and presenting high fracture toughness

[11], [12]. However, 7YSZ has disadvantages such as oxygen vacancies due to the stoichiometry of the system, which limits its operating temperature (<1200°C) for extended exposure times, where phase transformations from tetragonal to tetragonal plus cubic and then to monoclinic occur causing cracks in the coating, sensitivity to corrosion at high temperatures, among other drawbacks [3], [13], [14]. In recent studies, conducted by Abdul-Jabbar et al. [15], the ternary system of zirconia (ZrO_2), yttria (Y_2O_3) and tantala (Ta_2O_5), known as YTZ, especially $YTaO_4$ and ZrO_2 (equimolar amounts of yttria and tantala) has been of great interest because the addition of a pentavalent oxide in specific quantities in the system intrinsically eliminates the conditions for the formation of oxygen vacancies caused by doping with yttria, thus generating stability of the non-transformable tetragonal phase, *t'*, up to about 1500°C, which is a point at which phase stability in the YSZ is compromised. Also, in the study of Gurak et al. [16] about the $YTaO_4$ - ZrO_2 system, they present the pseudo binary phase diagram showing that the tetragonal phase remains stable under thermodynamically stable conditions after cooling in compositions where the amount of $Y_{0.5}Ta_{0.5}O_2$ is in the range between 29 and 36 mol%. Since 2001, Raghavan et al. [17], referred to compositions formed by ZrO_2 - $YTaO_4$ as particularly promising due to their stability at 1500°C and particular corrosion resistance. Furthermore, Shen et al. [18] pointed out that they presented high tetragonality values, which translate into fracture toughness values similar or higher than the well-known 7YSZ and have a particularly low thermal conductivity when transformation to monoclinic zirconia is avoided [3].

Therefore, the YTZ system, being a promising material for thermal barrier applications in gas turbines, requires an appropriate deposition process. One of the most common processes for the deposition of zirconia-based ceramics is the thermal spray by atmospheric plasma spray (APS) process, which is considered one of the most versatile methods, as there are very few materials that cannot be deposited by this process [19]. In addition, the plasma spray process is more affordable than electron beam physical vapor deposition (EB-PVD) since it has a higher deposition rate [20] and in nanostructured TBCs exert better thermal shock resistance and lower thermal conductivity [3], [21]. However, thermal spraying of submicrometric and nanometric particles present a significant challenge, as particle sizes below 5 micrometers require an increase in carrier gas,

which severely disrupts the plasma gas stream and thus reduces the deposition rate. Ultrafine particles often present difficulties in attempting to incorporate into the plasma plume, either by agglomeration issues of fine particles [22], particle bouncing when injected perpendicular to the plume or even evaporation phenomena [23]. This problem can be overcome by injecting the feedstock into a liquid medium, i.e. using a suspension. The suspension plasma spray process (SPS) has the potential to combine advantages such as high stress tolerance, low cost, low thermal conductivity, improved corrosion, and impact resistance of coatings [3], [24], [25].

No references have been found in the literature about the thermal spray coating by SPS of the YTZ system, so the parameters used for YSZ deposition were taken as a reference [3], [26], [27], [28], [29], [30].

This work proposes a feasibility study on the synthesis and characterization of five different compositions (x = 15.4, 16, 16.6, 17.2 and 17.8% in mol) in the region of the phase diagram of the ZrO_2-xY_2O_3-xTa_2O_5 system where the *t'* is found. It also seeks to develop and analyze one of these compositions (x = 16 mol%) for thermal spraying using the suspension plasma spray technique, exploring their potential as thermal barrier materials. A mechanical, microstructural and thermal analysis of dense ceramics and coatings is performed.

Justification

The study of thermal barrier coatings has had a strong impact in recent years due to its direct impact on engineering, particularly in the development of gas turbines. These coatings enhance the efficiency and power of turbines by extending the service life of metallic components through their ability to withstand high operating temperatures and reduce exposure to oxidation and corrosion.

One of the main challenges in this field is identifying materials that combine low thermal conductivity, a high melting point, and stability when facing phase transformations during temperature changes, from ambient to operating conditions. Although zirconia stabilized with 6-8% yttria (ZrO_2-Y_2O_3) exhibits these properties, it has limitations when exposed to temperatures around 1200 °C, allowing CMAS infiltration and phase transformations that lead to volume expansion and crack formation in the coatings.

The addition of oxides such as tantalum oxide (Ta_2O_5) has been shown to improve the tetragonal-to-monoclinic (t → m) transformation temperature, stabilizing the tetragonal phase up to at least 1500 °C. This makes the ternary system ZrO_2-Ta_2O_5-Y_2O_3 (YTZ) very important for further investigations. In addition, the lack of literature regarding the deposit of YTZ by SPS presents a unique opportunity to contribute to the advancement of this technology, with potential applications in high-performance thermal barrier coatings.

Objectives

General objective

To develop and characterize ZrO_2-Ta_2O_5-Y_2O_3 (YTZ) dense ceramics by mechanoactivation and solid-state reaction, and coatings deposited by suspension plasma spray.

Specific objectives

1. **Stage of synthesis and characterization of dense ceramics**

    - To develop the synthesis route of the ternary system YTZ from zirconium, yttrium and tantalum oxides by mechanical milling and solid-state reaction.

    - To analyze the microstructure of the precursors and the synthesized dense ceramics by X-ray diffraction, scanning electron microscopy and RAMAN spectroscopy techniques.

    - To characterize mechanically by micro and nanoindentation, and thermally by laser flash the dense ceramics.

2. **Stage of deposition and characterization of coatings**

    - To develop the suspension with powders mechanoactivated by high-energy ball milling.

    - To determine the appropriate parameters for TBC spraying of the YTZ system using the suspension plasma spray technique.

    - To analyze the microstructure and phase stability of the obtained coatings by X-ray diffraction and scanning electron microscopy.

Hypothesis

The compositions of the ZrO_2–$YO_{1.5}$–$TaO_{2.5}$ system located within the non-transformable tetragonal (t′) region exhibit, in their dense state, a percentage of non-transformable tetragonal phase more than 95%, tetragonalities around of 1.025, and a favorable combination of phase stability, mechanical response, and thermal behavior for high-temperature applications. These intrinsic properties, confirmed in the sintered ceramics, are expected to be retained consistently when the same compositions are used in coating form. Accordingly, when deposited by Suspension Plasma Spray (SPS), these compositions are considered viable thermal-barrier materials, as the characteristics observed in the dense state support their potential performance under high-temperature conditions.

CHAPTER 1: Background

This chapter presents the scientific background necessary to understand the synthesis, structure, and behavior of zirconia-based ceramic materials used for thermal barrier coatings (TBCs). It begins with an overview of the fundamental characteristics of zirconia (ZrO_2), emphasizing its polymorphism and the transformations between monoclinic, tetragonal, and cubic phases. The mechanisms governing these transformations, particularly the martensitic t → m transition and its dependence on grain size, temperature, and interfacial energy, are discussed to establish the basis for phase stabilization strategies.

The following sections describe the role of dopants in stabilizing the tetragonal structure. Yttria (Y_2O_3) acts as a trivalent stabilizer that creates oxygen vacancies, while pentavalent dopants such as tantalum oxide (Ta_2O_5) contribute to charge compensation and reduce defect concentration. Their combined effect enables the formation of the non-transformable tetragonal phase (t′), which exhibits superior thermal stability and mechanical resilience.

The ZrO_2–Y_2O_3–Ta_2O_5 (YTZ) ternary system is analyzed as a promising alternative to conventional YSZ, owing to its higher tetragonality, lower thermal conductivity, and improved resistance to phase transformation. The importance of mechanical activation through planetary and high-energy ball milling is also highlighted, as this process enhances powder reactivity and promotes t′-phase formation.

Finally, the chapter discusses the relationship between microstructure and thermomechanical properties, the influence of ferroelastic mechanisms and phonon scattering on toughness and conductivity, respectively, and the relevance of the Suspension Plasma Spray (SPS) technique as a modern route for obtaining TBCs. Collectively, these concepts establish the theoretical foundation for the experimental work presented in the subsequent chapters.

1.1. Zirconia: structure, polymorphism and fundamental characteristics

1.1.1. Crystal structure and polymorphic forms

Zirconia (ZrO_2) is a refractory ceramic material known for its high melting point (2680 °C), excellent corrosion resistance, and notable mechanical performance at elevated temperatures. A fundamental aspect of its behavior keeps in its polymorphism, which has been extensively studied since the 1960s [31], [32], [33], [34]. Zirconia can crystallize in three main structures: monoclinic (m) with the following crystallographic parameters: a=5.151 Å, b=5.203 Å, c=5.316 Å, and β=99.19°; tetragonal (t) with a=b=5.074 Å, c=5.188 Å, and β=90°; and cubic (c) with a=b=c=5.117 Å, and β=90° [26], whose stability depends primarily on temperature and, to a lesser extent, on pressure and dopant content. As illustrated in Figure 1.1, zirconia undergoes successive phase transformations from the monoclinic to the tetragonal and, finally, to the cubic fluorite-type structure as temperature increases.

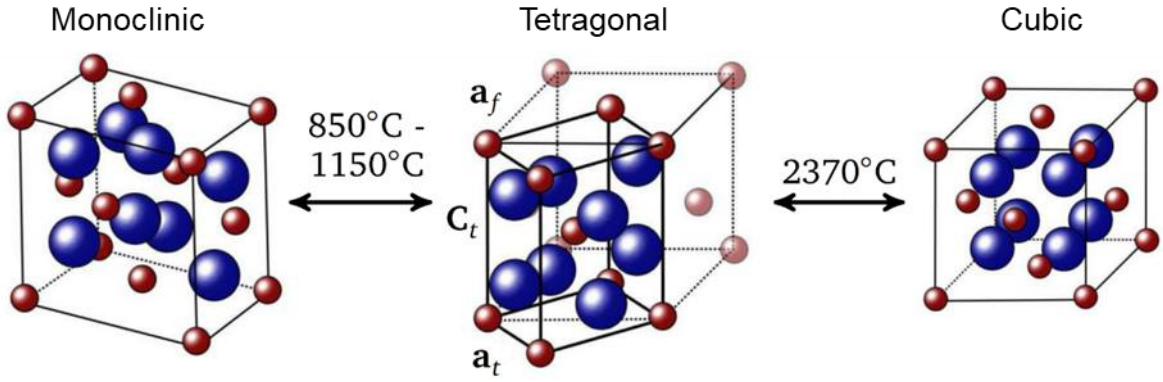


Figure 1.1 Crystal structures of zirconia polymorphs and their temperature stability ranges. The monoclinic phase is stable below 850 °C, the tetragonal phase between approximately 1150 °C and 2370 °C, and the cubic fluorite structure above 2370 °C (Adapted from [26]).

At ambient conditions, zirconia exhibits a monoclinic structure ($P2_1/c$) characterized by distorted oxygen coordination around Zr^{4+} ions [31], [34]. Upon heating above approximately 1150 °C, the material transforms into a tetragonal structure ($P4_2/n\ m\ c$), and further heating beyond 2370 °C leads to the cubic fluorite phase (Fm-3m) [26], [35], [36]. The tetragonal lattice can be represented by rotating the a and b axis by 45°, which allows a more direct comparison between the tetragonal, cubic and monoclinic arrangements when analysis phase transformations. These transformations are reversible upon cooling but involve distinct changes in lattice parameters and density. The tetragonal-to-monoclinic

(t → m) transformation, in particular, is accompanied by a volume expansion of 3–5%, producing local stresses that can cause microcracking if not properly controlled [26], [37].

Crystallographically, the cubic phase is the most symmetric, with oxygen ions occupying tetrahedral interstitial positions, while the tetragonal and monoclinic structures can be understood as successive distortions of this ideal fluorite arrangement [35], [38], [39]. This progression in symmetry explains the observed changes in physical properties, particularly thermal expansion, elastic modulus, and fracture toughness, across the different polymorphs.

In summary, zirconia's polymorphism is a dual feature: it introduces thermal instability in the undoped oxide but also enables toughening mechanisms when the tetragonal phase is stabilized. Understanding these structural relationships provides the basis for the introduction of dopant oxides, which can suppress the deleterious transformation and maintain phase stability at room temperature, as discussed in the following sections.

1.1.2. Thermodynamics and phase transformation mechanisms

The stability of each zirconia polymorph is determined by the balance between thermodynamic and structural factors, primarily temperature, internal energy, and entropy [6]. As temperature increases, the system minimizes its Gibbs free energy by adopting structures of higher symmetry [40]. Consequently, the cubic phase is stable at the highest temperatures, the tetragonal phase dominates at intermediate temperatures, and the monoclinic phase prevails under ambient conditions. This hierarchy in stability has been consistently reported in experimental and theoretical studies of pure and doped zirconia systems [31], [36].

The tetragonal-to-monoclinic (t → m) transformation proceeds through a diffusionless, martensitic pathway driven by a change in lattice free energy. During this process, atoms move cooperatively within the crystal without long-range diffusion, producing a crystallographic shear that accommodates the symmetry change. The transformation occurs rapidly once the thermodynamic barrier is surpassed, and its reversibility upon cooling gives rise to characteristic thermal hysteresis [41], [42], [43].

The t → m transformation is characterized by thermal hysteresis, beginning near 1150 °C on heating and reverting between 600 and 1000 °C during cooling [6], [26]. Within this range, both phases may coexist, generating strain fields that hinder further transformation. The process is therefore athermal: the transformation depends on temperature rather than time. The extent of transformation also depends on crystallite size. Garvie [34] and Heuer et al. [44] demonstrated that grains smaller than approximately 0.3 μm suppress the transformation because the elastic energy required to accommodate the volume expansion exceeds the thermodynamic driving force. Fine-grained zirconia can thus retain the tetragonal phase metastable at room temperature, a phenomenon that forms the basis of transformation toughening.

The relative stability of each phase can also be modified by chemical substitution. The addition of trivalent oxides such as Y_2O_3 introduces oxygen vacancies that lower the free energy of the tetragonal and cubic structures relative to the monoclinic phase. These vacancies act as charge-compensating defects, disrupting the oxygen sublattice and increasing configurational entropy [45]. In contrast, pentavalent dopants such as Ta_2O_5 or Nb_2O_5 tend to compensate existing vacancies, resulting in reduced defect concentrations and enhanced lattice stability at high temperatures [17], [45]. This combination of thermodynamic and defect-chemical effects explains the observed differences in the transformation behavior of co-doped systems such as ZrO_2–Y_2O_3–Ta_2O_5, which exhibit greater phase stability and reduced hysteresis upon cooling.

These thermodynamic principles establish the framework for understanding phase stabilization in zirconia. The addition of dopants, discussed in the following section, further alters the free-energy landscape and extends the stability of the high-temperature phases to lower temperatures.

1.1.3. Physical and chemical properties of pure zirconia

Pure zirconia possesses a combination of thermal, mechanical, and chemical properties that make it one of the most versatile oxide ceramics. Its high melting point (~2700 °C) and low vapor pressure provide excellent thermal stability, while its strong ionic bonds between Zr^{4+} and O^{2-} result in high hardness and stiffness [26], [35], [46]. However, in its undoped form, zirconia suffers from phase instability

and limited fracture toughness due to the spontaneous tetragonal-to-monoclinic transformation upon cooling, as previously discussed. This transformation restricts its direct use in structural or thermal-barrier applications, leading to the development of stabilized zirconias through chemical modification.

Thermally, zirconia exhibits a low thermal conductivity compared to most ceramics, typically between 2–3 $W \cdot m^{-1} \cdot K^{-1}$ at room temperature, decreasing further at elevated temperatures because of phonon scattering caused by mass and strain field fluctuations [17], [47]. This property, together with its high melting point, explains its widespread use as a refractory material and as the base compound for thermal barrier coatings. Its coefficient of thermal expansion (CTE) lies around 10×10^{-6} K^{-1}, close to that of many metallic alloys, which minimizes thermal mismatch in multilayer systems [48], [49]. The most relevant physical and chemical properties of pure zirconia reported in the literature are summarized in Table 1.1, which provides representative values for comparison across polymorphs and operating conditions.

Table 1.1 Summary of properties of pure zirconia (ZrO_2) reported in the literature.

Property	Symbol/Units	Typical value/Range	References
Density	P ($g.cm^{-3}$)	5.83-6.10	[26]
Melting point	T_m (°C)	~2700	[50]
Thermal conductivity	k ($W.m^{-1}.K^{-1}$)	2.0-2.2 (RT)	[51]
Coefficient of thermal expansion	α ($10^{-6}.K^{-1}$)	10.3-10.8	[45]

Mechanically, pure zirconia displays high compressive strength and good wear resistance, but like most oxide ceramics, it is brittle under tensile stress. The fracture strength strongly depends on microstructural factors such as grain size and porosity, and on the presence of residual stresses induced by phase transformations. Controlled stabilization of the tetragonal phase has been shown to significantly improve the work of fracture, making zirconia-based systems suitable for load-bearing and high-temperature applications [52].

Chemically, zirconia is highly stable and corrosion resistant, remaining inert to most acids and alkalis due to its strong ionic-covalent bonding

character [6], [53]. It resists oxidation up to its melting point and shows excellent compatibility with metallic substrates under oxidizing conditions. However, under extreme environments, particularly those containing silicates, sulfates, or molten CMAS (calcium–magnesium–alumino–silicate) deposits, zirconia can partially degrade through interfacial reactions or destabilization of the tetragonal phase [54]. These phenomena are critical for thermal barrier coatings in gas turbine engines and motivate the search for modified zirconia systems with enhanced chemical durability.

Altogether, these characteristics make zirconia an exceptional base material for advanced ceramics. However, to fully exploit its potential, it must be stabilized against phase transformation and chemical degradation, topics explored in the next section through the study of phase stabilization and dopant mechanisms.

1.2. Phase stabilization and dopant mechanisms

1.2.1. Yttria-stabilized zirconia (YSZ)

Among the different stabilizing oxides, yttria (Y_2O_3) has proven to be the most effective in producing thermally and mechanically stable zirconia. The addition of Y^{3+} cations to the Zr^{4+} sublattice generates oxygen vacancies that balance the charge difference, thereby reducing the free energy of the tetragonal and cubic phases relative to the monoclinic form [45], [52]. This defect-compensation mechanism was first described in detail by Scott (1975) [31] and later refined by Subbarao (1981) [53] to explain the stability ranges observed in the ZrO_2–Y_2O_3 phase diagram [55].

The reaction describing the substitutional incorporation of yttrium and the associated creation of oxygen vacancies can be expressed using Kröger–Vink notation as follows:

$$Y_2O_3 \rightarrow 2\,Y'_{Zr} + V_O^{\bullet\bullet} + 3\,O_O^{\times} \qquad (1.1)$$

This equation illustrates that two Y^{3+} ions substitute for two Zr^{4+} sites, generating one doubly charged oxygen vacancy ($V_O^{\bullet\bullet}$) to maintain charge neutrality. $O_O^{\times}$ is a neutral oxygen ion in its lattice position. The resulting defects lower the

Gibbs free energy of the high-symmetry phases, allowing zirconia to retain the tetragonal or cubic structure at lower temperatures [17], [31], [56].

At compositions between 3 and 13 wt.% Y_2O_3, zirconia forms a partially stabilized structure consisting of fine tetragonal domains dispersed in a cubic matrix. These domains remain tetragonal at room temperature because the elastic energy required for the t → m transformation exceeds the thermodynamic driving force [31], [52], [57], [58]. This metastable configuration, often referred to as t′-ZrO_2, combines high thermal stability with moderate ferroelastic strain, enabling limited domain switching under stress without catastrophic cracking [43]. The phase equilibria of the ZrO_2–Y_2O_3 system (Figure 1.2) illustrate how increasing yttria content stabilizes the tetragonal and cubic phases, suppressing the monoclinic field below 1170 °C.

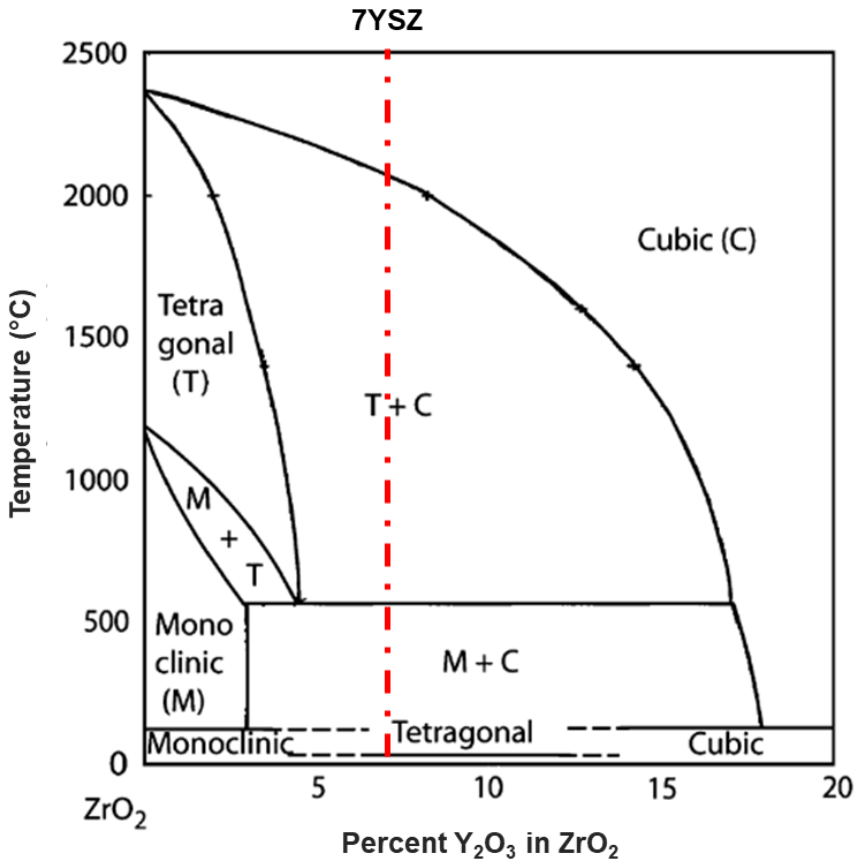


Figure 1.2 ZrO_2-Y_2O_3 phase diagram (wt.%). [55]

When the yttria content increases beyond ≈13–17 wt.%, the system becomes fully stabilized cubic zirconia (c-ZrO_2). The cubic fluorite lattice (Fm-3m)

provides high ionic conductivity and excellent thermal stability, but its lack of transformation capability reduces fracture toughness [36], [59]. For this reason, compositions containing 5–11 wt.% Y_2O_3 (3YSZ–6YSZ) are preferred for structural and thermal applications, where the coexistence of tetragonal domains contributes to transformation toughening [36].

YSZ's combination of low thermal conductivity, high melting point, and thermal expansion compatibility ($\alpha \approx 10 \times 10^{-6}\ K^{-1}$) with Ni-based superalloys makes it the reference top-coat material in current turbine technologies. Its microstructural stability during long-term exposure and resistance to sintering are directly linked to the distribution of oxygen vacancies and the fine-scale retention of the t′-phase. These attributes explain why YSZ remains the benchmark material for TBC systems, balancing phase stability, low k, and mechanical reliability under extreme thermal gradients [60], [61], [62].

In the following section, attention is focused on how the addition of a pentavalent oxide as co-dopant can modify the defect chemistry and lattice strain to further improve the thermal and chemical durability of the t′-phase under service conditions.

1.2.2. Role of pentavalent dopants (Ta^{5+}, Nb^{5+}, etc.)

When zirconia is co-doped with pentavalent elements such as tantalum (Ta^{5+}) or niobium (Nb^{5+}), its defect chemistry and structural stability undergo a noticeable alteration. These cations replace zirconium ions (Zr^{4+}) in the lattice, introducing a local excess of positive charge. In systems already stabilized with trivalent dopants such as yttrium, this additional charge partially compensates the oxygen vacancies created by Y^{3+} substitution. The result is a smoother distribution of lattice defects and a reduction in vacancy clustering, which together help the material maintain its non-transformable tetragonal (t′) structure even after long-term exposure to elevated temperatures [17], [18], [36], [63].

Pentavalent cations such as Ta^{5+}, Nb^{5+}, or V^{5+} can substitute zirconium ions (Zr^{4+}) in the zirconia lattice and act as donor dopants. Their incorporation modifies the charge balance established by trivalent stabilizers like yttrium, leading to a more complex and adjustable defect chemistry. The fundamental effect of these cations is the partial compensation of the oxygen

vacancies generated by trivalent dopants, which reduces local lattice distortion and improves phase stability [17]. In systems co-doped with Y^{3+} and pentavalent species, charge neutrality can be described using Kröger–Vink notation as follows:

$$xM_2O_5 + yY_2O_3 \rightarrow 2xM_{Zr}^{\cdot} + (5x + 3y)O_O^x + (y - x)V_O^{\cdot\cdot} \quad (1.2)$$

where $M_{Zr}^{\cdot}$ represents a pentavalent dopant (e.g., Ta^{5+}, Nb^{5+}) substituting a zirconium site, $O_O^{\times}$ a neutral oxygen ion in its lattice position, and $V_O^{\cdot\cdot}$ a doubly charged oxygen vacancy. This equation captures how donor–acceptor co-doping can adjust the effective vacancy concentration. When the dopant concentrations are nearly equimolar (y ≈ x), the donor and acceptor effects offset each other, and no net oxygen vacancies are generated. The resulting lattice is charge-neutral, elastically relaxed, and less prone to defect clustering or vacancy migration. This charge compensation leads to local neutrality within the lattice, minimizing electrostatic imbalance and elastic strain. As a result, vacancy clustering is suppressed, and the zirconia matrix maintains a more uniform and elastically stable configuration [36], [38], [56].

Structurally, the inclusion of pentavalent cations slightly increases the tetragonality (c/a) and overall lattice parameters, consistent with a stabilized non-transformable tetragonal (t′) phase [11], [64]. These dopants also tend to slow grain growth and suppress the t′ → t or t → m transformations during long-term exposure, preserving a fine-grained and thermally stable microstructure. The refinement of grain size enhances phonon scattering, contributing directly to lower thermal conductivity, a property of central importance in thermal barrier coatings [65], [66], [67].

Altogether, the introduction of pentavalent dopants offers a way to refine the defect landscape of stabilized zirconia, reducing strain, preserving the t′-phase, and maintaining low thermal conductivity under demanding service conditions. These effects make co-doped systems, such as ZrO_2–Y_2O_3–Ta_2O_5 or ZrO_2–Y_2O_3–Nb_2O_5 particularly attractive for advanced thermal barrier coatings, where long-term phase and microstructural stability are critical.

1.2.3. The ZrO_2–Y_2O_3–Ta_2O_5 (YTZ) system

The ternary ZrO_2–Y_2O_3–Ta_2O_5 (YTZ) system has become a focus of interest in the development of next-generation thermal barrier materials, combining the structural advantages of trivalent and pentavalent doping with the intrinsic low thermal conductivity of zirconia. Its design is motivated by the limitations of conventional YSZ, which tends to lose its metastable tetragonal phase through grain coarsening, phase decomposition, and chemical degradation under extended thermal exposure above 1200–1300 °C [5], [68]. The addition of Ta_2O_5 to the ZrO_2–Y_2O_3 binary system has proven to extend the stability range of the t′-phase, delay the onset of sintering, and improve resistance to corrosive environments, particularly those containing molten silicate deposits (CMAS) [18], [68], [69].

Experimental studies on the ZrO_2–Y_2O_3–Ta_2O_5 phase diagram have revealed that the coexistence of Y^{3+} and Ta^{5+} in the zirconia lattice produces a compositional window where the t′-phase is reached at 1500°C and is stable at room temperature without transforming to monoclinic on cooling [68], [69], [70], [71]. As shown in Figure 1.3, this stability field lies along compositions containing 14–18 mol% of combined oxides, with a nearly equimolar ratio between Y_2O_3 and Ta_2O_5. This range corresponds to the region where the cationic charge is effectively balanced, minimizing lattice distortions as substitutional defects. That compositional balance allows YTZ to extend the thermal stability limit of the tetragonal phase from about 1200 °C in YSZ to nearly 1500 °C, without evidence of phase decomposition or grain coarsening.

The addition of Ta slightly increases the lattice parameter a and the tetragonality (c/a ratio), suggesting a subtle relaxation of the oxygen sublattice [11], [38], [45]. These structural refinements lead to enhanced resistance to the tetragonal-to-monoclinic transformation, both under thermal cycling and mechanical stress. Moreover, Ta^{5+} incorporation promotes a higher degree of lattice symmetry, narrowing the distribution of bond angles within the Zr–O network and reducing the energy barrier for ferroelastic domain reorientation. These effects, while subtle at the atomic scale, result in substantial improvements in structural reliability during prolonged operation at high temperature [36], [45], [72].

One of the major advantages of Ta incorporation into YSZ is its impact on microstructural stability during sintering and thermal aging. Studies have shown that Ta additions significantly reduce the grain growth rate constant, preserving finer grain structures and limiting densification even after exposure to 1300–1400 °C [18], [71]. This effect arises from the refractory character of Ta_2O_5 and its low diffusivity, which restricts cation transport and impedes boundary migration. In contrast, pure YSZ tends to form coarse, columnar grains after similar exposure, resulting in loss of compliance and partial destabilization of the t′-phase [14].

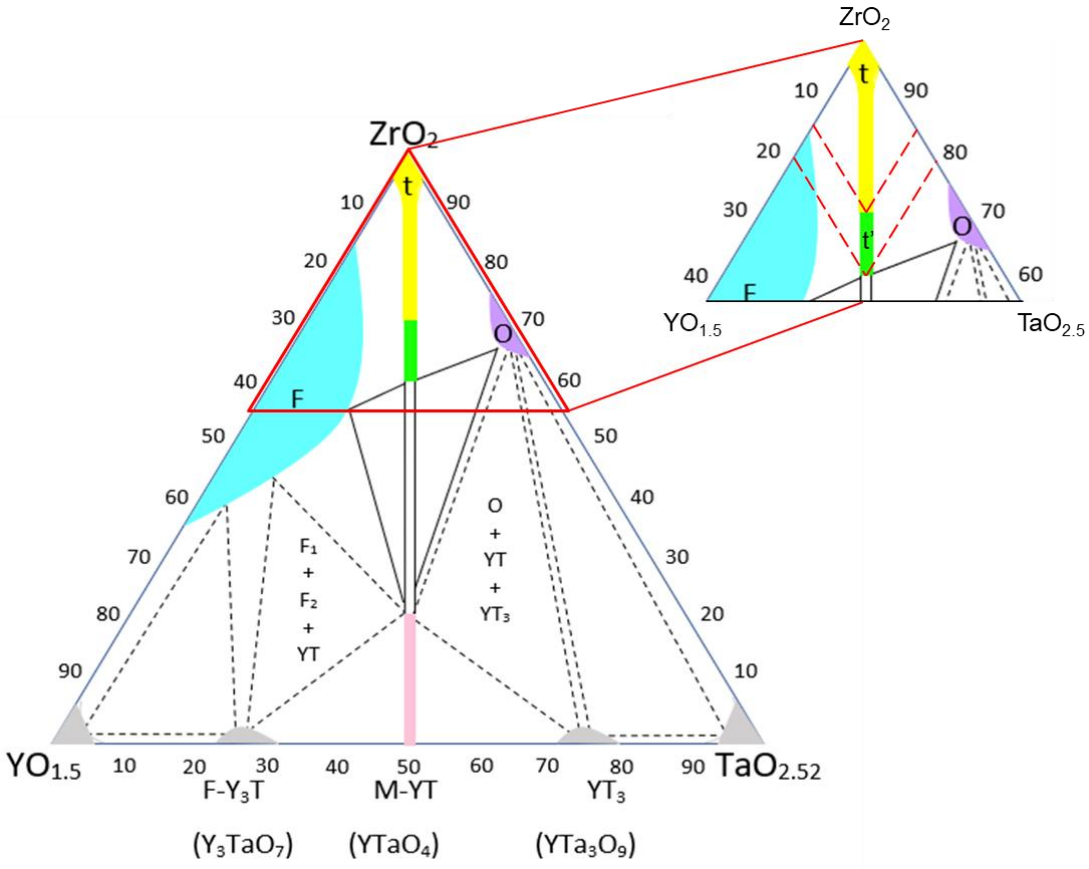


Figure 1.3 Phase diagram of ZrO_2–Y_2O_3–Ta_2O_5 showing the extended t′ field, where it can be observed that with equimolar amounts of $YO_{1.5}$ and $TaO_{2.5}$ in a range between 14-18 mol%, a *t′*-phase can be obtained (the area marked with red dotted lines).

Figure 1.4 compares the microstructures of YSZ and YTZ after identical annealing treatments (~ 1500 °C). The YTZ sample retains a dense but fine-grained structure, with well-defined grain boundaries and a limited number of intergranular pores. The morphological stability achieved through Ta incorporation is particularly beneficial for coatings, where coarsening of splats or lamellae leads to increased stiffness and higher thermal conductivity during service.

Microstructural refinement not only delays sintering but also enhances phonon scattering due to the combined influence of grain boundaries, mass fluctuation (from cation substitution), and lattice strain heterogeneity. Consequently, YTZ maintains its low thermal conductivity character even after extended exposure, unlike YSZ, which gradually densifies and loses its insulating capacity over time [18], [70].

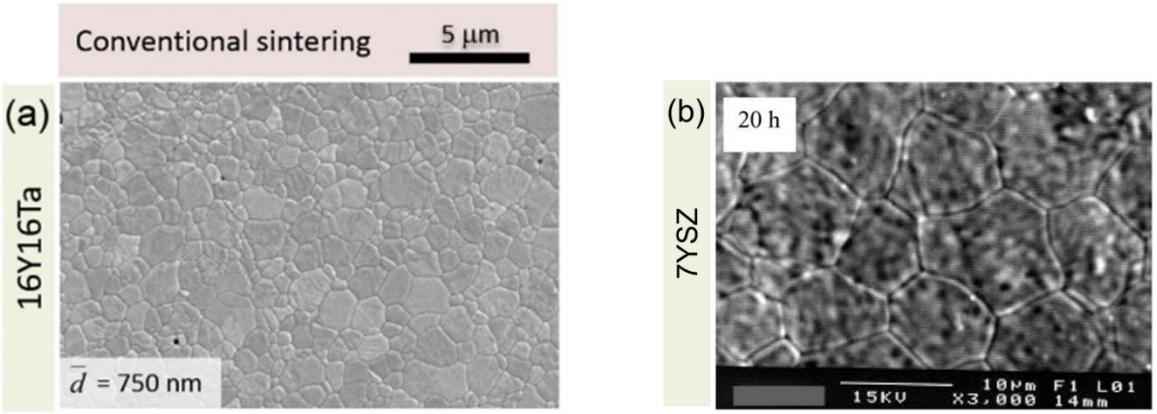


Figure 1.4 SEM micrographs comparing (a) YTZ [70] and (b) YSZ [73] microstructures after annealing at ~1500 °C.

The thermal conductivity (k) of YTZ is typically lower than that of YSZ, lying in the range of 1.6–1.9 $W \cdot m^{-1} \cdot K^{-1}$ at room temperature and decreasing slightly with temperature [17], [18], [70]. The reduction originates from both structural and chemical factors. At the atomic level, the coexistence of Y^{3+} and Ta^{5+} introduces mass contrast and strain fields that increase phonon scattering across the oxygen sublattice. At the mesoscale, the microstructural refinement produced by Ta doping enhances boundary scattering, which is known to dominate heat transport in ceramics with submicrometric grains. Consequently, YTZ maintains its low-thermal-conductivity character even after extended exposure, unlike YSZ, which gradually densifies and loses its insulating capacity over time [18], as illustrated in Figure 1.5.

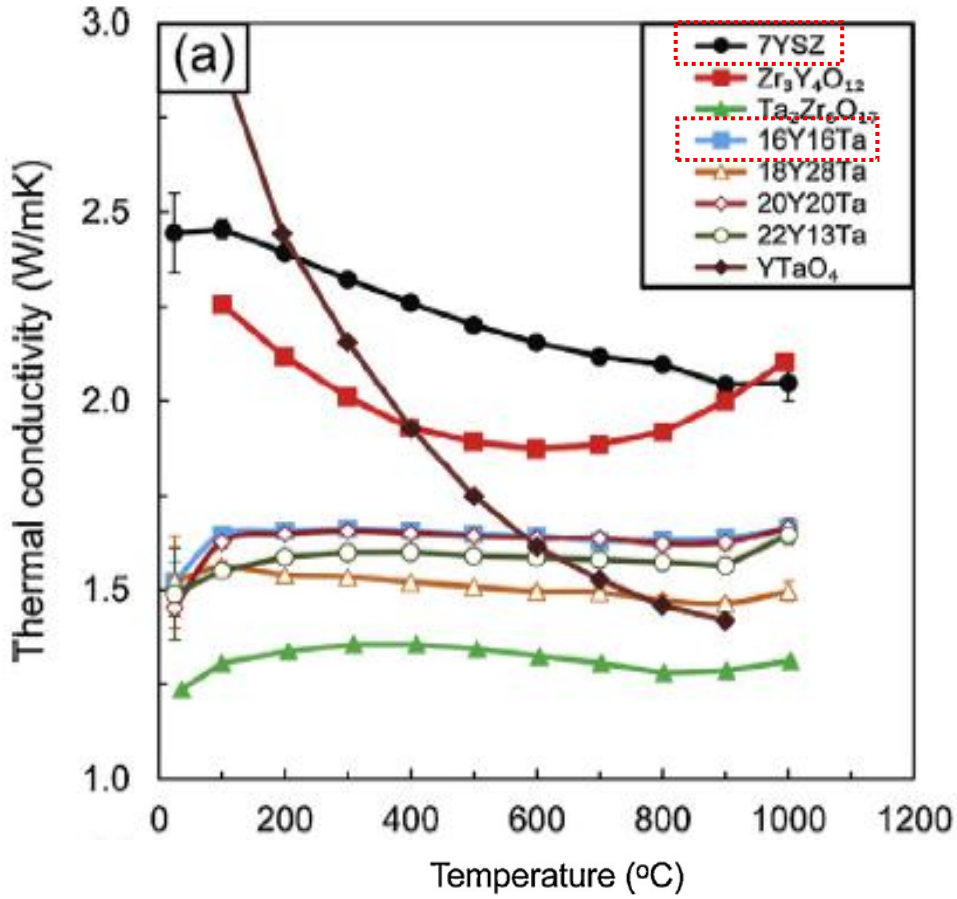


Figure 1.5 Thermal conductivity as a function of temperature for YSZ and YTZ compositions, showing the lower and more stable thermal conductivity of YTZ even after long-term annealing (samples indicated with dotted lines). [70]

Beyond the inherent reduction in (k), YTZ also shows superior thermal aging resistance, meaning that its k value changes very little after thermal cycling at 1300 °C. This behavior is attributed to its slower sintering kinetics and stable defect distribution. Such property retention is critical in TBCs, as performance degradation is often associated with microstructural densification and loss of porosity during operation [17], [18], [66].

The ZrO_2–Y_2O_3–Ta_2O_5 system exemplifies how targeted compositional design can overcome the intrinsic trade-offs of stabilized zirconias. Its unique combination of structural uniformity, low diffusivity, and chemical resilience enables it to operate stably in the severe thermal gradients and reactive atmospheres of modern turbines. For these reasons, YTZ has become one of the most studied candidates for next-generation thermal barrier coatings, designed to meet the thermal demands of high-efficiency propulsion and power systems.

1.3. Microstructural Control and Mechanical Behavior in Tetragonal Zirconia Systems

1.3.1. Microstructural stability and its influence

The microstructural configuration of zirconia-based ceramics, defined by the size, shape, grain-boundary density, and porosity distribution, plays a decisive role in determining their thermal, mechanical, and chemical behavior. Once the phase composition is fixed through stabilization, the evolution of microstructure becomes the dominant factor controlling the long-term stability of the tetragonal system.

In tetragonal zirconia materials such as YSZ and YTZ, the microstructure governs not only the mechanical strength and toughness but also the retention of the t′-phase during thermal exposure. Fine-grained microstructures limit the formation of transformation nuclei and suppress the tetragonal-to-monoclinic (t → m) transformation during cooling [44]. On the contrary, coarsening promotes local strain accumulation, grain-boundary cracking, and spontaneous phase transformation in unstabilized regions [43], [74]. The control of grain size through dopant chemistry and thermal processing is therefore essential, but so is the morphological stabilization of the grain boundaries that separate adjacent tetragonal domains.

The morphology of tetragonal grains influences the orientation-dependent elastic strain fields within the microstructure. In equiaxed-grain ceramics, stress accommodation is isotropic, favoring elastic domain switching and limiting residual stress after thermal cycling [75]. By contrast, anisotropic or elongated grains, as observed in partially sintered YSZ, generate local stress gradients that can trigger ferroelastic domain reorientation or even partial transformation under cyclic load [76].

These effects are illustrated schematically in Figure 1.6, which compares the distribution of internal stresses in fine, equiaxed-grain microstructures and in elongated-grain morphologies. In the homogeneous case (Figure 1.6(a)), stresses are evenly distributed across adjacent grains, promoting elastic domain switching and stability of the tetragonal structure. In contrast, elongated grains (Figure 1.6(b)) create localized stress concentrations at triple junctions and grain edges, where the mismatch in orientation can induce

ferroelastic domain reorientation or even partial t → m transformation under cyclic loading.

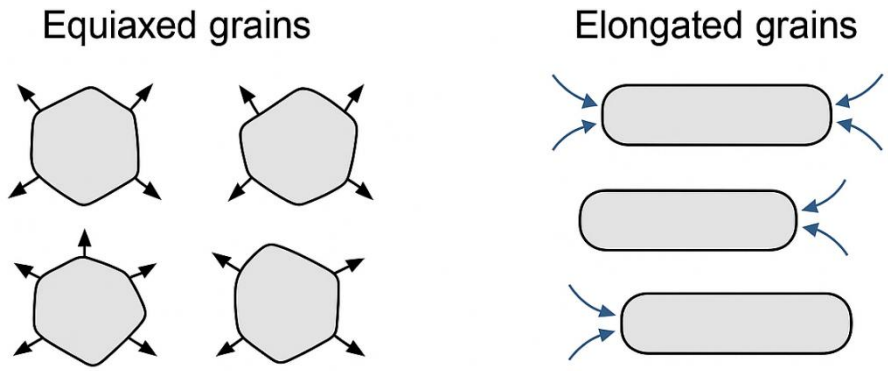


Figure 1.6 Schematic representation of stress distribution as a function of grain morphology in tetragonal zirconia. (a) Fine, equiaxed grains show homogeneous stress fields that promote ferroelastic domain stability. (b) Elongated grains generate localized stress concentrations that facilitate domain switching or t → m transformation.

Porosity is another key microstructural parameter influencing the performance of YTZ ceramics, especially in coatings. Controlled open and closed pores act as phonon-scattering centers, significantly reducing the effective thermal conductivity (k) while maintaining mechanical compliance. In YTZ coatings, the stability of this hierarchical pore network, comprising nanometric intergranular pores and micrometric lamellar gaps, persists up to 1400–1500 °C [15], [77]. This resistance to pore coalescence and densification delays sintering and preserves low k values over time.

1.3.2. Mechanoactivation of powders

Mechanochemical activation (or mechanoactivation) has become one of the most effective approaches for tailoring the reactivity, defect structure, and microstructural evolution of ceramic powders prior to consolidation or deposition. In zirconia-based systems, it is particularly relevant because the mechanical energy transferred during milling modifies the crystallite size, strain state, and defect density, thereby influencing both the sintering kinetics and the subsequent phase stability [78], [79].

The repeated impact and friction events occurring during milling generate localized high-pressure and high-temperature zones that promote solid-state reactions, partial amorphization, and lattice disordering [80]. As a result, the powders accumulate significant stored energy in the form of dislocations, oxygen

vacancies, and microstrain, which act as nucleation sites during subsequent thermal treatments. In systems such as YTZ, this accumulated energy plays a decisive role in enabling phase transformation in situ during plasma spraying or sintering.

1.3.2.1. Planetary ball milling

Planetary ball milling is a widely used technique for homogenizing ceramic mixtures and inducing mild mechanical activation. It operates through the combined rotation of a central disk and the individual vials containing the powder and grinding media, producing both centrifugal and shear forces [80], [81]. The repeated motion of the vials generates a continuous sequence of particle impacts, fragmentation, and cold-welding events that gradually refine and homogenize the powder mixture.

Figure 1.7 illustrates the operating principle of a planetary ball mill and the sequence of microstructural changes experienced by the particles during milling. The diagram shows the coordinated rotation of the vials and the supporting disc, the resulting centrifugal forces acting on the milling media, and the successive stages of the process: fracturing, welding, and dynamic equilibrium, that lead to the formation of fine, homogeneous powders suitable for subsequent sintering or deposition.

This configuration enables an efficient mixing of oxide powders, such as ZrO_2, Y_2O_3, and Ta_2O_5, while keeping the temperature relatively low. The main outcome is a progressive reduction of particle size, typically down to the submicrometric or nanometric range (400–800 nm), accompanied by limited lattice strain and defect introduction [29].

Overall, this technique provides a controlled degree of mechanical activation, refining the particle size and composition without destabilizing the structure. For YTZ feedstocks, planetary milling represents an intermediate stage between raw powder mixing and high-energy processing, producing powders that are homogeneous and reactive enough for subsequent dense ceramics fabrication.

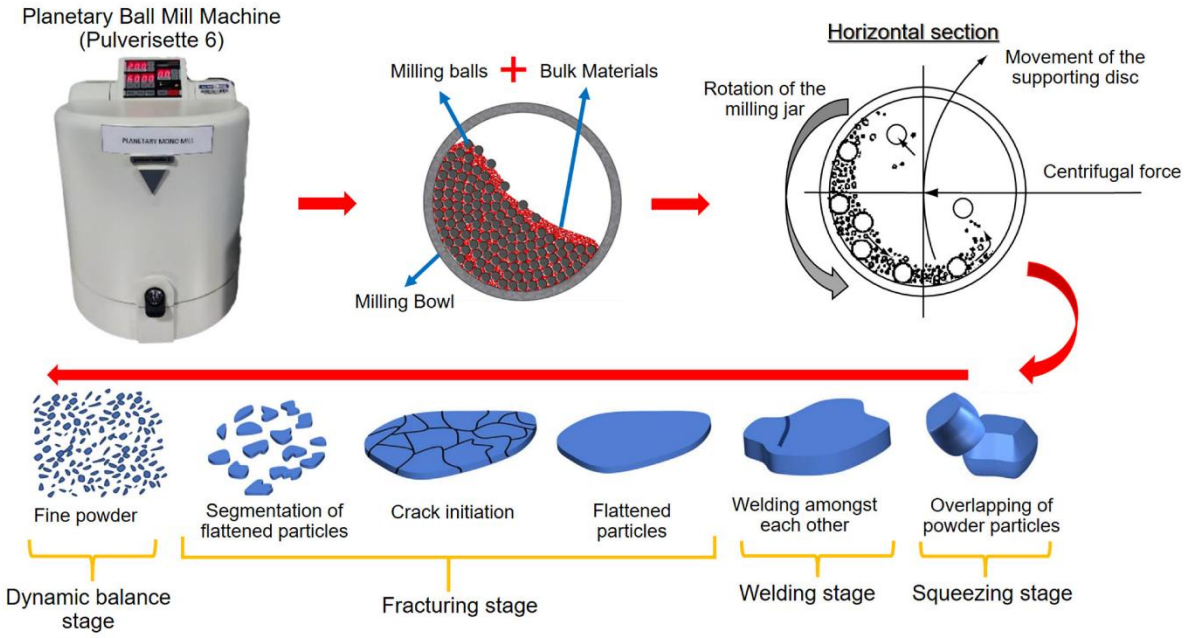


Figure 1.7 Schematic representation of the planetary ball milling process, showing the generation of centrifugal forces, powder movement, and successive stages of fracturing and welding leading to homogeneous submicrometric powders. [82]

1.3.2.2. High energy ball milling

High-energy ball milling is a mechanochemical technique designed to achieve extremely efficient particle refinement and structural activation through repeated, high-frequency impacts and frictional interactions between the powder and grinding media. Among the various configurations available, the Emax mill stands out for combining the operating principles of several mill types into a single mechanism that delivers both high impact energy and intensive friction [83].

In the Emax system, the grinding jars are mounted on two synchronized discs that rotate in the same direction, producing a controlled circular motion without jar reorientation. This movement, together with the oval geometry of the jars, generates a unique combination of impact and shear forces, allowing efficient particle deformation and mixing at high speeds [79]. As shown in Figure 1.8, the superposition of circular motion and jar geometry creates strong compressive and tangential stresses between the grinding balls, powder, and jar walls, leading to extremely fine particle sizes and homogeneous mixing.

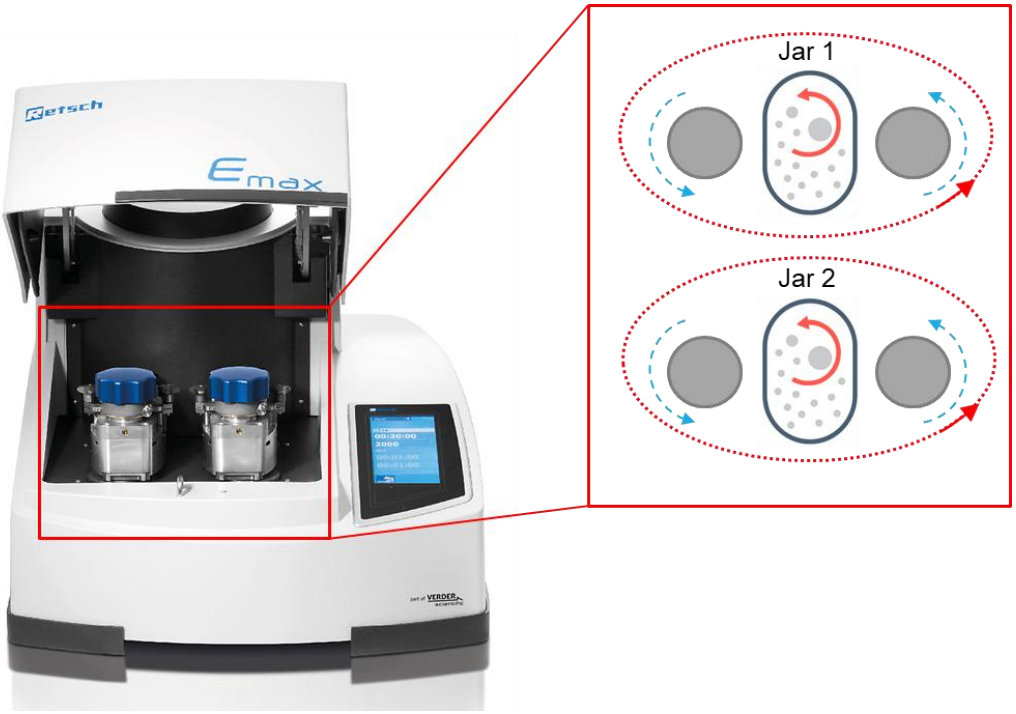


Figure 1.8 Schematic representation of the motion pattern in the Emax high-energy ball mill. The jars follow a circular trajectory controlled by two synchronized discs, generating simultaneous impact and shear forces through their oval geometry. This configuration results in high-frequency collisions, efficient frictional mixing, and uniform mechanical activation of zirconia-based powders (adapted from Retsch [83])

During milling, the powder experiences continuous high-energy collisions and frictional sliding, which promote grain refinement down to the nanometric scale. This mechanical activation reduces the thermal energy required for diffusion and facilitates solid-state reactions or phase transformations during subsequent heat treatments or plasma spraying [78], [79].

A key advantage of the Emax configuration is its efficient liquid-cooling system, which dissipates frictional heat generated at rotational speeds up to 2000 rpm. Unlike conventional planetary mills that require intermittent cooling periods to prevent overheating, the Emax enables continuous high-energy milling while maintaining temperature stability, ensuring consistent activation across the entire powder batch. For zirconia-based ceramics, particularly the ZrO_2–Y_2O_3–Ta_2O_5 (YTZ) system, this capability makes it especially suitable for producing metastable, nanostructured feedstocks capable of undergoing in-situ tetragonal phase formation during coating deposition [3], [77].

The main operational and microstructural differences between planetary and high-energy ball milling are summarized in Table 1.2. This comparison highlights the progressive increase in mechanical energy, defect density, and powder reactivity achieved with high-energy milling, which ultimately makes it the preferred technique for the preparation of YTZ feedstocks intended for plasma-sprayed coatings.

Table 1.2 Comparison between Planetary Ball Milling and High-Energy Ball Milling. (Data summarized from Retsch, The Art of Milling [83])

Factor	Planetary Ball Milling	High-energy Ball Milling
Movement and mechanism	Jars mounted eccentrically on a rotating “sun wheel.” The jars rotate in the opposite direction, generating impact and friction between balls and walls.	Two counter-rotating discs drive oval-shaped jars in a continuous circular path without orientation change, combining high-frequency impact, intensive friction, and controlled motion.
Typical speed and energy input	Up to 800 rpm; energy determined by rotational speed and mass of balls.	Fixed at 2000 rpm, producing much higher acceleration and energy density.
Grinding mode and achievable particle size	Dry or wet grinding; final fineness ≤ 10 µm (dry) or sub-µm (wet).	Primarily wet grinding; nanoscale (< 100 nm) achievable due to simultaneous high impact + friction.
Thermal control	Heat generation during long runs requires intermittent cooling breaks (~ 60%) to prevent overheating.	Integrated liquid cooling system enables continuous operation without breaks, dissipating frictional heat efficiently.
Sample capacity and jar volume	Up to 4 jars (12–500 ml each); flexible setup for alloying or homogenization.	Two jars (50 or 125 ml each) designed for high-energy continuous milling.

1.3.3. Ferroelasticity and toughening mechanisms

The exceptional mechanical performance of tetragonal zirconia arises from two key mechanisms that operate at the grain scale: ferroelastic domain switching and stress-induced phase transformation. Both mechanisms contribute to the material's ability to accommodate strain and resist crack propagation, though they differ fundamentally in reversibility and structural change. Understanding the balance between these mechanisms is essential to explain the toughness and high-temperature stability of the YTZ system.

In the tetragonal phase, mechanical loading produces local strain accommodation through the reorientation of crystallographic variants. The process involves rotation of the *c-axis* within neighboring grains, aligning ferroelastic domains with the applied stress direction [59], [84]. Figure 1.9 schematically illustrates this behavior: under an external load, the region near a stress concentrator, such as a crack tip, exhibits domain reorientation and partial transformation. These microstructural adjustments reduce the local tensile stress and help dissipate energy without inducing catastrophic fracture.

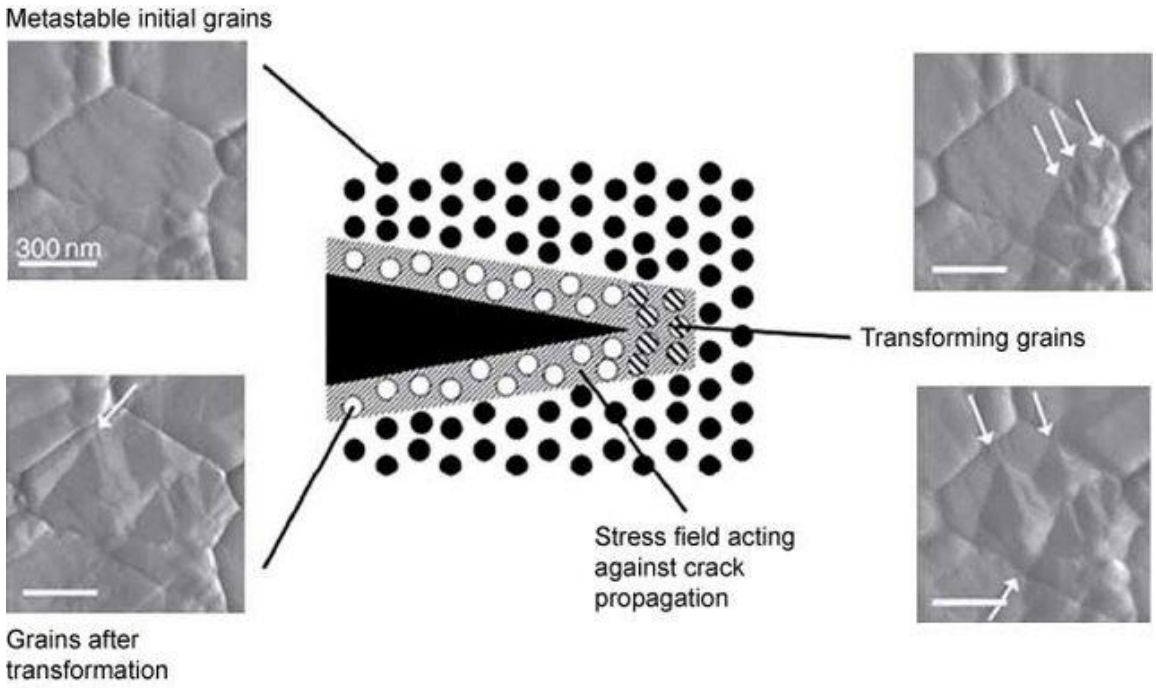


Figure 1.9 Illustration of ferroelastic domain reorientation and local strain accommodation near a crack tip in tetragonal zirconia. Domain switching and limited transformation contribute to stress relaxation and crack-tip shielding (adapted from Heuer et al. [75]).

A more detailed understanding of the ferroelastic contribution to the toughness of tetragonal-prime zirconia (t′-YSZ) was proposed by Mercer, Williams, Clarke, and Evans (2007) [59]. Their model established that the energy dissipation associated with ferroelastic switching occurs within a localized region in the wake of a crack, referred to as the ferroelastic process zone. In this zone, intense shear stresses promote the nucleation and propagation of ferroelastic domains, allowing strain accommodation without transformation into the monoclinic phase.

As shown schematically in Figure 1.10(a), when the shear stress around a crack tip reaches the critical shear stress, ferroelastic domains nucleate and switch orientation, generating a permanent shear strain γ^T. The cumulative switching of these domains produces a distributed process zone of height h and volume fraction f of transformed material. This mechanism introduces local hysteresis and dissipates part of the applied strain energy, effectively shielding the crack tip. The associated energy release rate reduction was formulated as:

$$\Delta\Gamma = 2fh\tau^T\gamma^T \tag{1.3}$$

where ΔΓ represents the energy absorbed by ferroelastic switching (toughness), and $\tau^T\gamma^T$ corresponds to the energy dissipated per unit volume of the process zone.

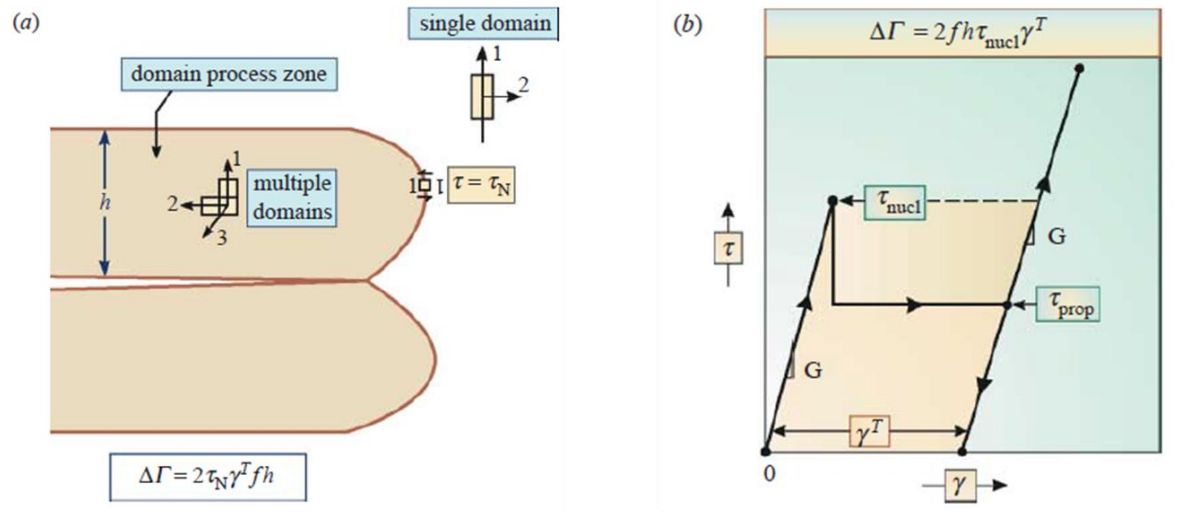


Figure 1.10 (a) Schematic of a ferroelastic process zone near a crack tip. (b) Corresponding stress–strain curve showing the hysteretic response of t′-YSZ during domain nucleation and switching. The mechanism activates when shear stress ($\boldsymbol{\tau}$) exceeds the critical stress ($\boldsymbol{\tau^T}$), generating a permanent shear strain ($\boldsymbol{\gamma^T}$). [59]

The corresponding stress–strain response, shown in Figure 1.10(b), exhibits a pronounced hysteresis loop. Initially, the material responds elastically until the local stress reaches τ^T; beyond this threshold, domain nucleation and propagation occur, resulting in a permanent strain offset. The area enclosed by the loop represents the energy dissipated during domain switching, while the partial recovery upon unloading reflects the reversible component of the ferroelastic response. This behavior explains the pseudo-plastic deformation and enhanced fracture resistance observed in fine-grained t′-YSZ, where the ferroelastic process predominates over transformation toughening.

The improvement in fracture toughness of stabilized tetragonal zirconia is primarily attributed to ferroelastic toughening, rather than to the classical tetragonal-to-monoclinic transformation mechanism.

In the t′-phase, where the tetragonal lattice is fully retained, mechanical stresses promote the switching of ferroelastic domains toward energetically favorable orientations. This domain reorientation enables local strain accommodation around the crack tip, where part of the applied mechanical energy is absorbed and subsequently dissipated as heat. The hysteretic stress–strain response associated with this process reflects the amount of energy consumed during switching, and the area enclosed by the hysteresis loop represents the material's effective toughness.

The efficiency of ferroelastic toughening is closely related to the tetragonality (c/a ratio) of the crystal structure: larger tetragonality enhances the resistance to domain switching and increases the energy required for reorientation, leading to higher fracture toughness. Unlike transformation toughening, which is ineffective at elevated temperatures due to the loss of driving force for the t → m transformation, ferroelastic toughening remains operative even above the T_0(t/m) boundary [45], providing an intrinsic mechanism for toughness and damage tolerance in thermal barrier coatings based on t′-zirconia.

1.4. Zirconia-based ceramics for thermal barrier coatings (TBCs)

1.4.1. Thermal barrier coatings and their requirements

Thermal barrier coatings (TBCs) are multilayer systems designed to protect metallic components operating in aggressive high-temperature environments, such as gas turbines and aero-engines. A conventional TBC typically consists of three principal layers on a superalloy substrate: a bond coat, a thermally grown oxide (TGO), and a ceramic topcoat that provides the primary thermal insulation [2], [5], [8]. Each layer fulfills a distinct role within the system, and their collective performance determines the overall durability of the coating under cyclic thermal and mechanical loading.

Figure 1.11 illustrates the general architecture of a thermal barrier system. The metallic substrate, commonly Ni-based superalloys such as René 80 or CMSX-4, provides structural integrity and creep resistance. A metallic bond coat, typically MCrAlY (where M = Ni, Co, or a combination), acts as a diffusion barrier and oxidation-resistant layer. During operation, selective oxidation of Al in the bond coat forms a continuous alumina scale known as the thermally grown oxide (TGO). Finally, the ceramic topcoat, generally based on partially stabilized zirconia, offers thermal insulation due to its low thermal conductivity and high melting point [48].

The performance of a TBC is governed by the synergistic behavior of these layers during service. At temperatures exceeding 1000 °C, thermal gradients across the coating induce stress due to differences in the coefficients of thermal expansion (CTE) between the metallic and ceramic layers. Cyclic oxidation further leads to the thickening of the TGO and the accumulation of stresses at the interfaces, which may eventually cause crack initiation and spallation of the topcoat. To ensure long-term durability, a successful TBC system must therefore combine low thermal conductivity, high fracture toughness, phase stability, and chemical inertness of the ceramic layer with excellent oxidation resistance and adherence of the bond coat [62], [85].

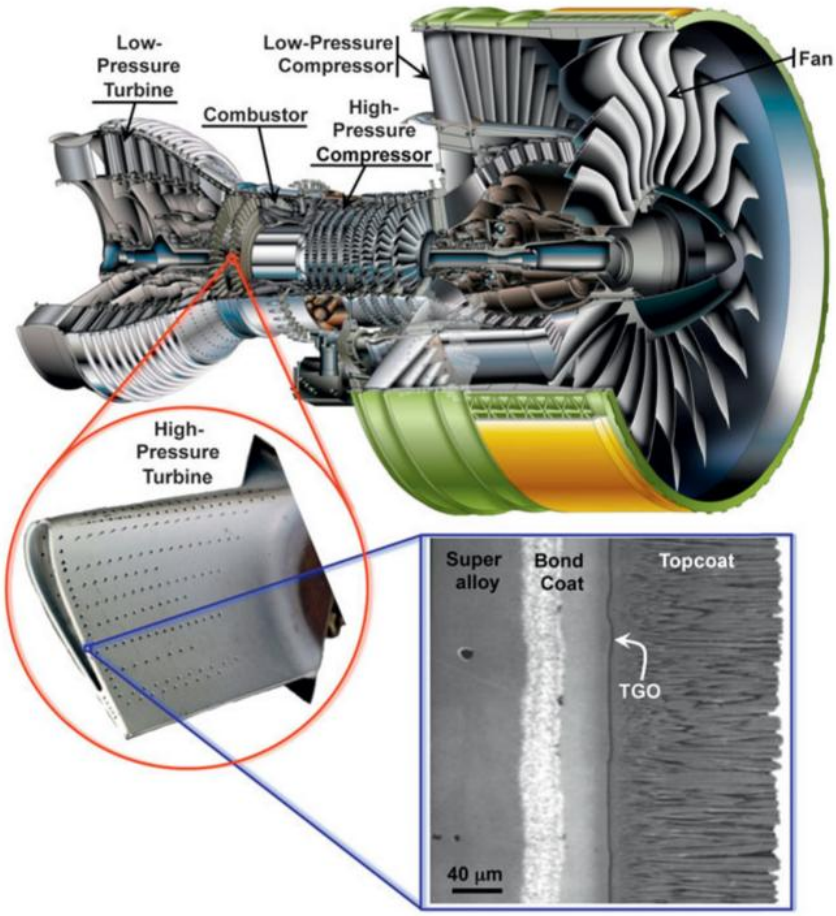


Figure 1.11 Schematic representation of a typical thermal barrier coating system showing the superalloy, bond coat, thermally grown oxide (TGO), and ceramic topcoat. [2]

Figure 1.12 summarizes the main requirements for the ceramic topcoat in a TBC system. Thermophysical properties such as low conductivity (≤ 2 W m^{-1} K^{-1}), high melting temperature (> 2600 °C), and a low CTE mismatch with the substrate are essential to minimize thermal stress during heating and cooling cycles. Additionally, the coating must remain chemically stable and resistant to sintering or phase decomposition under prolonged exposure to hot gases [86], [87].

The development of new compositions such as co-doped YTZ arises from the need to extend these capabilities to higher temperatures (> 1300 °C) and to environments with more severe thermal gradients.

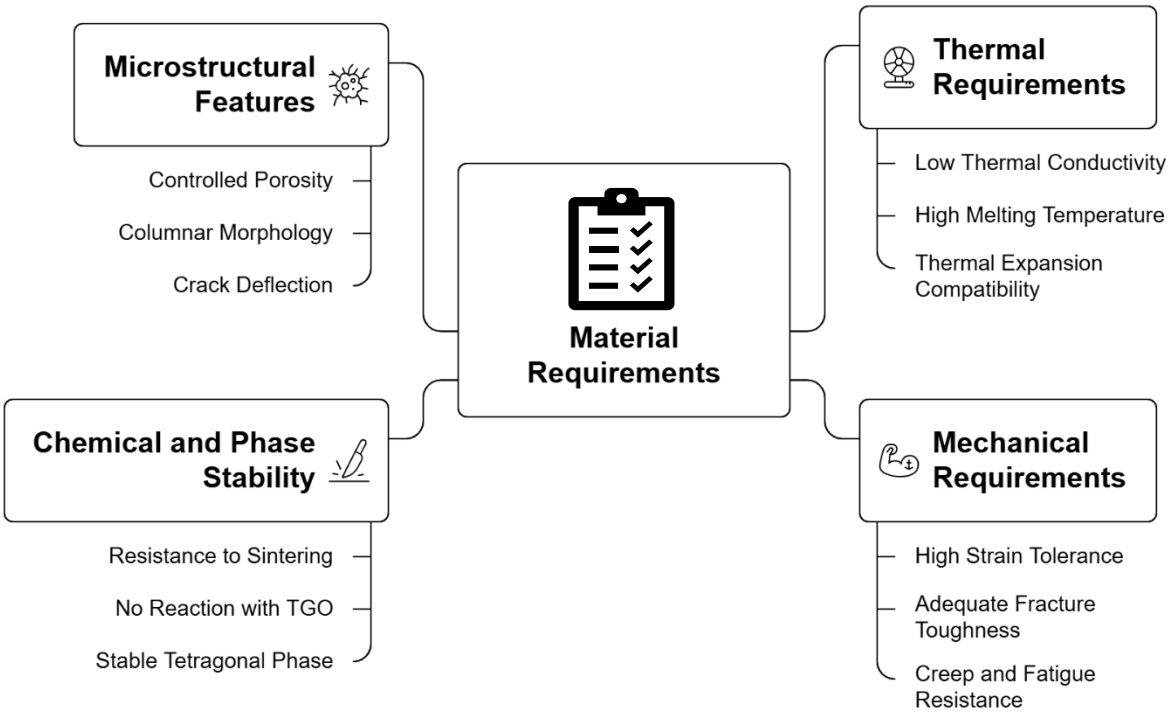


Figure 1.12 Main design and performance requirements for ceramic topcoats in TBCs.

Such systems aim to maintain the balance between low conductivity, mechanical compliance, and microstructural stability, while reducing the susceptibility to sintering and phase destabilization observed in conventional 7YSZ coatings.

1.4.2. Thermal Spray Techniques

The spraying method plays a decisive role in determining the microstructure, adherence, and functional performance of thermal barrier coatings. Among the various techniques available for ceramic coating fabrication, thermal spray processes have become the most widely adopted due to their scalability, versatility, and ability to produce coatings with tailored porosity and thickness.

There are several spray techniques used for thermal barrier coatings, but before identifying them, it is important to first define the concept of thermal spray deposition. As illustrated in Figure 1.13, the central element of any thermal spray system is a spray torch, which converts incoming energy, either chemical (in combustion-based systems), electrical (in plasma-based systems) or kinetic (in cold spray), into a high-temperature, high-velocity gas stream capable of melting and

and/or propelling the coating material toward the substrate. The feedstock, which may be supplied as a powder, wire, or rod, is introduced into the plasma jet or combustion flame, where it is heated and accelerated. Molten or semi-molten particles impact the substrate, flatten, and solidify to form the coating through a splat-by-splat buildup process [6], [19], [88].

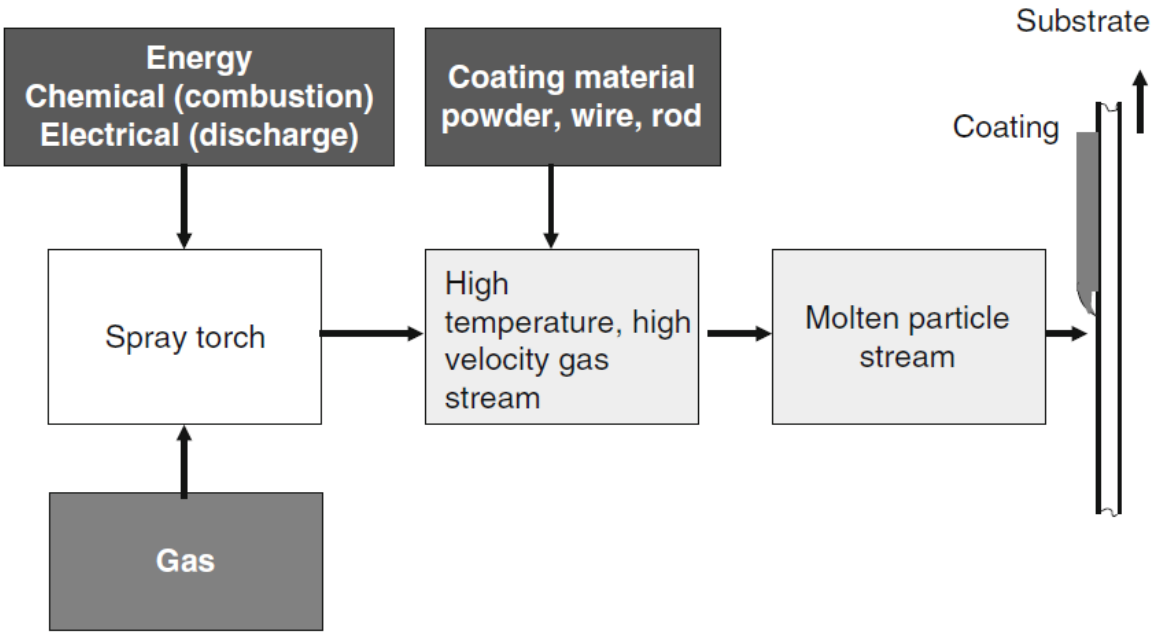


Figure 1.13 Representation of a general thermal spray process. The spray torch converts chemical or electrical energy into a high-temperature gas stream that melts and propels the coating material toward the substrate. [19]

Several deposition techniques fall under the category of thermal spray, differing in their heat source, gas dynamics, and feedstock form. The main processes include [4]:

- Flame spray
- High Velocity Oxy-Fuel (HVOF)
- High Velocity Air-Fuel (HVAF)
- Cold Spray
- Atmospheric Plasma Spray (APS)
- Suspension Plasma Spray (SPS)

Another technique to elaborate thermal barriers is the Electron Beam Physical Vapor Deposition (EB-PVD).

Among these, APS, SPS, and EB-PVD are the most attractive for the fabrication of the topcoat layer, as they can produce coatings with tailored porosity, phase composition, and microstructure suitable for high-temperature environments [89]. Although all three are used to deposit zirconia-based ceramics, their resulting microstructures differ substantially, leading to distinct mechanical and thermal behaviors as is shown in Figure 1.14.

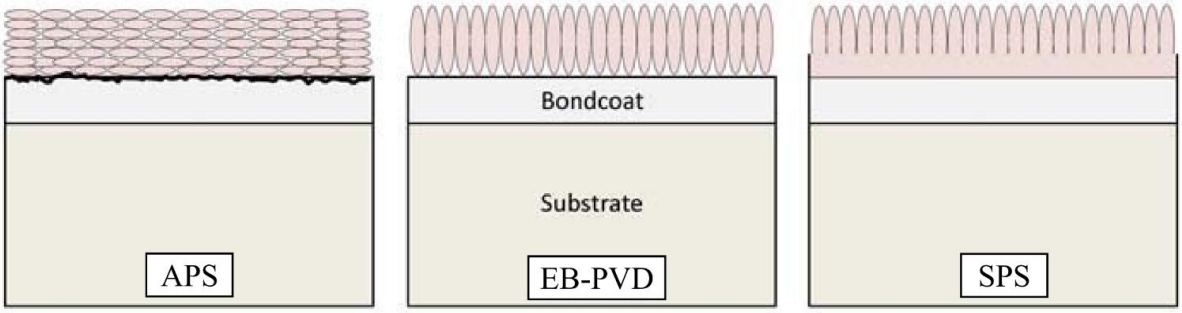


Figure 1.14 Schematic comparison of topcoat typical microstructures produced by APS, SPS, and EB-PVD processes. APS yields a lamellar splat structure, SPS produces a feather-like or columnar morphology depending on parameters, and EB-PVD forms highly oriented columnar grains. [89]

APS coatings exhibit a lamellar splat-based architecture with interlamellar pores and microcracks that enhance strain tolerance. EB-PVD coatings develop a columnar structure, which provides excellent strain accommodation and erosion resistance but at significantly higher processing cost. SPS coatings, in contrast, present a bimodal or feather-like morphology derived from the fine droplets in the liquid feedstock, offering a tunable balance between density and compliance. Together, these techniques represent the current state-of-the-art in the deposition of advanced ceramic coatings for gas-turbine applications [4], [19].

The variation of the plasma spray process that has gained attention in recent years is Suspension Plasma Spraying (SPS), which enables the use of submicrometric and nanometric feedstocks dispersed in liquid suspensions. SPS produces microstructures that bridge the gap between the lamellar morphology of APS and the columnar structures of EB-PVD, offering enhanced control over porosity, texture, and roughness [90], [91].

1.4.2.1. Suspension Plasma Spraying (SPS)

Suspension Plasma Spraying (SPS) is an advanced variant of the conventional atmospheric plasma spray (APS) process, developed to enable the deposition of coatings from submicrometric and nanometric feedstocks that cannot be efficiently processed using traditional powder injection. Instead of feeding dry powders, the precursor material is dispersed in a liquid carrier medium, typically water or ethanol, forming a stable suspension that is injected directly into the plasma jet [24], [92], [93]. This modification expands the range of achievable microstructures and allows precise control of coating porosity, texture, and columnar morphology.

The Figure 1.15 schematically illustrates the principle of the SPS process. The suspension is atomized upon injection into the high-temperature plasma, where the liquid phase evaporates and the solid particles are accelerated and partially melted. Their trajectories and in-flight thermal histories depend strongly on the plasma enthalpy, injection angle, carrier flow rate, and droplet breakup dynamics [24]. As the particles impact and solidify on the substrate, a microstructure forms that can vary from finely lamellar to columnar and feather-like, depending on the substrate temperature and the plasma–particle interaction regime.

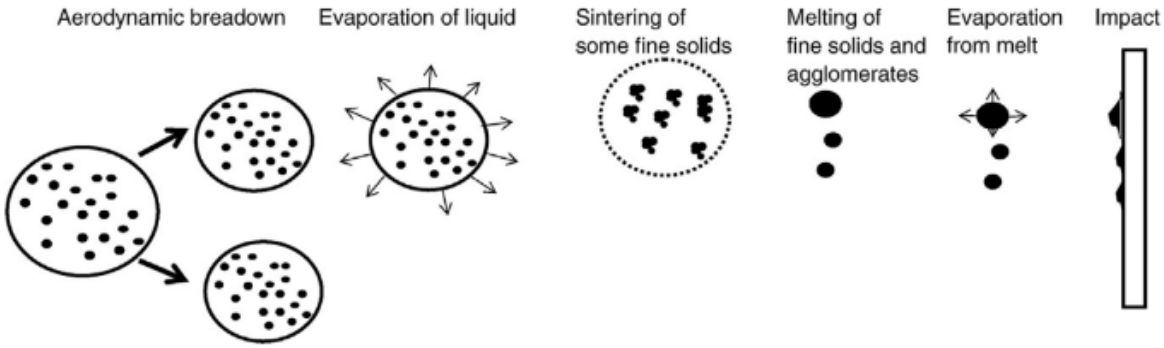


Figure 1.15 Schematic of the Suspension Plasma Spraying (SPS) process showing the injection of a liquid suspension into a plasma jet. Molten particles impact the substrate and form the coating. [94]

Compared to conventional APS, the SPS process provides a higher degree of microstructural control and produces coatings with unique porosity architectures that combine fine intra-splat pores with inter-columnar gaps [86], [95].

The microstructure obtained by the SPS process, as shown in Figure 1.16, exhibits a characteristic columnar and feather-like morphology composed of elongated clusters of fine particles that grow perpendicular to the substrate. This architecture promotes high strain compliance by allowing the columns to flex and expand independently during thermal cycling [96]. The topographical BSE view reveals a surface composed of clusters with cauliflower-like terminals and partially merged microfractal structures, reflecting the dynamic solidification of particles within the plasma jet [97].

This distinctive surface morphology, together with the internal columnar arrangement and interconnected porosity, defines the hierarchical architecture typical of SPS coatings, providing a balance between mechanical integrity, strain tolerance, and low thermal conductivity.

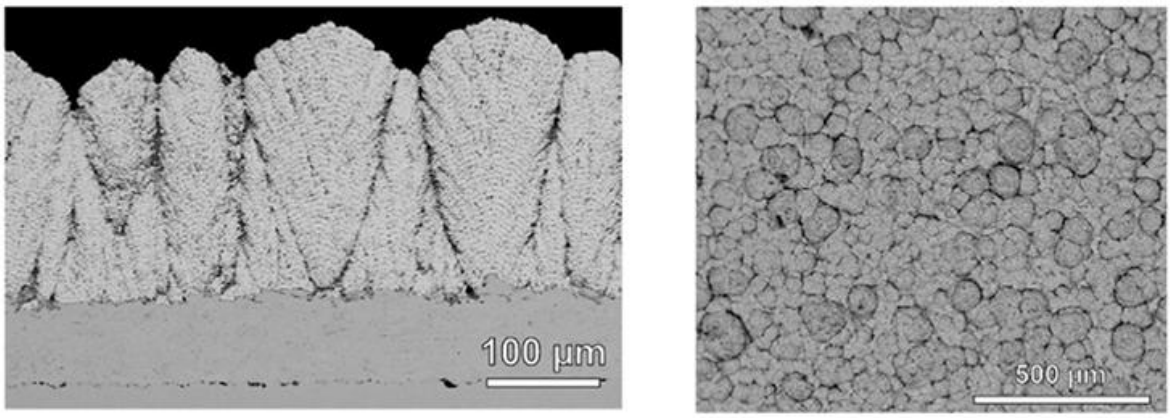


Figure 1.16 Cross-section and top-view BSE micrographs of a typical SPS coating showing columnar growth (left) and the topographical surface morphology characterized by cauliflower-like clusters and merged microfractal structures (right). [97]

These features significantly improve the strain compliance and thermal insulation of the coating. The columnar-like structures formed by SPS resemble those of EB-PVD coatings, yet they are obtained through a more flexible and cost-effective route. In addition, the high surface area and fine-scale porosity of SPS coatings contribute to low thermal conductivity while maintaining excellent adherence and mechanical integrity [98].

The versatility of the SPS technique lies in the tunability of its process parameters. Key variables include the solid content and viscosity of the suspension, the carrier gas flow rate, the plasma power, and the stand-off distance. Optimization

of these parameters allows tailoring of the coating microstructure for specific applications, such as dense barrier layers, porous thermal insulators, or graded architectures.

Recent studies have also shown that SPS coatings exhibit improved sintering resistance and better phase retention compared to conventional APS coatings, making the technique particularly suitable for next-generation TBCs operating above 1300 °C [86], [99].

CHAPTER 2: Experimental procedure

The purpose of this chapter is to describe the experimental procedures used to carry out zirconia-yttria-tantala (YTZ) dense ceramics and coatings. It starts with the obtention and characterization of commercial zirconium oxide (ZrO_2), yttrium oxide (Y_2O_3), and tantalum oxide (Ta_2O_5) using X-ray diffraction (XRD), scanning electron microscopy (SEM), and particle size analysis to guarantee the conditions given by the supplier and ensure their suitability for processing. Five different compositions within the non-transformable tetragonal phase of the ZrO_2–Y_2O_3–Ta_2O_5 ternary system were prepared using planetary ball milling, with one composition prepared by high-energy ball milling for comparison.

The methodology includes the powder compaction by uniaxial press at 250 MPa and sintering of green samples at 1500 °C for 2 and 20 h to stabilize the non-transformable tetragonal phase. The obtained dense ceramics were characterized by XRD, SEM/EBSD, Raman spectroscopy, microhardness testing, elastic modulus, fracture toughness, thermal conductivity, and ferroelasticity.

The final section describes the preparation of raw material (16YTZ) using high-energy ball milling for the suspension plasma spraying (SPS) process, with vial filling varying from 30% to 40% in volume. The respective coatings were characterized by XRD and SEM. Overall, this chapter describes in detail the methodology applied throughout the project, from raw material preparation to the analysis of the final coatings and ceramics (See the figure 2.1).

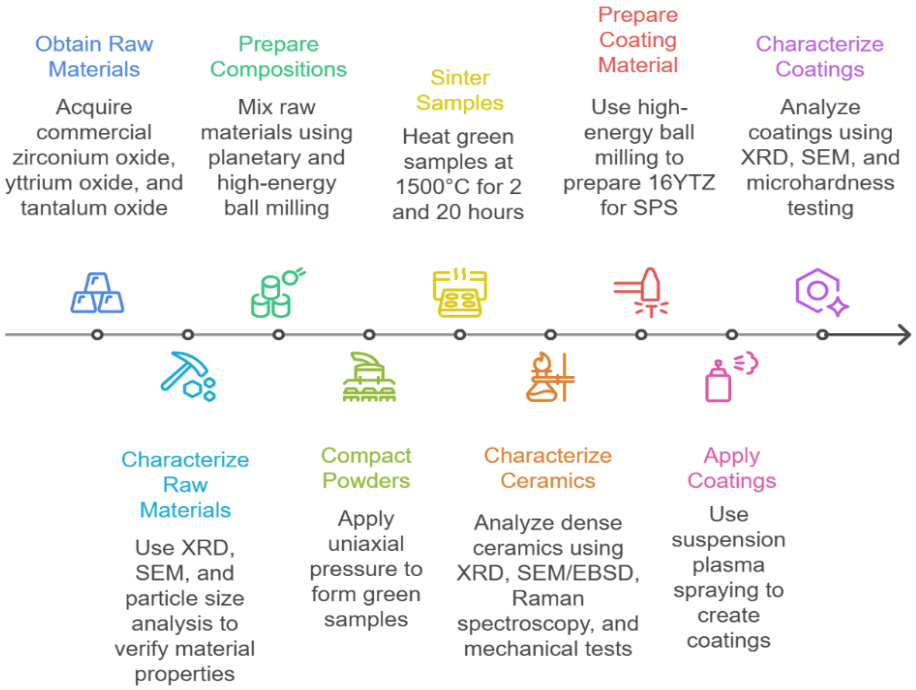


Figure 2.1. Overview of the development of the project.

2.1. Synthesis and characterization of ZrO_2-Y_2O_3-Ta_2O_5 dense ceramics

2.1.1. Powder milling, pressing and sintering of dense ceramics

Powders mixtures and mechanoactivation of ZrO_2 - $xYO_{1.5}$ - $xTaO_{2.5}$ (where x = 15.4, 16, 16.6, 17.2 and 17.8 mol%) were carried out by planetary ball milling of mixed oxides using ZrO_2 (99.9 %, Alfa Aesar, USA), Y_2O_3 (99.99 %, Alfa Aesar, USA) and Ta_2O_5 (99.99 %, Suoyi, China) as precursors. These precursors were preheated at 1000°C for 2 h, then a stoichiometric amount of each one was weighed and mixed in a liquid medium (with 1.5 g of ethanol) by a planetary ball-milling (Pulverisette 6, Fritsch) for 12 h at 240 RPM with reverse mode every hour in a jar of 45 mL [3]. The balls:powder ratio (BPR) was 10:0.77 in mass and the diameter of the zirconia balls used as milling media was 10 mm. Subsequently, the milled and dried powders were compacted into coupons of approximately 10 mm in diameter and 1 mm of thickness by uniaxial press at 250 MPa. The green samples were sintered in a chamber furnace at 1500°C for 20 h, with the heating and cooling rate at 10°C/min, for densification and to obtain the non-transformable tetragonal phase of the YTZ ternary system [3]. The heat treatment was carried out in high purity alumina crucibles.

To compare the influence of high-energy ball milling and planetary ball milling processes on the microstructural properties of dense ceramics, the mixture and mechanoactivation of 16YTZ composition was carried out by Emax equipment (Retsch) with a 125 mL jar, and the parameters used were 20 min of milling at 1700 RPM using zirconia balls of 1 mm in diameter as the milling media. Based on previous in-house experience, the powder percentage (fill ratio) in the jar was 30 vol.% and 40 vol. %, with the remaining volume occupied by the liquid medium (ethanol) and the milling balls (The latter around 60% on the Emax supplier recommendation) [3]. Sintered samples presented in this report are listed in Table 2.1 and the experimental steps for obtaining the samples are shown in Figure 2.2.

Table 2.1. Conditions used for sintering samples at 1500 °C.

Sintered sample	Process of milling	Powder qty. in the jar	Milling time	Particle size distribution after milling, nm			Sintering time, h
				(D10)	(D50)	(D90)	
15.4P1	Planetary	10:0.77 (balls:powder)	12 h	-	-	-	20
16P1	Planetary	10:0.77 (balls:powder)	12 h	819	1096	1957	20
16.6P1	Planetary	10:0.77 (balls:powder)	12 h	-	-	-	20
17.2P1	Planetary	10:0.77 (balls:powder)	12 h	-	-	-	20
17.8P1	Planetary	10:0.77 (balls:powder)	12 h	-	-	-	20
16P2	High-energy	30 vol.%	20 min	526	708	946	2
16P20	High-energy	40 vol.%	20 min	358	449	867	20

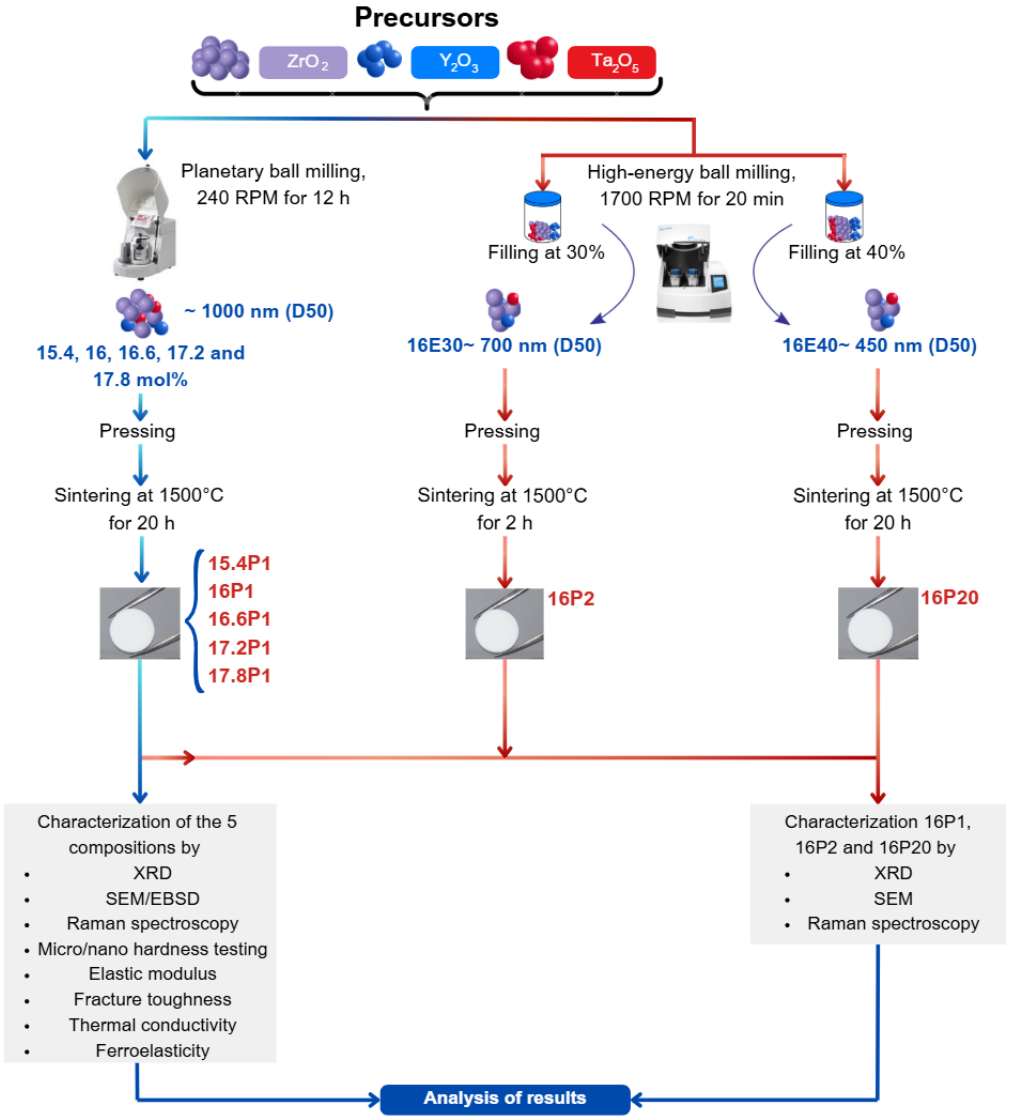


Figure 2.2 Experimental steps for obtaining and characterizing the dense ceramics developed in this project.

2.1.2. Microstructural analysis

X-ray diffraction (XRD, DaVinci D8 Advance, BRUKER, Germany), with CuK_{α} radiation (λ = 1.5406 Å) was carried out to analyze the phase constitution of the different compositions of YTZ. The generator settings were 40 kV and 40 mA, the XRD data were collected in a 2θ range of 20 – 80° with a step width of 0.02° and a counting time of 0.8 s/step. Phase quantification was performed using a mathematical adjustment with the Rietveld method. The structural data used are presented in tables S1 to S6 of the annex 1 [3]. The parameters used to determine a good fit to the experimental data were $\chi^{\wedge 2}$ (GOF), R_{wp}, and R_{exp} (Eq. S1-S3, in the annex 1) [100]. The Rietveld refinement was processed according to the guidelines formulated by the International Union of Crystallography Commission on powder diffraction [3], [101]. The tetragonalities were calculated by determining the interplanar distances from the positions of the (220)/(004) tetragonal peaks, which are observed within the range of 71° ≤ 2θ ≤ 75°. The interplanar distances of the peaks mentioned above correspond to the parameters c and a, respectively, in the tetragonal phase [17], [45].

A scanning electron microscope (SEM, JEOL IT100) equipped with an energy dispersive spectroscopy (EDS) system was used to determine microstructural features of the samples such as porosity level and grain size. Additionally, EDS analysis was carried out to observe the elemental distribution and perform a semi-quantitative assessment of the elements present in dense ceramics. Prior to SEM analysis, the samples were coated with a thin Au-Pt layer via sputtering without requiring any additional pre- or post-treatment.

Raman spectroscopy (WiTec, Alpha 300RA Raman Microscope) equipped with a 355 nm laser source, constant laser power of 4.7 mW, integration time of 60 s, and 1 accumulation was utilized to characterize the phases presents in samples, to identify the vibrational modes of the system and confirm the predominance of the tetragonal phase determined by XRD. Analysis of spectra, including background subtraction, normalization, deconvolution and peak fitting, was performed using the WiTec software [3].

Electron Backscattered Diffraction (Oxford Instruments, Aztec EBSD system, NordlysNano detector) was conducted to determine the phase distribution

and analyze the different crystallographic orientations present in the ceramics. Additionally, it was also used to assess the effect of nanoindentation on the crystalline orientation, particularly in the vicinity of cracks formed by the indentation itself. Special care was taken to ensure that the indentation was positioned right in the center of a single grain to minimize the influence of grain boundaries on crack initiation and propagation.

Atomic force microscopy (AFM, integrated into the Hysitron TI 950 TriboIndenter) was used to examine the microstructure of the ceramics to perform assisted indentations, by selecting the position of one indentation at the center of a grain for EBSD analysis. Additionally, it was employed to identify the locations multiple indentations performed for hardness and elastic modulus measurements, allowing the observation and analysis of the generated prints.

For microstructure revelation in AFM and EBSD, the dense ceramics were prepared for by a multi-step polishing process. It started by polishing with SiC sandpaper on a polish machine set at 80 RPM in the following grit sizes: P240, P600, P1200, P2500, and P4000, followed by steps with diamond paste in progressively finer sizes of 9 µm, 6 µm, 3 µm and 1 µm. Finally, a colloidal silica polish (~30 nm) was used to ensure an optimal surface for analysis.

2.1.3. Mechanical analysis

The mechanical properties of the YTZ dense ceramics were evaluated at both micro- and nanometric scales to analyze hardness, elastic modulus, and fracture toughness, as well as to identify ferroelastic contributions related to tetragonality. Two complementary approaches were used: Vickers microindentation and instrumented nanoindentation.

2.1.3.1. Vickers microindentation

Microhardness tests were performed using a KAIRDA THV-1D tester equipped with a Vickers indenter. The same surface preparation procedure used for AFM and EBSD analysis was followed to ensure comparable surface quality. Loads between 0.3 and 0.5 kgf were applied to promote controlled crack propagation from the indent corners, using a dwell time of 10 s.

For each condition, five indentations were performed to improve the statistical reliability of the data. The indents were examined by optical microscopy to measure the diagonal lengths and the crack extensions from the indent center.

The hardness (H) and fracture toughness (K_{ic}) were determined using the following expressions:

$$H = 1.854\frac{P}{d^2} \tag{2.1}$$

$$K_{ic} = \xi\left(\frac{E}{H}\right)^{1/2}\left(\frac{P}{c^{3/2}}\right) \tag{2.2}$$

Where P is the applied load, d the half-diagonal of the indentation, c the crack length, E the elastic modulus (obtained from nanoindentation), and $\xi = 0.016$ a calibration constant. Fracture toughness (K_{ic}) and toughness are related but not equivalent concepts. Fracture toughness is a mechanical property that quantifies the resistance of a material to crack propagation, whereas toughness represents the energy required to extend a crack. In this work, fracture toughness was evaluated from nanoindentation tests using a Berkovich indenter, for which the Anstis equation was employed to estimate K_{ic}, whereas Vickers indentation was used to estimate the fracture energy (**Γ**) based on crack propagation measurements. Since the exact values of the Young's modulus (E) are not well known, the results of Vickers indentations were expressed in terms of the toughness **Γ** (J/m^2), which is a more appropriate parameter for assessing the behavior of ceramic materials under thermal cycling. This parameter reflects the energy needed to extend a crack through the ceramic and was obtained from the calculated toughness values using $\Gamma = K_{ic}^2/E$.

$$\Gamma = \xi^2\left(\frac{2d^2P}{c^3}\right) \tag{2.3}$$

Which is independent of E.

2.1.3.2. Nanoindentation and Load-Displacement Analysis

Nanoindentation tests were carried out using a Hysitron TI 950 TriboIndenter equipped with a Berkovich diamond tip. A total of 16 indentations were performed on specific grains under loads ranging from 400 to 10.000 μN with a load spacing of 644 μN, ensuring that the largest imprint remained smaller than the average grain

size. This allowed local evaluation of the mechanical response without overlapping grain boundaries.

The Oliver–Pharr method [102] was used to extract the hardness and reduced modulus from the loading–unloading curves. The resulting data were analyzed through a Weibull distribution to determine representative average values, reducing the influence of local anisotropy.

Additionally, the first indentation at 10.000 μN was selected in the compositions with lowest and highest tetragonality for detailed examination (15.4P1 and 17.2P1, respectively). The corresponding load–displacement curves were analyzed to identify discontinuities ("pop-ins") associated with sudden penetration events. These events were interpreted as possible signatures of ferroelastic switching, plastic deformation, or fracture initiation.

2.1.3.3. AFM observations and crack-length calibration

The residual nanoindentation imprints were characterized by Atomic Force Microscopy (AFM) to measure the radial crack lengths (c) generated at different loads. The relationship between P and $c^{3/2}$ was analyzed following the Evans model to assess the evolution of fracture toughness with load and composition. These AFM measures also allowed observation of surface relief patterns near the crack tips, providing evidence of domain reorientation and ferroelastic activity.

2.1.3.4. Determination of the Q parameter

The constant Q is a dimensionless parameter that relates the additional deformation during pop-in to the crack opening and serves to verify the consistency of Field's model. To correlate the data obtained by AFM and by the instrumented indentation, the experimental Q-factor was determined according to the chain-rule approach proposed by Field, Swain, and Dukino [103]. Two linear relationships, H_X vs $P^{2/3}$and c vs $P^{2/3}$ were plotted, and their slopes were used to calculate Q as:

$$Q = \left(\frac{dc}{dP^{2/3}} \cdot \frac{dP^{2/3}}{dh_x} + \sqrt{2}\right)\left(\frac{H}{E'}\right) \tag{2.4}$$

The calculated Q values close to unity indicate that the material response follows the premises of the model and that the estimation of toughness from indentation is reliable. Comparing Q between compositions confirms the

consistency of the method and its applicability for estimating K_{ic} directly from indentation data.

2.1.4. Thermal properties

Finally, thermal conductivity and diffusivity from room temperature to 1000°C at 100°C intervals was measured using the laser flash method (Linseis, LFA 100). To prepare the samples, hand coating of a dispersion of fine, pure colloidal graphite (Graphit 33, Kontakt Chemie) was applied, which provides an electrically conductive coating to non-conductive substrates, prevent direct transmission of infrared light pulse and provide better absorption. The dense ceramics were then placed on graphite cylindrical holders and introduced into the equipment for subsequent analysis. The value of thermal diffusivity is obtained using the laser flash (mm^2/s) and the thermal conductivity, κ (W/(m.K)) was calculated using the Eq. 2.5 [9]:

$$\kappa = \alpha \cdot C_p \cdot \rho \tag{2.5}$$

Where α is the thermal diffusivity, C_p is the specific heat capacity (J/g.K) which was measured by the Kopp-Neumann approximation (Eq. 2.6) [104] from room temperature until 1000°C in intervals of 100°C using data of pure ZrO_2, Y_2O_3 and Ta_2O_5 from literature [104], [105] and ρ is the dense ceramic apparent density measured by XRD and corroborated by Archimedes'.

$$C_{p(system)} = \sum_i x_i \, C_{p(i)} \tag{2.6}$$

For any residual porosity (φ) in the sample, the thermal conductivity was further corrected with Maxwell's relation [9] as:

$$\kappa_{dense} = \kappa_{measured} \frac{1}{(1-1.5\varphi)} \tag{2.7}$$

2.2. Plasma spraying coatings of YTZ systems

2.2.1. Deposit and characterization by SPS technique

For any residual porosity (φ) in the sample, the thermal conductivity was further corrected with Maxwell's relation as: The submicrometric powders mechanoactivated by Emax with 30 vol.% and 40 vol.% of vial filling, corresponding to precursor mixtures milled under high-energy conditions but without sintering, were used as feedstock for the coatings deposited by suspension plasma spraying (SPS) [3], as is described in Figure 2.3. The quantities were selected following the equipment supplier's recommendations, which specify that approximately 60% of the jar's volume should be filled with balls, 30% with the material to be ground, and the remainder with the liquid medium. The sample in which 40% of the jar's volume was filled with precursor materials was used to compare the amount of powder in the vial filling.

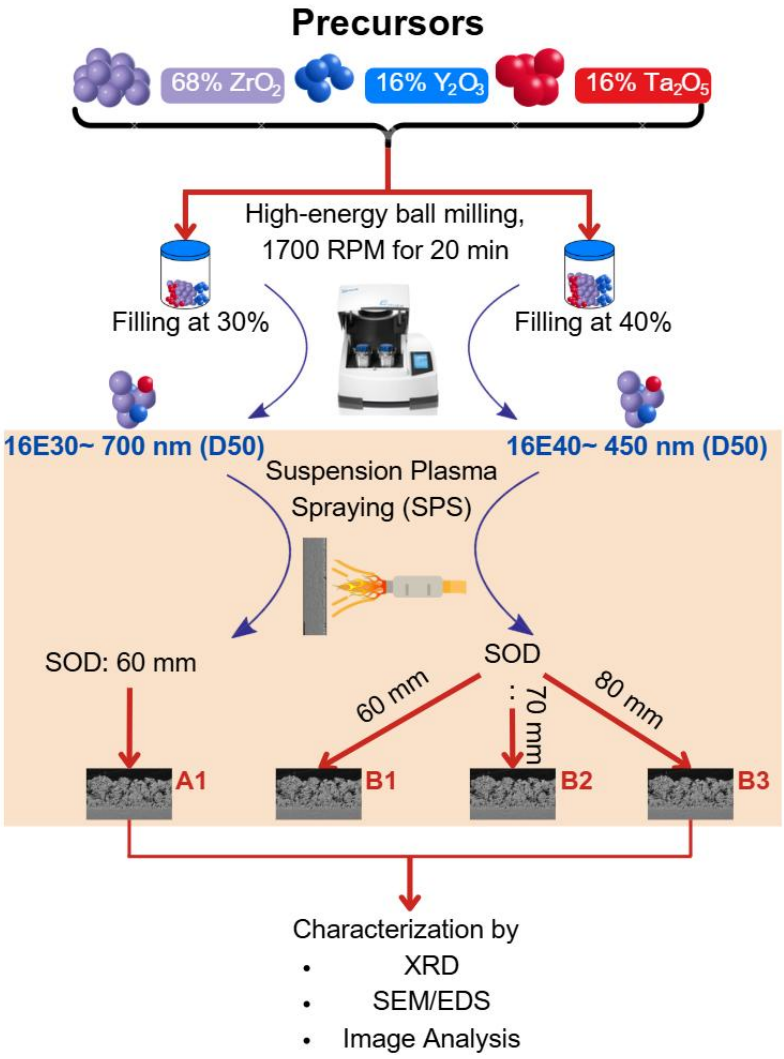


Figure 2.3 Methodology for obtaining and characterizing coatings.

The SinplexPro-180 torch (Oerlikon Metco), which features a cascade-anode and single cathode design, was used to produce the coatings by suspension plasma spray technique (see Figure 2.4). This arrangement is characterized by including an additional stage in comparison with the conventional plasma torches that is called « *neutrode stacking* » allowing the extension of the arc length and a reduced anodic surface, minimizing the fluctuations and instabilities presented in the conventional arrangement [106]. In addition, it is equipped with a suspension injection system developed by the SPCTS laboratory of the University of Limoges. This system consists of two pressurized tanks: one for storage of the suspension and the other containing ethanol for cleaning the system after each deposit. The injector, with a diameter of 150 µm, is manually adjusted to ensure that fragmentation of the suspension occurs properly within the plasma jet (see Figure 2.5).

The suspensions were prepared with a concentration of 20 wt.% powder in ethanol as solvent and 2 wt.% dispersant (Hypermer KD2-LQ-(CQ)) to avoid particle agglomeration [3]. Each suspension was prepared with a total mass of 500 g. First, ethanol, which correspond to the 80 wt.% of the suspension, was weighed. Subsequently, the dispersant was diluted in the ethanol, and the powder was then gradually added to the ethanol-dispersant mixture and dispersed using both magnetic stirring and a high-power ultrasonic probe. This addition was carried out for over 30 min, with 3-sec rest intervals every 10 sec to avoid the formation of lumps. The suspension was maintained under constant agitation until deposition to minimize sedimentation. The preparation procedure is detailed in Figure 2.6.

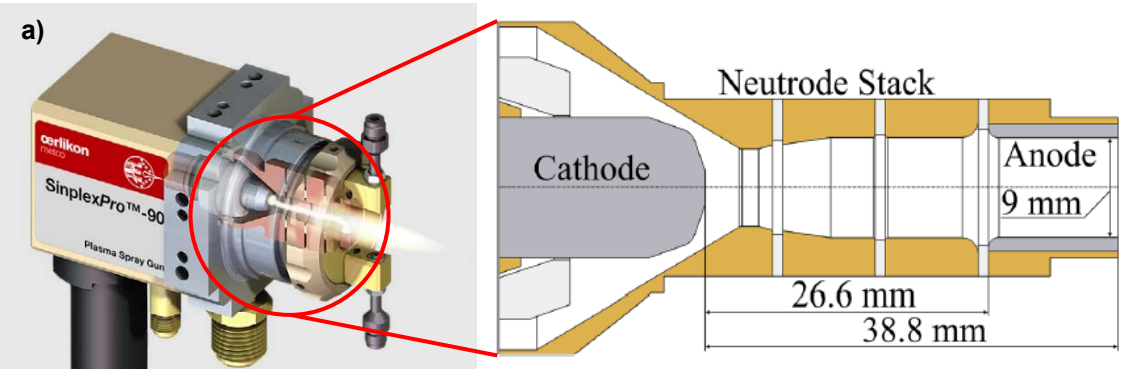


Figure 2.4 a) SinplexPro cascaded arc design [107] and, b) plasma torch scheme. [108]

The deposits were carried out on SS304 stainless steel disc substrates, with 50 mm in diameter and 5 mm thick, with a surface roughness of 0.4 μm ± 0.01 [3].

To reveal the microstructure in SEM of the coatings obtained, the samples were first cut and embedded in Buehler Epothin® resin for 24 h to ensure proper solidification. They were sequentially polished with SiC sandpaper in the following grit sizes: P360, P600, P1200, P2500, and P4000, followed by a final polishing step with 3-micron diamond paste. The polishing process was performed on a machine set at 180 RPM. Once polished, the samples were coated with Au-Pt to obtain the SEM images, enabling the analysis of the coating's microstructure, thickness, porosity and microhardness.

The obtention of fracture toughness and hardness parameters were carried out with the same procedure as in dense ceramics, considering the equations 2.1 and 2.2.

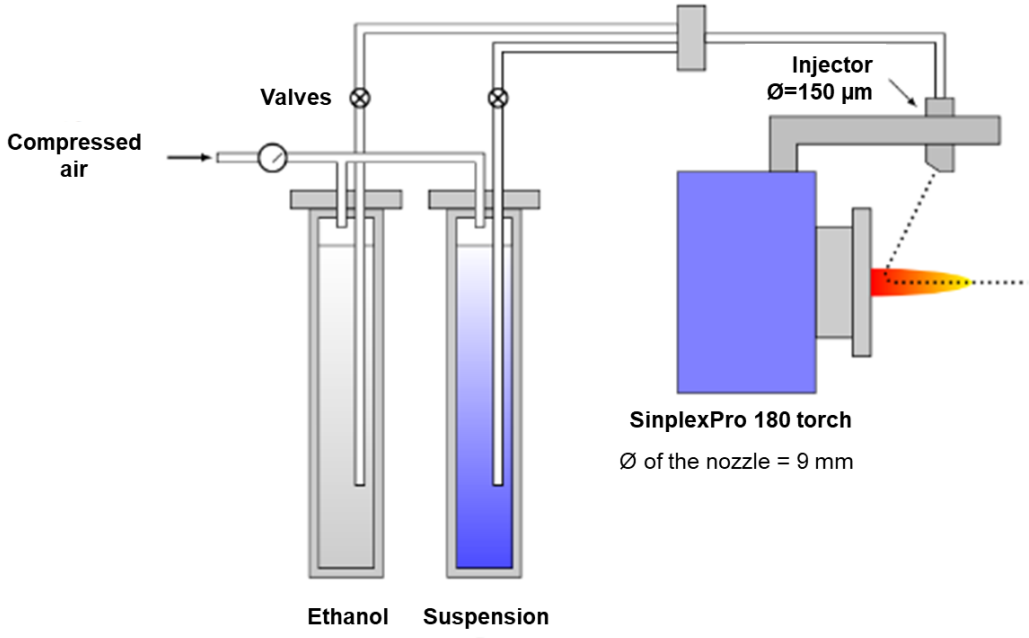


Figure 2.5 Suspension injection system used in this project (adapted from [26]).

The plasma spraying parameters are listed in Table 2.2. These parameters were selected based on previous experiments with 8YSZ [26], [30], due to the lack of information on the SPS deposit of the YTZ system. The stand-off distance was varied from 60 to 80 mm to study its effect on the deposition efficiency, *t'*-phase percentage, and the porosity in the coatings. The analysis was done with coatings obtained with the 16E40 powder at stand-off distances of 60, 70, and 80 mm, identified as B1, B2, and B3, respectively. For comparative purposes, a coating with the 16E30 powder was prepared at a fixed stand-off distance of 60 mm (sample A1) [3].

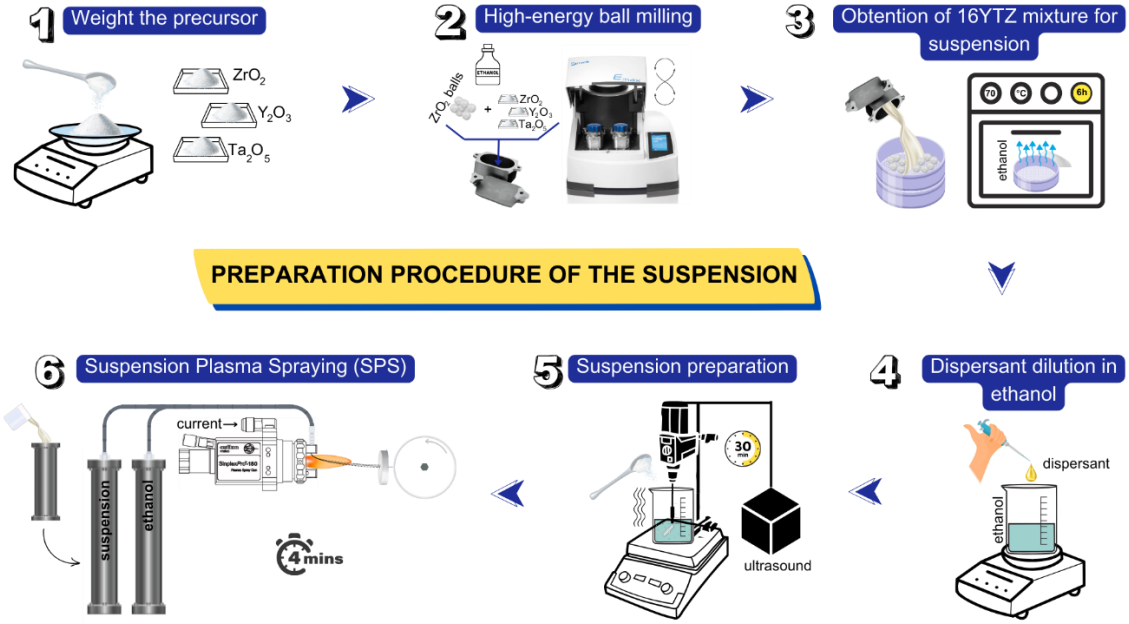


Figure 2.6 Preparation procedure of the suspension.

Table 2.2 Plasma spraying parameters used in this project [3].

Anode nozzle diameter, mm	9
Ar,He gases flow rate, slpm	40/20
Current intensity, Amps	500
Electric power, kW	37
Stand-off distance, mm	60-80
Preheating temperature, °C	300-450

2.3. Samples nomenclature

Due to the fact that when we worked with the same quantity of Y_2O_3 and Ta_2O_5, we could work with the quasi-binary $YTaO_4$-ZrO_2 phase diagram. All compositions in this work are named using this molar percentage system, which relates half of one $YTaO_4$ unit to one full ZrO_2 unit, it means: $Y_{0.5}Ta_{0.5}O_2$-ZrO_2. Table 2.3 presented below shows the conversion of compositions from the ternary ZrO_2-$YO_{1.5}$-$TaO_{2.5}$ system to the quasi-binary $Y_{0.5}Ta_{0.5}O_2$-ZrO_2 system.

For practical phase identification purposes, in this work the cubic, tetragonal and monoclinic phases of zirconia will be denoted by the lower-case letters *c*, *t* and *m*, respectively. The orthorhombic phase of Ta_2O_5 will be denoted by the lower-case letter *o*.

Table 2.3 Conversion of molar scale from ZrO_2-$YO_{1.5}$-$TaO_{2.5}$ Ternary phase diagram to $YTaO_4$-ZrO_2 quasi-binary phase diagram.

Dense ceramics							
	ZrO_2-$YO_{1.5}$-$TaO_{2.5}$ Ternary phase diagram					**$YTaO_4$-ZrO_2 quasi-binary phase diagram**	
Name	**Mol% ZrO_2**	**Mol% $YO_{1.5}$**	**Mol% $Ta_{2.5}$**	**X**	**Chemical formula $Y_{(1-x)}Ta_{(1-x)}Zr_{2x}O_4$**	**Mol% $YTaO_4$**	**Mol% ZrO_2**
15.4P1	69.2	15.4	15.4	0.69	$Y_{0.38}Ta_{0.38}Zr_{1.38}O_4$	30.8	69.2
16P1	68.0	16.0	16.0	0.68	$Y_{0.36}Ta_{0.36}Zr_{1.36}O_4$	32.0	68.0
16.6P1	66.8	16.6	16.6	0.67	$Y_{0.34}Ta_{0.34}Zr_{1.34}O_4$	33.2	66.8
17.2P1	65.6	17.2	17.2	0.66	$Y_{0.32}Ta_{0.32}Zr_{1.32}O_4$	34.4	65.6
17.8P1	64.4	17.8	17.8	0.64	$Y_{0.28}Ta_{0.28}Zr_{1.28}O_4$	35.6	64.4
Coatings							
A1	68	16	16	0.68	$Y_{0.38}Ta_{0.38}Zr_{1.38}O_4$	32	68
B1	68	16	16	0.68	$Y_{0.36}Ta_{0.36}Zr_{1.36}O_4$	32	68
B2							
B3							

CHAPTER 3: Results – Characterization of raw materials

Characterization of the raw materials used for both the synthesis of dense ceramics and the deposition of coatings based on the ternary YTZ system was carried out. The study began with the characterization of the precursor oxides (ZrO_2, Y_2O_3 and Ta_2O_5) comparing samples prepared without preheating and precursors preheated at 1000 °C for 2 h. Subsequently, the 16YTZ composition was analyzed after planetary ball milling, with and without preheated precursors, both before and after sintering at 1500°C for 20 h. Then, the powders of the five compositions studied (15.4, 16, 16.6, 17.2 and 17.8 mol% YTZ), milled by planetary ball milling, were characterized with the preheated precursors before and after sintering at 1500°C for 2 and 20 h.

Additionally, the microstructural parameters of the 16YTZ composition obtained by two different milling processes (planetary and high energy ball milling) with preheated precursors were evaluated. Finally, the raw powders used in the suspensions for coating deposition by the suspension plasma spray (SPS) technique, corresponding to the 16YTZ composition and prepared by high-energy ball milling, were also characterized. The development outline of this chapter is presented in the Figure 3.1.

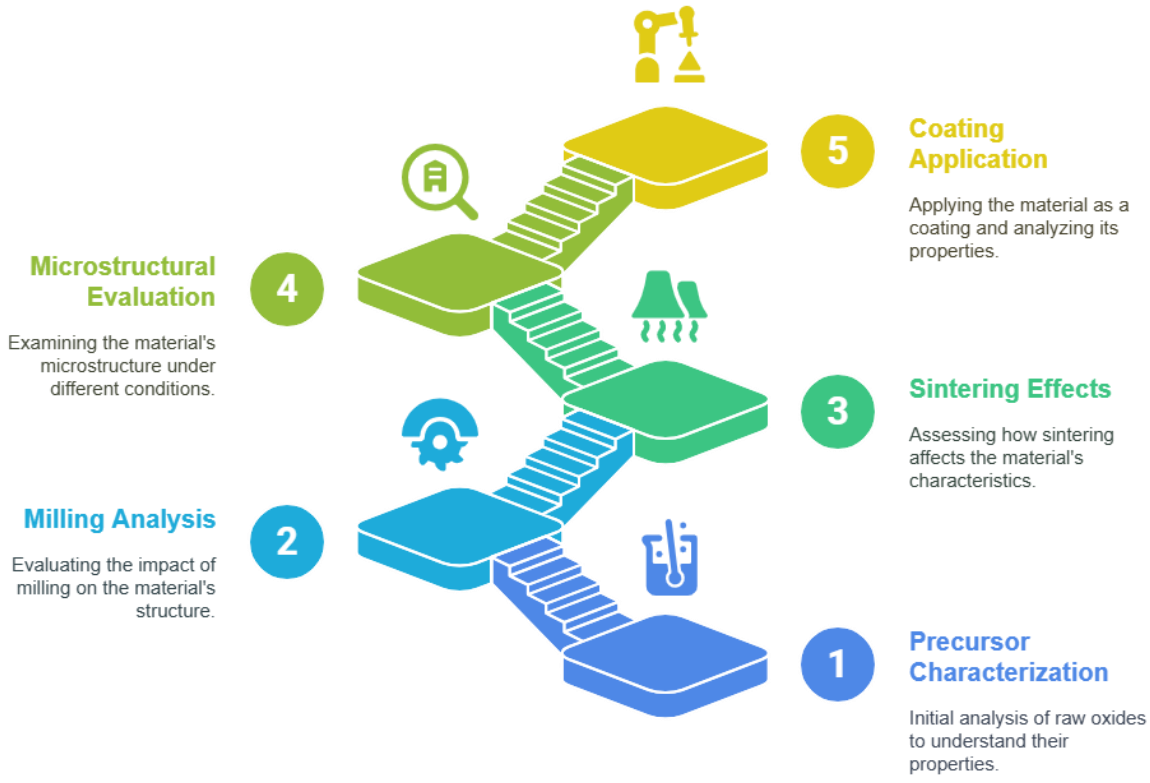


Figure 3.1. Scheme of the development of this chapter.

3.1. Characterization of the precursors ZrO_2, Y_2O_3 and Ta_2O_5

An X-ray diffraction (XRD) analysis was performed on the ZrO_2, Y_2O_3, and Ta_2O_5 precursors separately, before and after heat treatment at 1000 °C (see Figure 3.2). The results indicate that preheating did not cause phase transformations in the ZrO_2 and Y_2O_3 precursors (Fig. 3.2 (a), (b), (d) and (e)), which maintained their stable crystalline structures under these thermal conditions. In contrast, Ta_2O_5 experienced a phase transformation from an orthorhombic structure to a Ht-monoclinic phase, as shown in Figure 3.2 (c) and (f). This phase transition has previously been reported to be dependent on the temperature and thermal history of the material [109], [110].

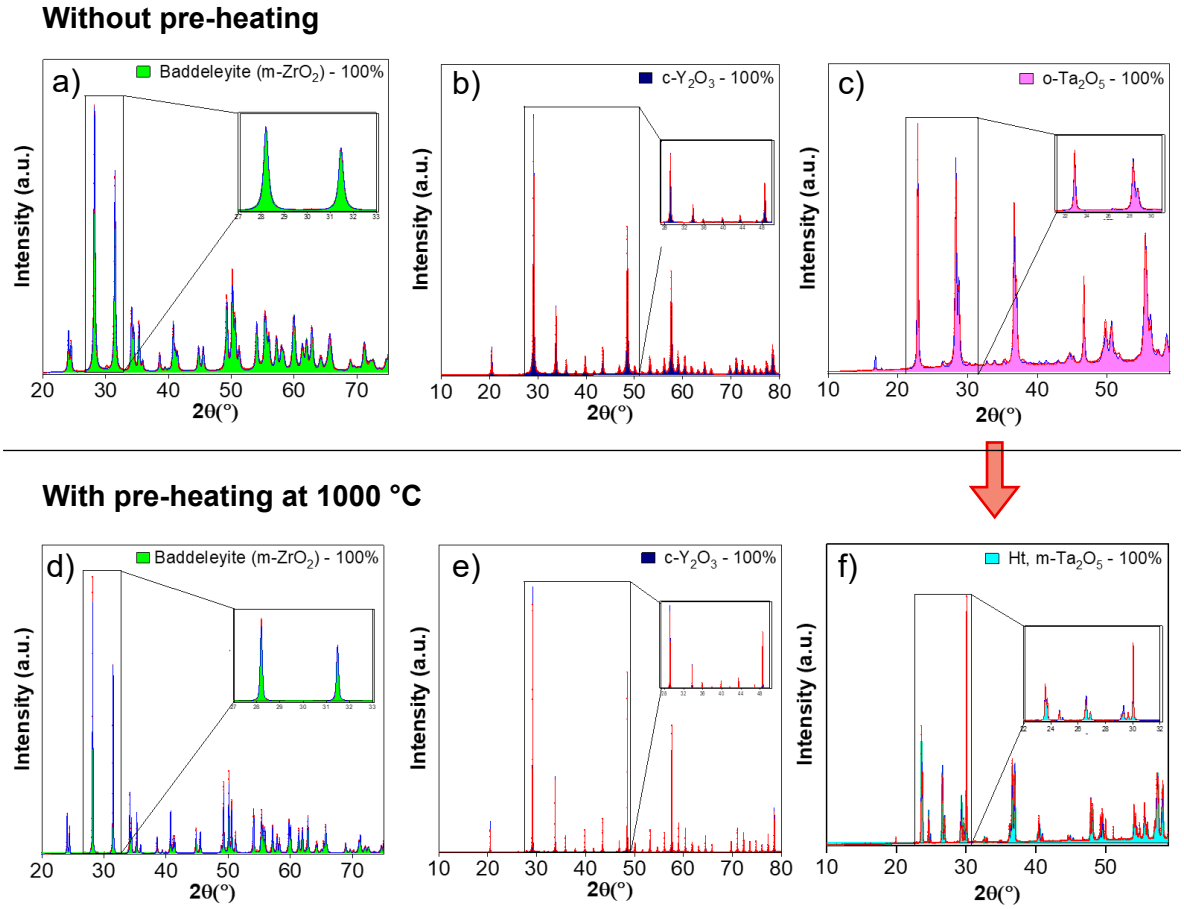
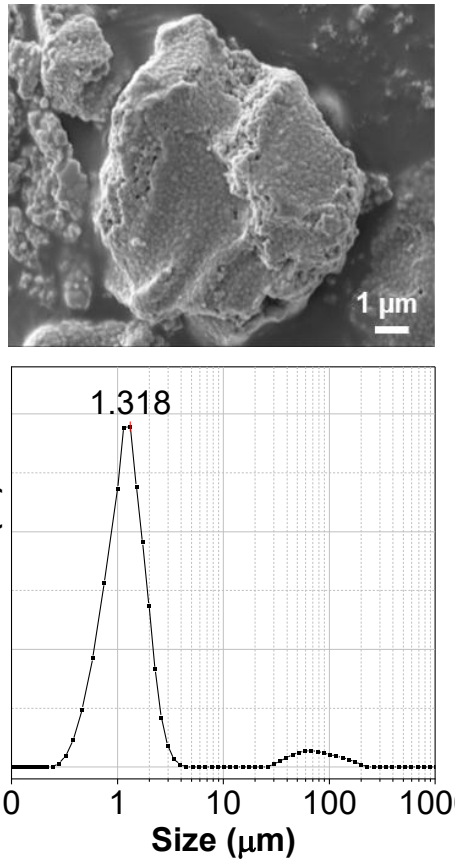
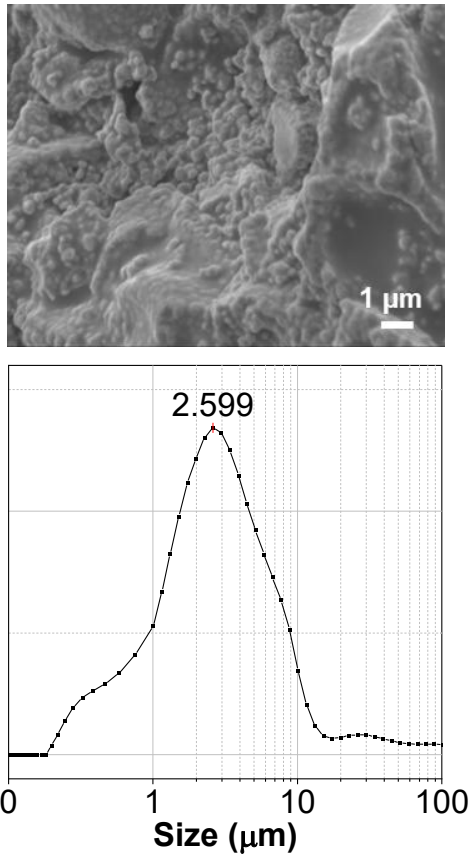


Figure 3.2. X-ray diffraction patterns of precursors powders without preheating ((a) ZrO_2, (b) Y_2O_3, (c) Ta_2O_5) and with preheating at 1000 °C ((d) ZrO_2, (e) Y_2O_3, (f) Ta_2O_5).

The microstructure of the precursors was also analyzed using scanning electron microscopy (SEM), and the particle size distribution was evaluated in samples both with and without heat treatment at 1000 °C as shown in Figure 3.3. For both preheated and unheated samples, SEM micrographs reveal

the presence of agglomerates, as well as particles with submicrometric dimensions on average, while the results of the particle size distribution indicate sizes in the micrometric range on average (the corresponding values are shown in the Table 3.1), suggesting that this latter analysis does not reflect the individual size of the particles, but of the agglomerates formed. This behavior highlights the strong tendency of these particles to agglomerate, even after subjecting the suspensions to sonication in an ultrasonic bath prior to measurement.

Among the three oxides, Ta_2O_5 showed the lowest values in both SEM micrographs and D50 in both cases with and without preheating, suggesting a lower tendency to agglomeration, possibly due to its different chemical nature or initial powder morphology.

	Without preheating	**With preheating at 1000 °C**
ZrO_2		

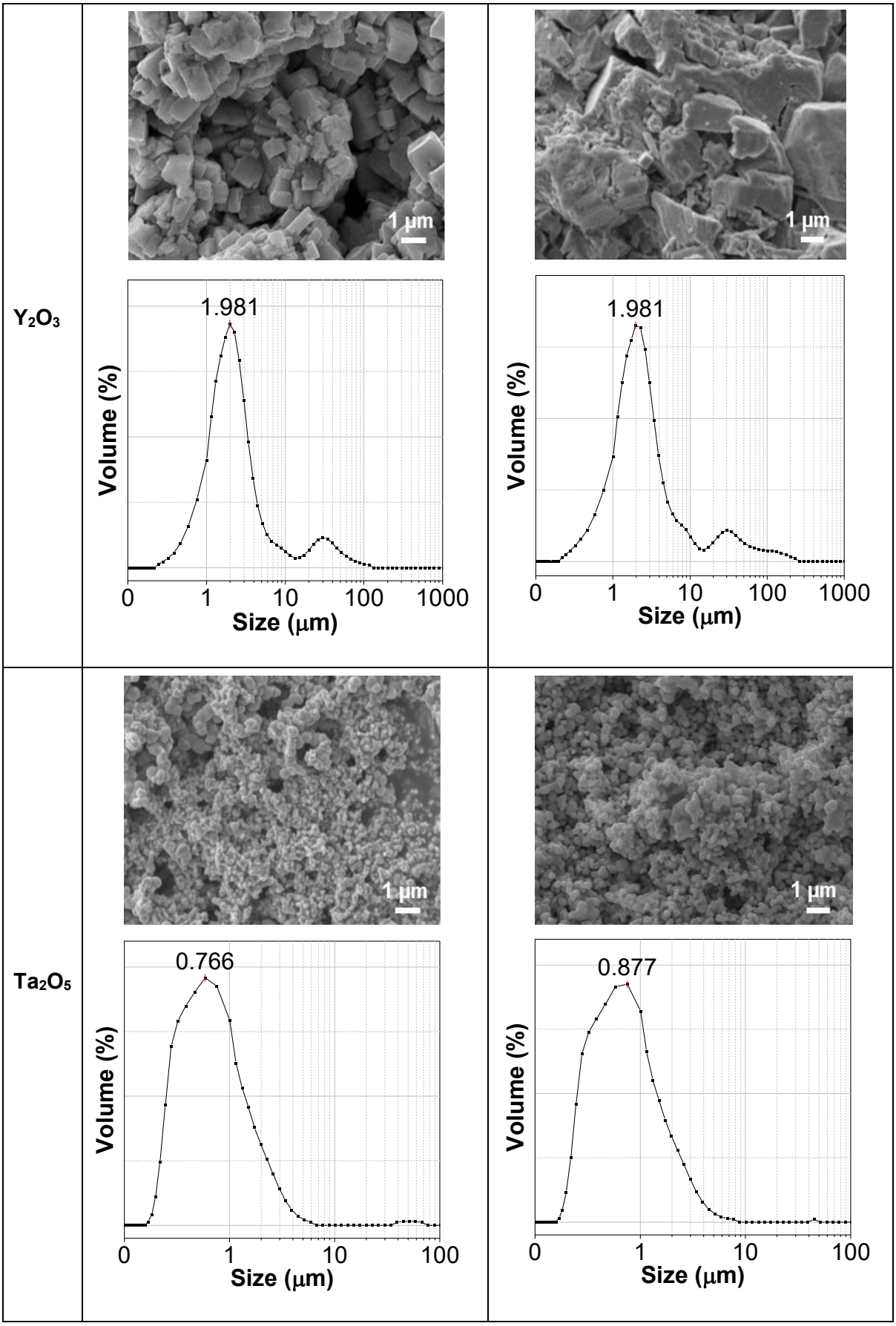


Figure 3.3. SEM micrographs and particle size distribution of precursors without and with preheating at 1000 °C.

Table 3.1. Particle size values calculated from SEM micrographs and particle size distribution of precursor powders without preheating and preheated to 1000 °C.

	Without preheating		With preheating at 1000 °C	
	SEM (μm)	**D50 (μm)**	**SEM (μm)**	**D50 (μm)**
ZrO_2	0.57 ± 0.04	1.32 ± 0.05	0.41 ± 0.02	2.60 ± 0.11
Y_2O_3	0.92 ± 0.05	1.99 ± 0.08	1.39 ± 0.21	1.99 ± 0.08
Ta_2O_5	0.41 ± 0.01	0.76 ± 0.03	0.40 ± 0.02	0.88 ± 0.03

It should be noted that, although preheating to 1000 °C does not result in a significant increase in individual particle size (as observed in SEM micrographs), an increase in the D50 value is observed in the precursors. In the case of ZrO_2, for example, this value nearly doubles after preheating. This behavior can be explained by the presence of solid-state sintering effects, where heat-activated surface diffusion favors the formation of “bridges” between fine particles at their contact areas. As a result, bigger agglomerates are generated, which are detected by particle size distribution analysis. This type of phenomenon has already been reported in the literature for fine ceramic powders, where even moderate temperatures (like 1000 °C in this case) can be enough to start the formation of solid-solid interfaces or necks between particles [111].

Also, it is important to mention that the strong tendency to agglomerate of the precursors used in this work can represent a challenge for subsequent stages such as colloidal dispersion in the preparation of suspensions for SPS, potentially affecting the stability, homogeneity, and microstructure of the final coating. Therefore, the properties of the powders obtained by milling in a planetary ball mill and a high-energy ball mill will be evaluated, with the objective of identifying a suitable method for obtaining submicrometric particles that conserve their size without excessive agglomeration during the preparation of the suspension and its subsequent deposition using the SPS technique.

3.2. Characterization of YTZ powders compositions used for dense ceramics

3.2.1. Comparison between 16YTZ composition milled with preheated and without preheated precursors

Of the five compositions prepared, the one corresponding to the 16YTZ system was selected to evaluate the phases present after the planetary ball milling process, under the conditions detailed in section 2.1.1. of the chapter 2. At this stage, it was not deemed necessary to present all compositions; therefore, the composition most frequently reported in the literature was selected for further analysis. The XRD analysis, shown in Figure 3.4(a), indicates that the milling of the precursor powders without preheating (sample 16M) did not produce the formation of new phases, maintaining the same ones identified in the original precursors. Furthermore, the mass ratio of each phase coincides within the experimental margin, with the stoichiometric estimate calculated for this composition.

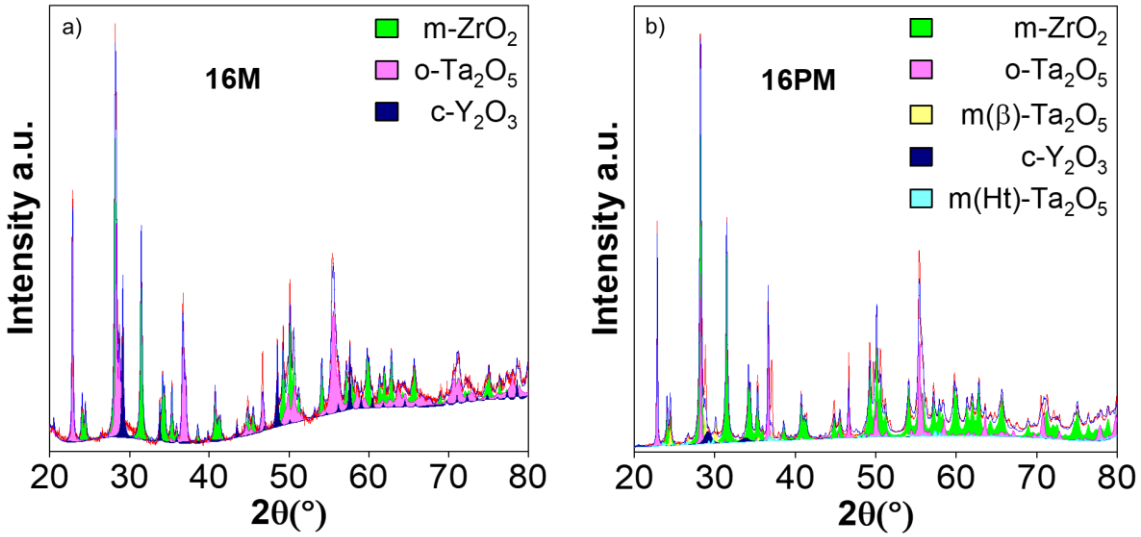


Figure 3.4. XRD patterns of a) 16M and, b) 16PM identifying their respective phases after planetary ball milling process.

In contrast to the composition prepared from powders without preheating, the composition obtained after milling the precursors previously heated at 1000 °C by 2 h observed in Figure 3.4(b) (16PM) exhibits the orthorhombic phase of Ta_2O_5. The percentages for each of the phases are shown in Table 3.2.

This phase is attributed to the partial recrystallization of the monoclinic phase generated after preheating and mechanical milling. This behavior is consistent with the observations reported by Ikeya et al. (1989) [110], who observed that commercial Ta_2O_5 (initially in the orthorhombic phase) undergoes a transformation to the monoclinic phase when heat treated at temperatures ≥ 1000 °C. They also report that when monoclinic Ta_2O_5 is subjected to prolonged mechanical milling, the material tends to become amorphous and, after enough energy accumulation, can recrystallize into the orthorhombic phase. This phenomenon is explained by the change in the local coordination of Ta during amorphization, where the structure tends to reorganize itself into more stable configurations at the local level (such as the hexagonal bipyramids characteristic of the orthorhombic phase) before reaching complete crystalline order. The results obtained in this work reinforce the idea that the previous thermal history of the precursors, especially Ta_2O_5, determines their structural outcome when milled. In conclusion, while unheated powders maintain their original orthorhombic structure, those that have been preheated behave differently when subjected to milling, generating phases that show the effect of recrystallization induced by mechanical energy.

Table 3.2. Mass percentages of each phase present in the 16YTZ composition before sintering.

(wt.%)	***m*-ZrO_2**	***c*-Y_2O_3**	***o*-Ta_2O_5**	***m*-Ta_2O_5**
Stoichiometric	61.8	13.1	25.3	-
16M	61.3	15.9	22.8	-
16PM	67.1	8.0	11.6	11.4

The changes observed in the amounts of *m*-ZrO_2 and *c*-Y_2O_3 after milling can be understood by considering how mechanical energy affects the way atoms are distributed within the material. Although the sample has, on average, 16 mol% Y_2O_3 (enough to stabilize the cubic phase of zirconia) prolonged milling can cause yttrium to shift within the ZrO_2 structure or accumulate in areas with defects, such as grain boundaries or dislocations. This effect does not necessarily mean that yttrium (Y^{3+}) has been lost, but rather that some of it may have moved to places where it no longer contributes to maintaining the cubic phase. Thus, the decrease in the amount of *c*-Y_2O_3 and the simultaneous increase in the monoclinic phase of ZrO_2 could be explained as a result of this internal reorganization that occurs during

milling, without implying a real change in the overall composition of the system [78], [112], [113].

After structural analysis, this composition was sintered at 1500 °C for 20 h as reported in the literature [70], [114] to synthesize the non-transformable tetragonal phase, inherent in this type of system. Figure 3.5 shows the XRD corresponding to the composition made with unheated and preheated powders and the Table 3.3, the mass percentage of each phase present with the lattice parameters.

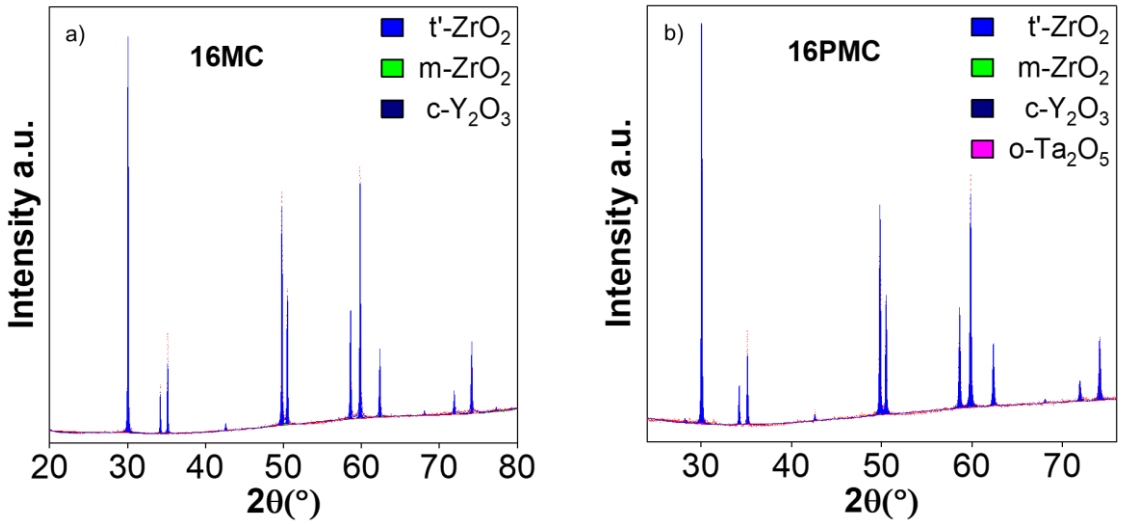


Figure 3.5. XRD of a) 16MC and b)16PMC sintered at 1500 °C for 20 h in a chamber furnace.

Both XRD patterns show the main peak at 2θ = 30.05° and peaks with lower intensity at 2θ = 34.2°, 35.1°, 42.6°, 49.8°, 50.5°, 58.6°, 59.9°, 62.3°, 71.9° and 74.1° corresponding to the tetragonal crystalline system of ZrO_2 with space group (P 42/n m c) attributed to the non-transformable tetragonal phase (*t'*). In addition, low intensity peaks are observed at 2θ = 28.3° and 31.5°, which correspond to the monoclinic phase of ZrO_2 (*m*-ZrO_2) with space group (P 1 21/c 1), while the peak at 29.2° can be assigned to the cubic phase of Y_2O_3 (*c*-Y_2O_3, I a -3) [3]. For the sample 16PMC, a slight peak is observed at 28.2°, corresponding to the orthorhombic phase of Ta_2O_5 (*o*-Ta_2O_5, P m m 2).

Table 3.3. Mass percentages of each phase present in the 16YTZ composition and lattice parameters after sintering.

(wt.%)	***t'*-ZrO_2**	***m*-ZrO_2**	***c*-Y_2O_3**	***o*-Ta_2O_5**	d_c	d_a	**Tetragonality (d_c/ d_a)**
Stoichiometric	61.8	25.3	13.1	-	-	-	-
16MC	95.7	2.4	1.9	-	1.31209	1.27791	1.0267
16PMC	97.3	1.4	1.1	0.2	1.31132	1.27795	1.0261

The tetragonality of the samples was determined from XRD peaks appearing at angles 2θ = 71.9° and 74.1°, related to the *t'*-phase, where d_c denotes the interplanar distance of the (004) plane, representing the c axis of the tetragonal distance, while d_a indicates the interplanar distance of the (220) plane, representing the a axis [3]. The tetragonality value is important in this system because it has been directly correlated with the fracture toughness which tends to increase with higher tetragonality values [3].

In this study, the decision was made to use preheated precursors, as they produce a higher t′-phase content in the synthesis of the composition. Previous studies also report on the use of a preheating stage at 1000 °C for 2 h [13]. However, the results obtained here suggest that preheating should not be strictly necessary, as the differences observed between the preheated and non-preheated samples were not significant enough to justify the additional heat treatment.

3.2.2. Granulometry and XRD of 15.4, 16, 16.6, 17.2 and 17.8YTZ powders

The Figure 3.6 shows the particle size distribution in volume percentage for the five compositions with different dopant molar content: 15.4%, 16%, 16.6%, 17.2% and 17.8% mol of Y_2O_3 and Ta_2O_5.

It is observed that all the compositions present a similar particle size distribution in volume around 0.7 μm (D50) which indicates that the milling has the same effect on all compositions and reduced them to a submicrometric scale.

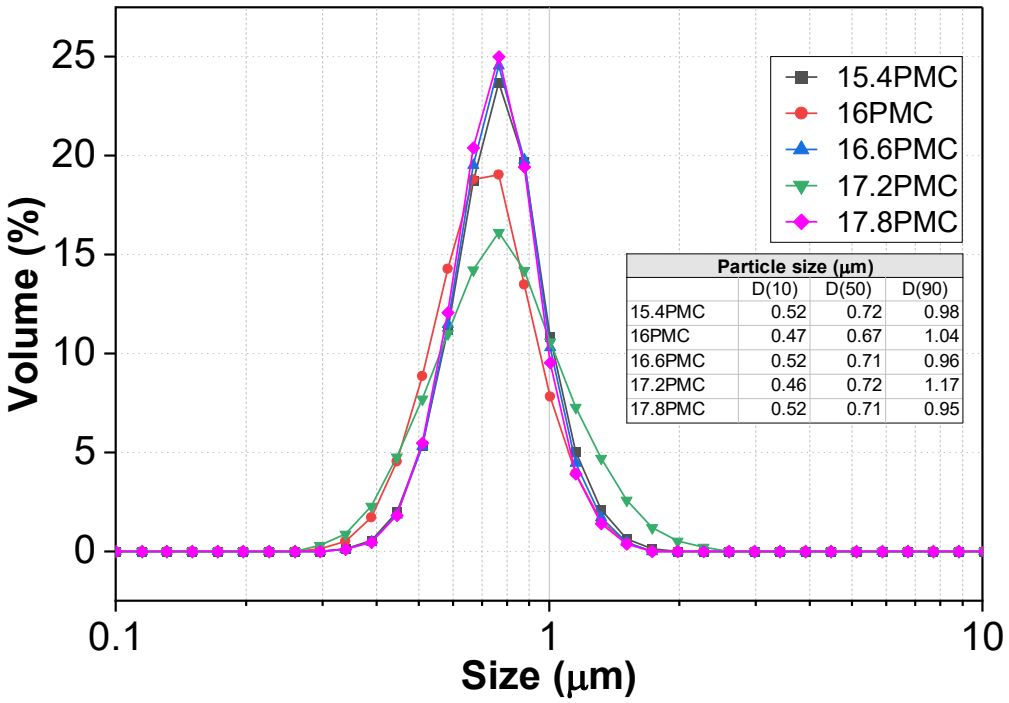


Figure 3.6. Particle size distribution in volume percentage of the five different compositions of YTZ.

A sintering process was carried out at 1500 °C for 20 h with the objective of stabilizing the *t'*-phase. Figure 3.7 shows the XRD patterns corresponding to the five compositions analyzed in powder form. As shown in section a) all samples exhibit diffraction peaks consistent with the tetragonal structure with a slight presence of monoclinic phase and residues of *c*-Y_2O_3 and *o*-Ta_2O_5 which are not visible in the patterns but appeared in the phase analysis (the values are so small that they are not statistically representative). This means that under these sintering conditions, the formation and stabilization of the phase was achieved.

Section (b) highlights the region between 71.5° and 75° where the lattice parameters of the *t'*-phase are represented. These peaks show gradual shifts as the dopant content increases from 15.4 to 17.8 mol% of Y_2O_3 and Ta_2O_5, suggesting a progressive difference in the lattice geometry. The Rietveld adjustment performed on these patterns shows a goodness of fit (GOF) between 1 and 2 for the five compositions, indicating the reliability of the adjustment.

Section (c) illustrates the tetragonal lattice characteristic of a *t'*-system, in which Y^{3+} and Ta^{5+} ions randomly occupy Zr^{4+} sites, promoting the stabilization of the metastable *t'*-phase. Finally, section (d) presents the lattice parameters obtained and the c/a ratio (tetragonality) for each composition, evidencing once again that the increase in dopant percentage is directly related to the increase in the tetragonality of the system.

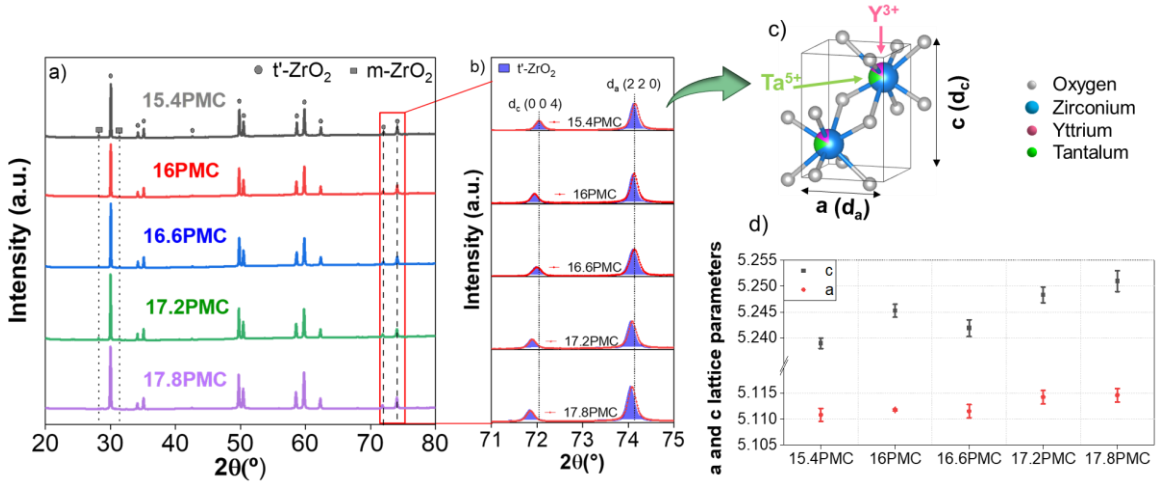


Figure 3.7. XRD patterns of (a) the five different compositions in powder, (b) highlights of the characteristic peaks corresponding to *t'*-phase,(c) tetragonal lattice characteristic of a *t'*-system representing the random occupancy of Y^{3+} and Ta^{5+} ions into Zr^{4+} places, and (d) tetragonality and lattice parameters of *t'*-phase in 15.4, 16, 16.6, 17.2 and 17.8PMC samples.

Compared to conventional YSZ systems, where the t-phase is stabilized by the occupancy of Y^{3+} into Zr^{4+} sites, which results in the generation of oxygen vacancies to maintain the neutrality of the system, the YTZ ternary system reduces significantly the formation of these vacancies due to its stoichiometry, promoting greater structural stability and tetragonality values. This system has tetragonal values (c/a ratio) higher than those typically reported for dense YSZ ceramics, which are in the range of 1.014-1.016 [115], [116]. This higher tetragonality could be translated into better mechanical response at high temperatures, as the *t'*-phase is well known for its resistance to crack growth and good thermal stability.

Sintering tests were also conducted at 2 and 8 h in only one composition (16YTZ) to observe if the complete stabilization of the *t'*-phase could be achieved in a shorter sintering time. The corresponding results are presented in the annex 2, where it can be observed that, under these conditions, the formation of *t'*-phase remains limited, indicating that these sintering times are still insufficient to promote its predominant formation. For this reason, all experiments carried out within the scope of this work related to dense ceramics were conducted using a sintering time of 20 h.

3.3. Comparison between planetary ball milling and high-energy ball milling process

In order to compare the performance of planetary ball milling and high-energy ball milling and considering the limited capacity of the former to process large quantities of material, the decision was made to explore using high-energy ball milling. This method allows the processing of at least 100 grams of powder per vial and 200 grams per milling cycle (using two vials). Moreover, the powder intended for plasma spraying must be adequately mechanoactivated to enable the formation of the *t'*-phase during in-flight conditions. This preliminary assessment was conducted using the 16YTZ composition.

High-energy ball milling was performed with the stoichiometric quantity of precursors without preheating under different milling conditions where the percentage of powder in the vial and the milling time were varied. The percentages of each phase present in each sample, determined by Rietveld refinement, as well as the milling conditions used, are detailed in Table 3.4, where an approximate difference of 2-4% can be observed between the stoichiometric content and the refined phase percentage. This can be considered acceptable within the margins of error of the Rietveld method. This difference is supported by a GOF of 1.48-1.69, which indicates a good overall fit of the pattern. Furthermore, minor variations such as this are to be expected due to the assumption of ideal compositions in stoichiometric calculations.

Table 3.4. High-energy ball milling conditions for 16YTZ powders, mass percentages of each phase present in the four samples and milling times before sintering and GOF of the refinement.

Sample	Time of milling (min)	Powder in the vial (%)	*m*-ZrO_2 (%)	*o*-Ta_2O_5 (%)	*c*-Y_2O_3 (%)	GOF
Stoich.	-	-	61.3	25.6	13.1	-
16E2040	20	40	63.9	22.4	13.7	1.48
16E1040	10	40	63.8	21.0	15.2	1.69
16E2030	20	30	63.7	20.9	15.3	1.50
16E1030	10	30	63.4	21.0	15.6	1.58

The diffraction patterns are shown in Figure 3.8, where it is shown that, independent of the conditions used, no new phases are formed. The phases detected correspond only to the individual precursors (*m*-ZrO_2, *c*-Y_2O_3 and *o*-Ta_2O_5). This suggests that the mechanical energy supplied during the selected milling times did not induce a significant phase transformation. Furthermore, in the expansion of the region between 27.5° and 32.5°, a precise match between the experimental peaks and the reference patterns can be observed, confirming the stability of the initial phases.

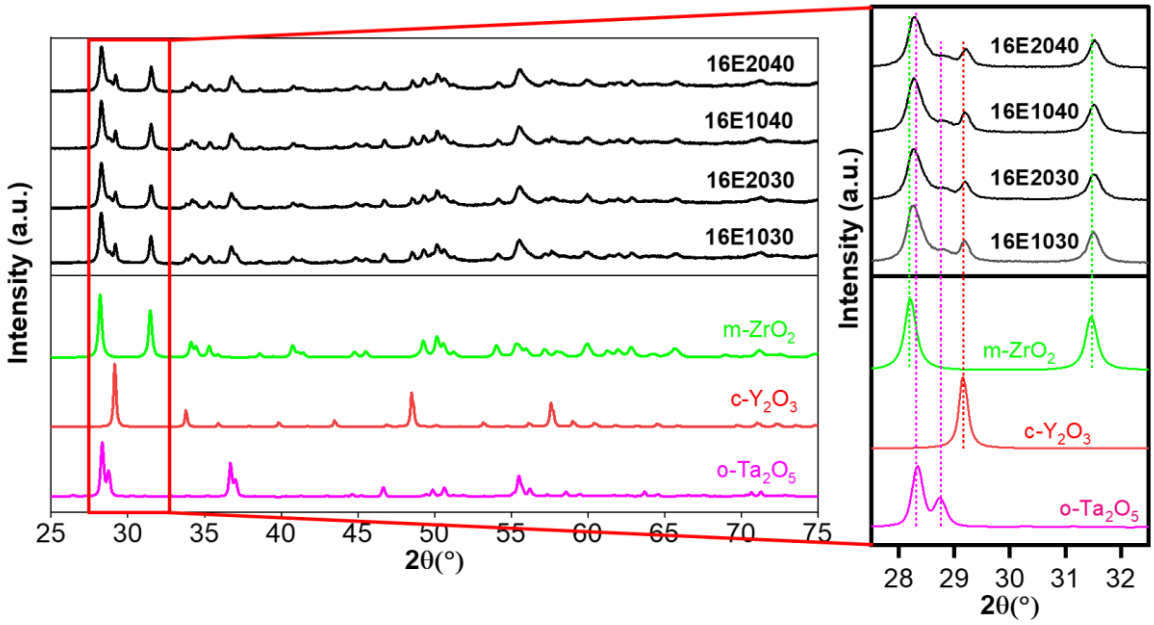


Figure 3.8. XRD patterns of the samples analyzed with the composition of 16YTZ milled by high-energy ball milling (Emax) at different powder vial filling volumes and milling times without sintering.

Once the structural analysis was completed, the sample 16E2040 was sintered at 1500 °C for 2 and 20 h to evaluate if the prior mechanoactivation of the powders through high-energy ball milling could reduce the time required for the *t'*-phase transformation.

XRD analysis presented in Figure 3.9(a) confirms that the transformation can be achieved after just 2 h of sintering. Based on this result, all subsequent experiments using high-energy milled powders were carried out with a sintering time of 2 h. To further optimize the process, two milling times were tested: 10 and 20 min. However, the XRD patterns shown in Figure 3.9(b) for the 10-min milling condition revealed pronounced peaks at 28.2° and 31.4° corresponding to the *m*-ZrO_2 phase, suggesting that this duration was insufficient to achieve proper activation.

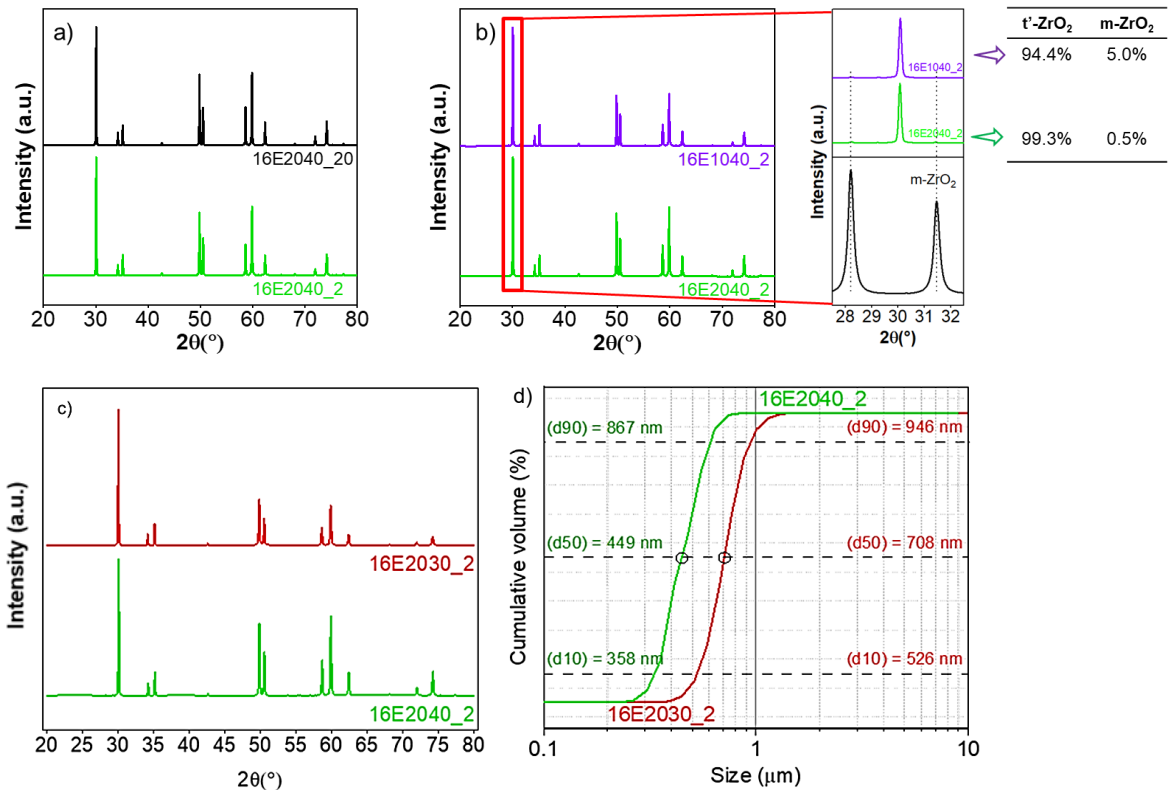


Figure 3.9. XRD patterns of powders milled by high-energy ball milling: (a) comparison of sintering times (2 h and 20 h) to evaluate *t'*-phase formation; (b) effect of milling time (10 min vs 20 min) on 16YTZ composition; (c) XRD patterns and (d) size distribution showing the influence of powder volume in the vial (30% and 40% vol.) on mechanoactivation efficiency.

Therefore, the 20-minute milling condition was selected for all subsequent analyses. Thus, 30% and 40% in volume of powder relative to the jar capacity were used, following the equipment manufacturer's recommendations. The particle size and XRD obtained for each one are presented above in the Figure 3.9(c).

As previously discussed, powder milled using the conventional planetary ball mill were also analyzed and served as a reference to evaluating the efficiency of the high-energy ball milling process. One key difference between both techniques resides in the size of the balls used: the planetary ball mill employed 10 mm balls, whereas the high-energy ball mill (Emax) used smaller 1 mm balls. The smaller diameter increases the number of contact points between balls and powder particles, enhancing fragmentation and resulting in finer particle sizes. This is consistent with literature reports, which indicates that the use of smaller balls in high-energy milling improves milling efficiency and promotes surface activation [117].

A summary of the milling parameters and resulting particle size distributions for each sample is shown in Table 3.5. As observed, the high-energy ball milled powder using 40 vol.% of powder in the jar (sample 16E2040_2) showed the smallest D50 value (449 nm), compared to the planetary ball milled sample (16PMC), which remained at values above 1000 nm.

Table 3.5. Comparison of milling conditions and particle size distribution of powders obtained by conventional and high-energy ball milling [3].

Sample	Process of milling	Powder quantity. in the jar	Milling time	Particle size distribution after milling (nm)		
				(D10)	(D50)	(D90)
16PMC	Conv. ball milling	10:1 (wt.) (balls:powders)	12 h	819	1096	1957
16E2030_2	high-energy ball milling	30 vol. %	20 min	526	708	946
16E2040_2	high-energy ball milling	40 vol. %	20 min	358	449	867

These results confirm that high-energy ball milling not only allows the production of higher quantities of powder in shorter times but also achieves significantly finer particles. This makes the resulting powder especially suitable for SPS feedstock applications, where small and homogeneous particle sizes are essential for optimal coating quality.

CHAPTER 4: Results – Dense ceramics

The results obtained from the characterization of dense ceramics from the YTZ system, corresponding to five compositions identified as 15.4P1, 16P1, 16.6P1, 17.2P1, and 17.8P1 after sintering at 1500 °C for 20 h are presented. The characterization and analysis of results were organized into different sections (see Figure 4.1) in order to establish the relationship between the microstructure, mechanical properties, and thermal behavior of the materials. First, microstructural characterization was performed using X-ray diffraction (XRD), scanning electron microscopy (SEM), and Raman spectroscopy to identify the present phases, evaluate tetragonality, lattice parameters and study vibrational modes. Additionally, backscattered electron diffraction (EBSD) analysis was performed to observe the distribution of the phases present in the dense ceramics and identify the different orientations of the grains on compositions 15.4P1 and 17.2P1, selected for having the minimum and maximum tetragonality values, respectively.

Subsequently, the mechanical properties were evaluated using nanoindentation with atomic force microscopy (AFM), obtaining values for hardness and elastic modulus. These results were complemented by the analysis of fracture toughness and the ferroelastic effect, derived from the load-displacement curves. Finally, thermal characterization was carried out at 200 °C for all compositions, and at 1000 °C only for the extreme samples (15.4P1 and 17.2P1), in order to compare their stability and performance under high temperature conditions.

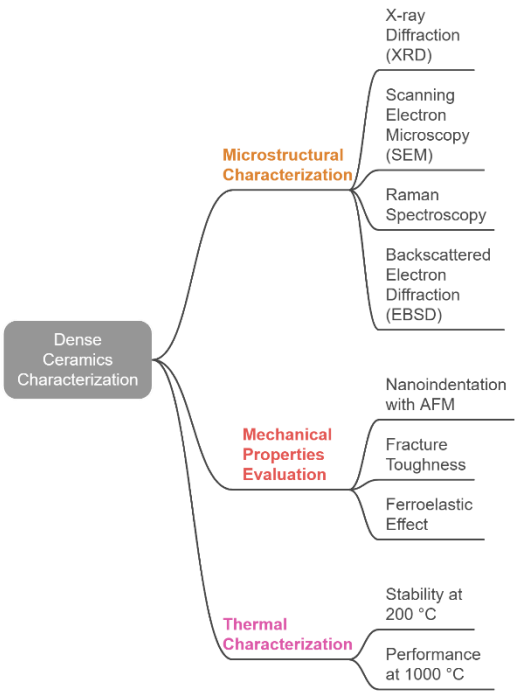


Figure 4.1 Scheme of the development of the results for dense ceramics.

4.1. Characterization of YTZ dense ceramics

4.1.1. Microstructural properties of YTZ system

Figure 4.2 shows the results of the structural characterization of the ceramics prepared under different conditions. XRD patterns of 15.4P1, 16P1, 16.6P1, 17.2P1 and 17.8P1 ceramic samples are presented in Fig. 4.2(a). All the XRD patterns show the main peak at 2θ = 30.1° and peaks with lower intensity around 2θ = 34.4°, 35.1°, 49.9°, 50.5°, 58.9°, and 59.9°, corresponding to the tetragonal crystalline system of ZrO_2 with space group (P 42/n m c) attributed to the non-transformable tetragonal phase (*t'*) [3], [45].

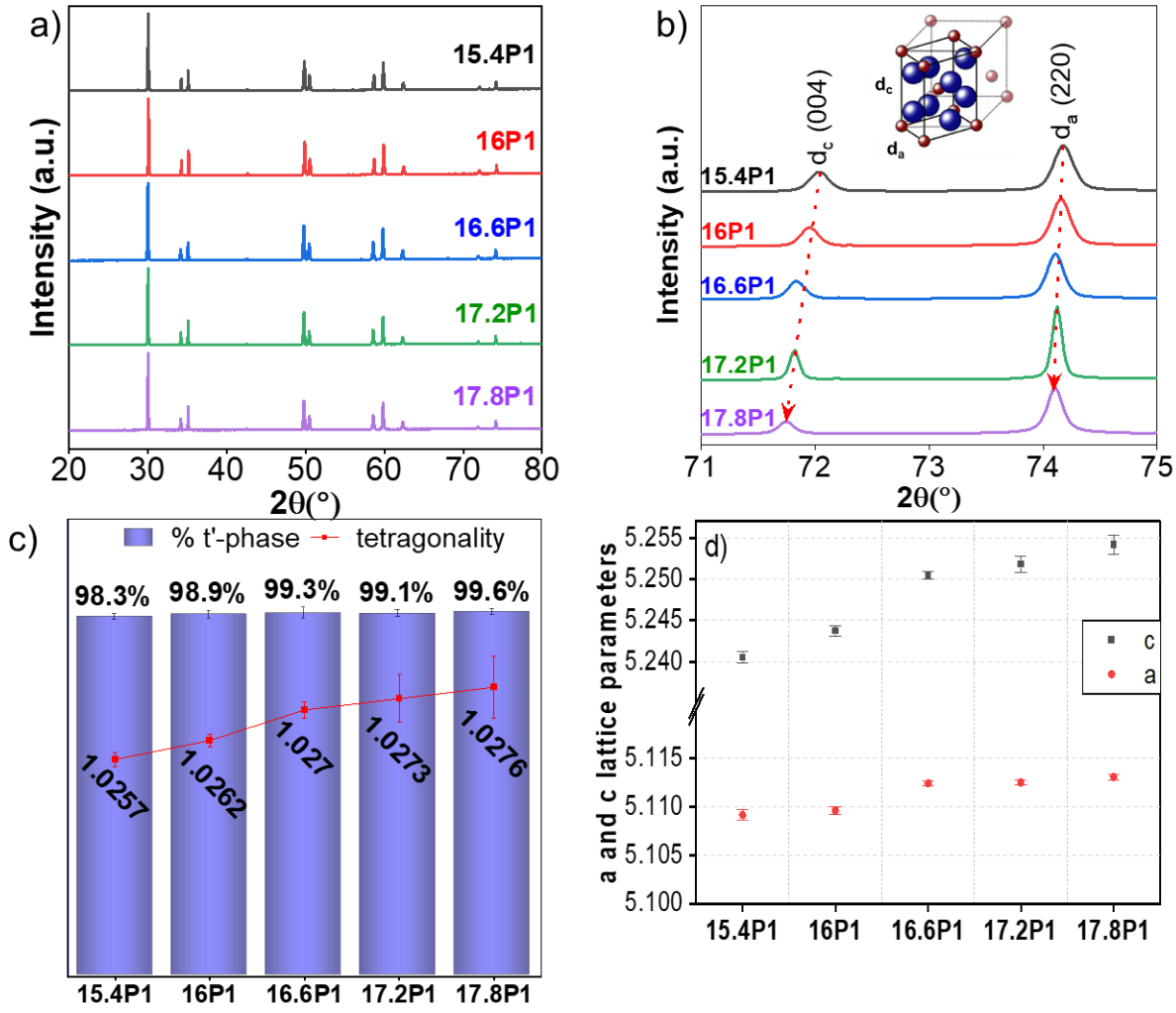


Figure 4.2 XRD analysis of 15.4P1, 16P1, 16.6P1, 17.2P1 and 17.8P1 dense samples. (a) XRD patterns; the characteristic peaks corresponding to *t'*-phase are highlighted in (b), (c) tetragonality and % *t'*-phase, and (d) lattice parameters of *t'*-phase in 15.4P1, 16P1, 16.6P1, 17.2P1 and 17.8P1.

In addition, low intensity peaks are observed around 2θ = 28.3° (11-1) and 31.6° (111), which correspond to the monoclinic phase of ZrO_2 (*m*- ZrO_2) with space group (P 1 21/c 1). The tetragonality of the material was determined from XRD peaks occurring in the range of 2θ = 71-75° (Fig. 4.2(b)) particularly at angles around 2θ = 71.9° and 74.2°, at which two peaks corresponding to the *t'*-phase are present [3], [110], where d_c (~1.30 Å) denotes the interplanar distance of the (004) plane, representing the c axis of the tetragonal crystal, while d_a (~1.28 Å) indicates the interplanar distance of the (220) plane, representing the a axis [3]. It is worth nothing that these diffraction peaks gradually shift toward lower 2θ values as the dopant content increases. The reason for this behavior can be explained in terms of Bragg's law $(2\sin\theta = n\lambda)$: the observed peak shift corresponds to an enlargement of the interplanar distance, *d*. In the tetragonal lattice, this enlargement manifests itself mainly as an elongation of the c-axis relative to the a-axis (see figure 4.2(d)), which increases the tetragonality (c/a). Such a change could be associated with the ionic size of the substituent cations. Y^{3+}, being larger than Zr^{4+}, expands the lattice, whereas Ta^{5+}, being smaller, contracts it. The coexistence of both dopants may induce local distortions and stress fields that help stabilize the tetragonal phase, possibly accounting for the leftward shift of the peaks and the increase in tetragonality values [1–4]. In addition, from the perspective of defect chemistry, Y^{3+} substituting for Zr^{4+} creates oxygen vacancies to preserve charge neutrality $(Y'_{Zr} + V_O^{\cdot\cdot})$, while Ta^{5+} incorporates as $Ta_{Zr}^{\cdot}$, compensating these vacancies. This balance can be expressed by the following reaction in Kröger–Vink notation [17]:

$$xTa_2O_5 + yY_2O_3 \rightarrow 2xTa_{Zr}^{\cdot} + (5x + 3y)O_O^x + (y - x)V_O^{\cdot\cdot} \quad (4.1)$$

This indicates that for every two Ta^{5+} ions incorporated into Zr^{4+} sublattice, one oxygen vacancy created by Y^{3+} is canceled out. By reducing the concentration of vacancies, local distortions in the anionic sublattice are limited and the associated stress fields are reduced, promoting a more homogeneous crystalline environment and, consequently, contributing to the stabilization of the tetragonal phase.

Tetragonality is a key structural parameter in this system because higher c/a values have been correlated with increased toughness [45], [64], [119]. The corresponding improvement in toughness is commonly attributed to ferroelastic

switching, a mechanism that remains active even at high temperatures [120]. The role of ferroelasticity in increasing toughness will be discussed later in this chapter in relation to the analysis of mechanical properties.

The results of the *t'* phase content and the tetragonality associated with the five different compositions are presented in Fig. 4.2(c), where it is observed that the percentage of non-transformable tetragonal phase synthesized by the planetary ball milling processes is close to 98-99 wt.%. This value was determined by Rietveld refinement of the diffraction patterns, considering the presence of the *t'*- and *m*- phases of ZrO_2. A maximum amount of 1.7 wt.% of the m-ZrO_2 phase was found in the 15.4P1 sample [3]. However, there is no statistically significant difference between the five compositions in terms of the amount of *t'*-phase, but there is a difference in terms of tetragonality. Sample 15.4P1, 16P1, 16.6P1, 17.2P1 and 17.8P1 present tetragonality values of 1.0257, 1.0262, 1.0270, 1.0273 and 1.0276, respectively, which are higher than those reported for the YSZ system, typically around 1.013, as documented in the literature [45] and are similar with the one reported for 16YTZ system which is around 1.026 [121]. It can be also seen in Fig. 4.2(d) that the lattice parameters have a perceptible alteration with the increment of dopants. The error for the values of tetragonality is around ± 0.000188%; and for the percentage of *t'* phase around ± 0.8% considering the five compositions [3].

The Figure 4.3(a-f) shows the results of the microstructural characterization from SEM micrographs recorded at a magnification of 2000X of the five compositions after densification by sintering. These micrographs were mainly analyzed for grain size, following the procedure described in ASTM standard E1382. The results from each composition showed a microstructure composed by equiaxed grains with an average size of 9.2 ± 2.9 μm for 15.4P1, 9.4 ± 2.4 μm for 16P1, 11.4 ± 4.0 μm for 16.6P1, 11.7 ± 2.8 μm for 17.2P1 and 12.3 ± 3.6 μm for 17.8P1 [3]. The progressive increase in grain size with the increasing of dopant content suggests that the presence of Y^{3+} and Ta^{5+} promotes segregation at grain boundaries, thereby reducing the energy barrier to grain mobility. This increased boundary mobility facilitates more pronounced coarsening during sintering treatment at 1500 °C, leading to the development of larger and more uniform equiaxial grains in compositions with higher doping [111]. This behavior indicates

that the chemistry of the dopants plays a central role in controlling the grain growth kinetics and the final microstructural stability of the YTZ system.

Along with microstructural analysis, the density and porosity properties of the pellets were evaluated. Bulk density and apparent solid density were determined using Archimedes' method, while open porosity was obtained independently from the ratio between the masses of the dry samples, submerged in water, and dried with a sponge. The density and porosity results (Table 4.1) show that all dense ceramics achieved high levels of compaction, with densification percentages around 99%.

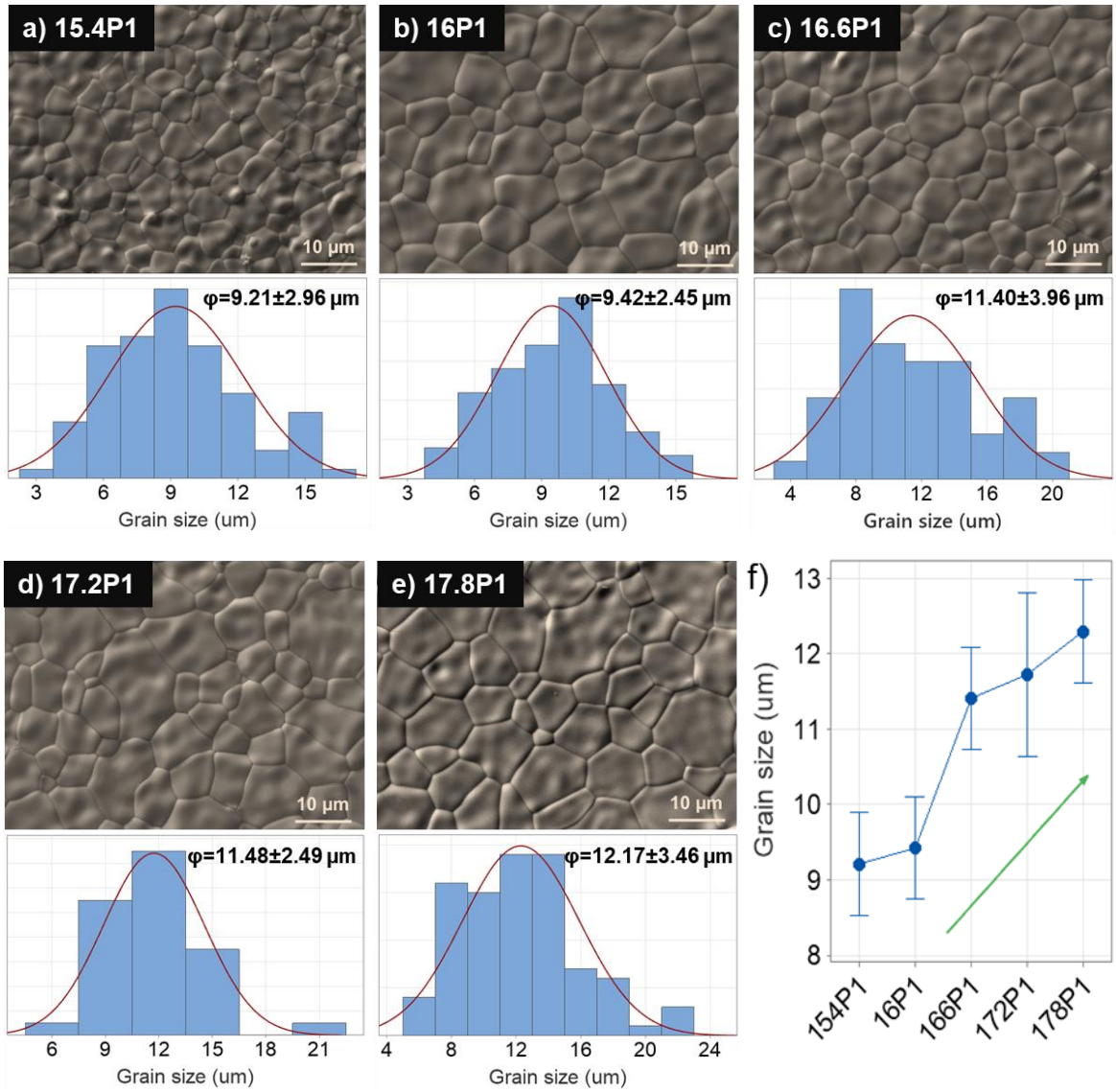


Figure 4.3 Microstructure of samples a) 15.4P1, b) 16P1, c) 16.6P1, d) 17.2P1 and e) 17.8P1 with their respective grain size distribution and standard deviation; and f) is the average grain size for all compositions, showing an increasing trend with the increment of dopants.

Table 4.1 Apparent density, apparent solid density, open porosity, and theoretical density (XRD) of the sintered dense ceramics.

	Apparent density (g/cm^3)	Apparent solid density (g/cm^3)	Open porosity (%)	Theoretical density in XRD (g/cm^3)
15.4P1	6.58 ± 0.28	6.60 ± 0.30	0.44 ± 0.52	6.68
16P1	6.50 ± 0.23	6.52 ± 0.24	0.46 ± 1.11	6.67
16.6P1	6.25 ± 0.42	6.29 ± 0.45	0.99 ± 1.57	6.66
17.2P1	6.57 ± 0.33	6.58 ± 0.32	0.36 ± 1.28	6.65
17.8P1	6.48 ± 0.06	6.48 ± 0.07	0.01 ± 0.24	6.65

The sample with the highest apparent density was 6.58 g/cm³, very close to the theoretical density determined by XRD (~ 6.68 g/cm³) and had a minimum open porosity of ~ 0.4%. As expected, the experimental densities measured by Archimedes' method are slightly lower than the theoretical densities calculated from XRD, since the crystallographic value corresponds to an ideal unit cell without accounting for defects or porosity. The small differences observed can be mainly attributed to the presence of a residual fraction of open and even closed porosity in the pellets, as well as to the sensitivity of Archimedes' method to small variations in water absorption. Nevertheless, the good agreement between both methods confirms that the processing conditions were effective in producing highly densified ceramics with negligible open porosity, in accordance with the microstructural observations by SEM.

As predicted by group theory, the Raman spectra of crystalline *t'*-ZrO_2 contain six fundamental optical modes. According to several reports, the wavenumber positions of these modes are 150, 260, 315, 462 608 (weak shoulder) and 660 cm^{-1} [122]. The position of these modes may vary slightly depending on the reference considered. According to the group theoretical analysis of normal phonon vibrations in *t'*-ZrO_2 crystalline phase, these modes are associated with the E_g, $B_{g1}(1)$, $B_{1g}(2)$ and A_{1g} symmetries, respectively. The typical linewidth of these Raman bands in crystalline *t*-ZrO_2 is about 40 cm^{-1}. Previous observations have shown that the intensity of Raman lines in *t'*-ZrO_2 samples decreases, and their line width increases when the samples are milled into a fine powder or doped with substitutional impurities [123]. Fig. 4.4(a) shows typical Raman spectra where the characteristic vibrational modes of the phases present in the five YTZ samples processed by the different routes can be identified. The peaks are associated with

the non-transformable tetragonal phase, *t'*-ZrO_2. The Raman signatures of each sample between 150 and 900 cm^{-1} show four characteristic bands at ~ 320, ~ 465, ~ 665, and ~ 805 cm^{-1}, which are consistent with previous reports in the literature associated with the *t'*-ZrO_2 phase [124]. From these Raman spectra, it was not possible to identify all the active Raman vibrational modes of the *m*-ZrO_2 phase [3].

The A_{1g}, $B_{1g}(1)$, and $B_{1g}(2)$ vibrational modes are correlated with three stretching vibrational modes of the tetragonal phase of ZrO_2. In turn, the Eg(3) mode is associated with a bending vibrational mode. The shift in these vibrational modes may be due to internal strains generated by the *t'*-phase and to a lesser extent m phase of ZrO_2 present in the material [3], [121]. Figure 4.4(b) shows the spectra deconvoluted into the five bands mentioned. These bands have been labeled according to the symmetries of the normal vibrational modes in crystalline *t'*-ZrO_2, as described above. To our knowledge, the mode observed at approximately 800 cm^{-1} has not been reported before. Considering that Raman provides information on local and long-range disorders, this mode could be attributed to a disorder-active mode due to doping [122], [123]. However, further investigation and validation by theoretical studies of these compositions is required.

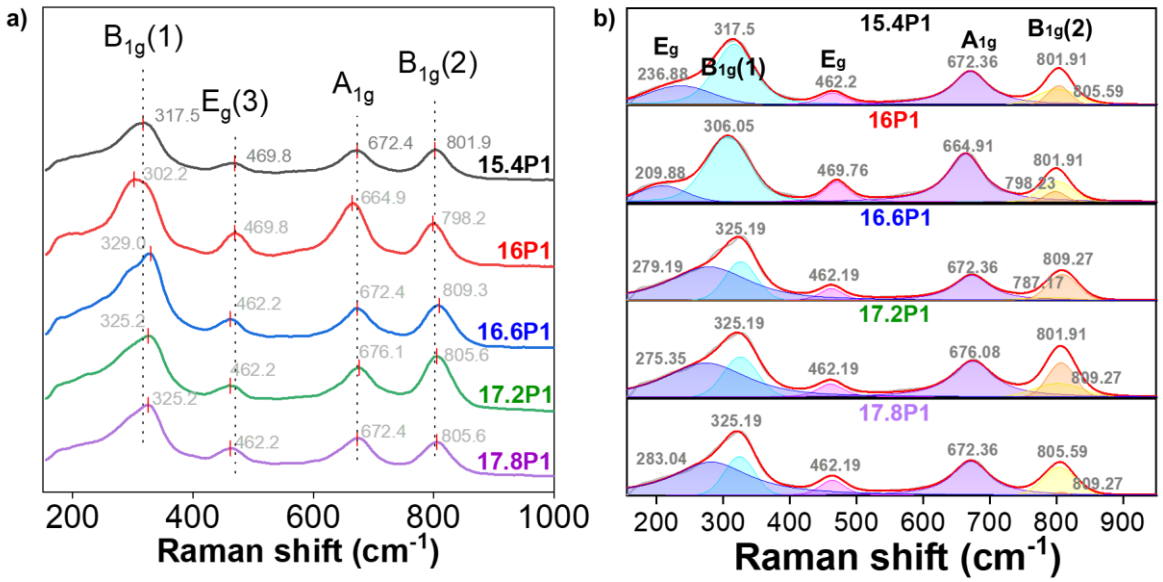


Figure 4.4 a) Raman spectra of the five compositions of YTZ recorded at room temperature after sintering at 1500 °C for 20 h and, b) Deconvolution of Raman spectra in the 5 different bands found in *t'*-phase for the five compositions.

Figure 4.5(a) shows the EBSD results for the 15.4P1 and 17.2P1 compositions. These compositions were chosen because they represent the two extremes (minimum and maximum) of tetragonality value. In both cases, the phase maps reveal that *t'*-ZrO_2 is the dominant phase, with fractions of 99.24% and 98.31%, respectively, while only small amounts of *m*-ZrO_2 (0.21–0.96 %) and traces of *o*-Ta_2O_5 (0.04–0.08 %) were detected. These values are very similar to those obtained from XRD analysis, confirming the reliability of the EBSD phase quantification.

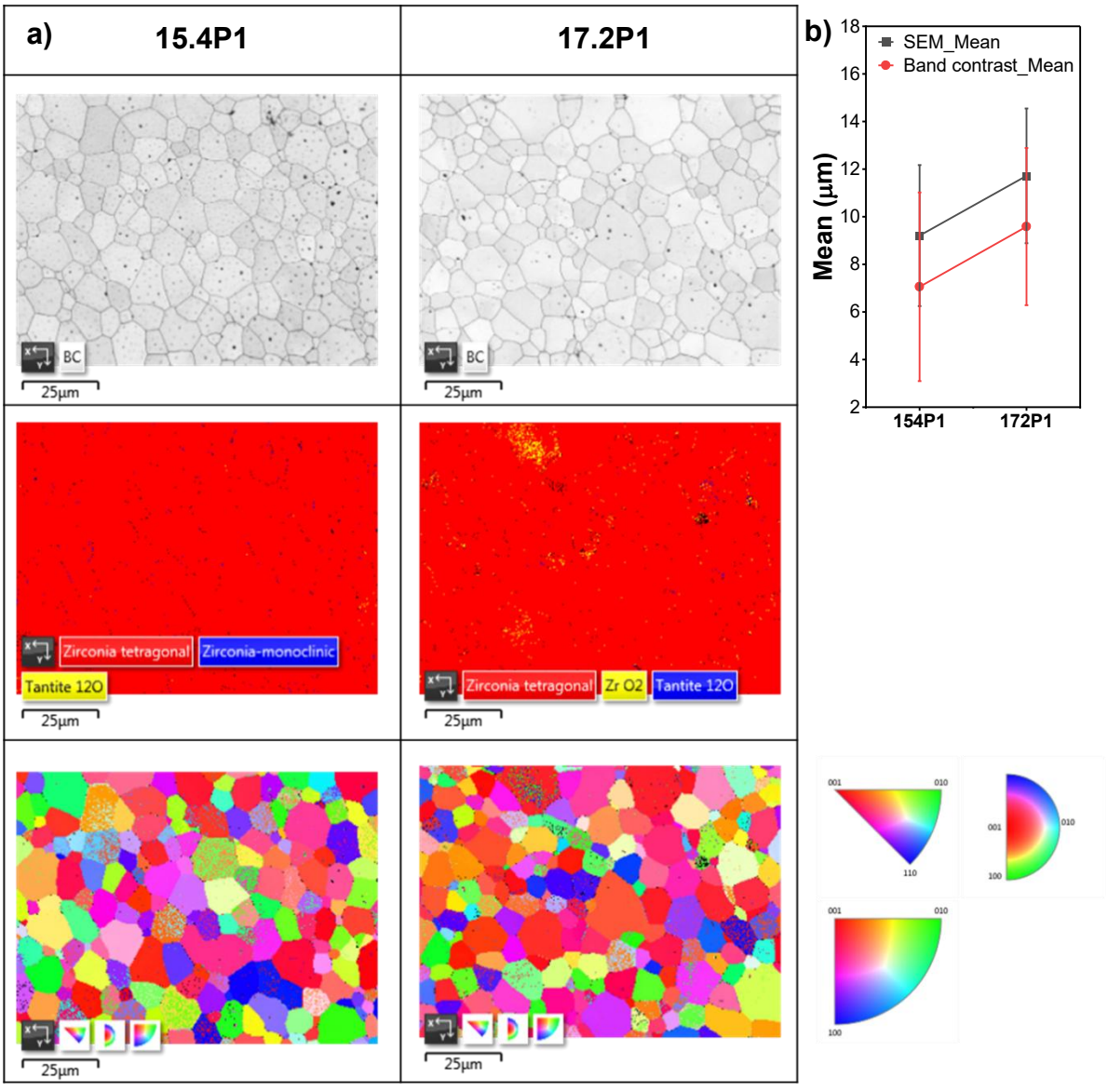


Figure 4.5 a) Phase distribution and crystallographic orientation maps obtained by EBSD for 15.4P1 and 17.2P1 and b) Comparison between grain sizes obtained by SEM and those obtained by EBSD.

The predominance of the *t'*-ZrO_2 highlights the effective stabilization provided by Y and Ta co-doping, which is crucial for improving the mechanical and thermal performance of these ceramics in thermal barrier applications. The inverse pole figure (IPF-Z) maps present a homogeneous color distribution without preferential clustering toward specific crystallographic directions, indicating a nearly random orientation distribution. In addition, and in agreement with the SEM observations, the EBSD images suggest a tendency of Ta dopants and ZrO_2 *m*-phase to segregate at grain boundaries, lowering the boundary energy and facilitating enhanced grain growth during sintering. This is a possible explanation of the progressive increase in grain size observed as the dopant content increases.

Fig. 4.5(b) shows the comparison between the grain sizes obtained by SEM and the values calculated from EBSD. From a statistical point of view, the difference between the two methods is not significant; however, it can be seen that the EBSD values tend to be slightly lower. This tendency can be explained by the different regions analyzed by each technique: SEM images correspond to the surface of the sample immediately after sintering, whereas EBSD was performed on polished cross-sections that reveal the bulk interior. At the surface, atoms are in a higher energy state due to their lower coordination, which increases the driving force for grain growth. As a result, the surface provides a more dynamic environment during sintering, favoring the development of slightly coarser grains compared to the bulk.

AFM images of the polished surfaces of ceramics 15.4P1 and 17.2P1 are shown in Figure 4.6(a-b), along with the roughness parameters obtained from the scans. For 15.4P1, the mean square roughness - RMS (Rq) was 11.9 ± 6.4 nm, while for composition 17.2P1, a slightly higher value of 17.4 ± 6.7 nm was obtained. These values are below the maximum limit of 50 nm recommended in the Hysitron TriboIndenter 950 equipment manual [125] to ensure the reliability of nanoindentation measurements. This confirms that the polishing process used in section 2.1.2 was effective, that the surfaces in this study are smooth enough to avoid significant topographical irregularities, and that the hardness and elastic modulus results reflect the intrinsic response of the material.

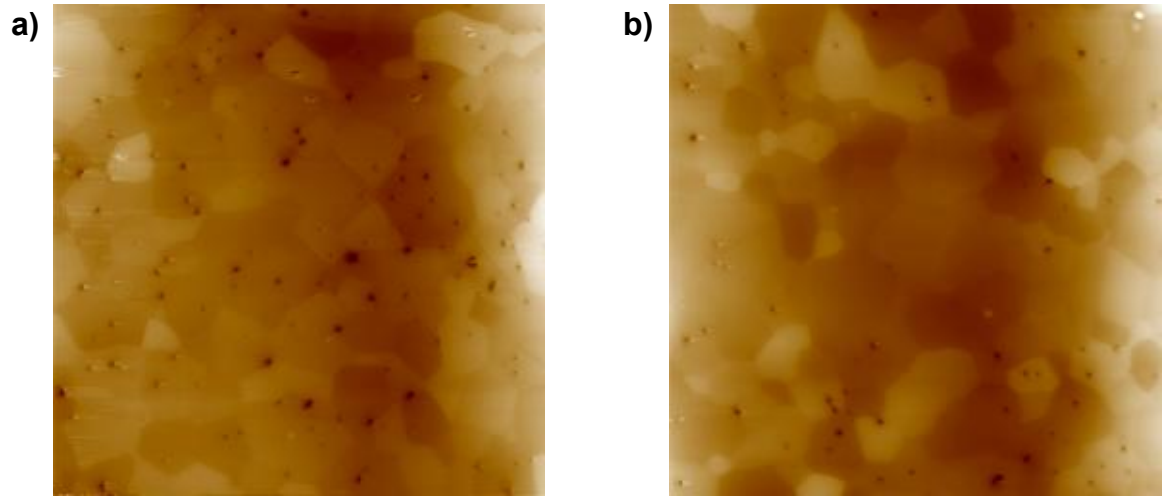


Figure 4.6 AFM images of the polished surface of a) 15.4P1 and b) 17.2P1 dense ceramics showing the microstructure through the topography reconstruction of mechanochemically polished surfaces.

In addition to all these analyses, a microstructural comparison was made of dense 16YTZ ceramics made with powders ground by planetary ball milling and high-energy ball milling processes. Figure 4.7 shows the results of the structural characterization of the ceramics prepared under different conditions. XRD patterns of 16P1, 16P2, and 16P20 ceramic samples are presented in Fig. 4.7(a). All the XRD patterns show the main peak at 2θ = 30.1° and peaks with lower intensity at 2θ = 34.4°, 35.1°, 49.9°, 50.5°, 58.9°, and 59.9°, corresponding to the tetragonal crystalline system of ZrO_2 with space group (P 42/n m c) attributed to the non-transformable tetragonal phase (*t'*) [3]. In addition, low intensity peaks are observed at 2θ = 27.1° and 30.8°, which correspond to the monoclinic phase of ZrO_2 (m-ZrO_2) with space group (P 1 21/c 1), while the peak at 28.8° can be assigned to the orthorhombic phase of Ta_2O_5 (o-Ta_2O_5, P m m 2) [3].

The tetragonality of the material was determined from XRD peaks occurring in the range of 2θ = 71–75° (Fig. 4.7(b)) particularly at angles of 2θ = 71.9° and 74.2°, at which two peaks corresponding to the t′ phase are present [118], where d_c (≈1.30 Å) denotes the interplanar distance of the (004) plane, representing the c axis of the tetragonal crystal, while d_a (≈1.28 Å) indicates the interplanar distance of the (220) plane, representing the a axis [3]. The tetragonality value is important in this system as it has been correlated with the fracture toughness of the material, which tends to increase with higher tetragonality values [45], [64], [119].

The mechanism reported to be responsible for the increase in fracture toughness, which is maintained at high temperatures, is ferroelasticity [3], [120].

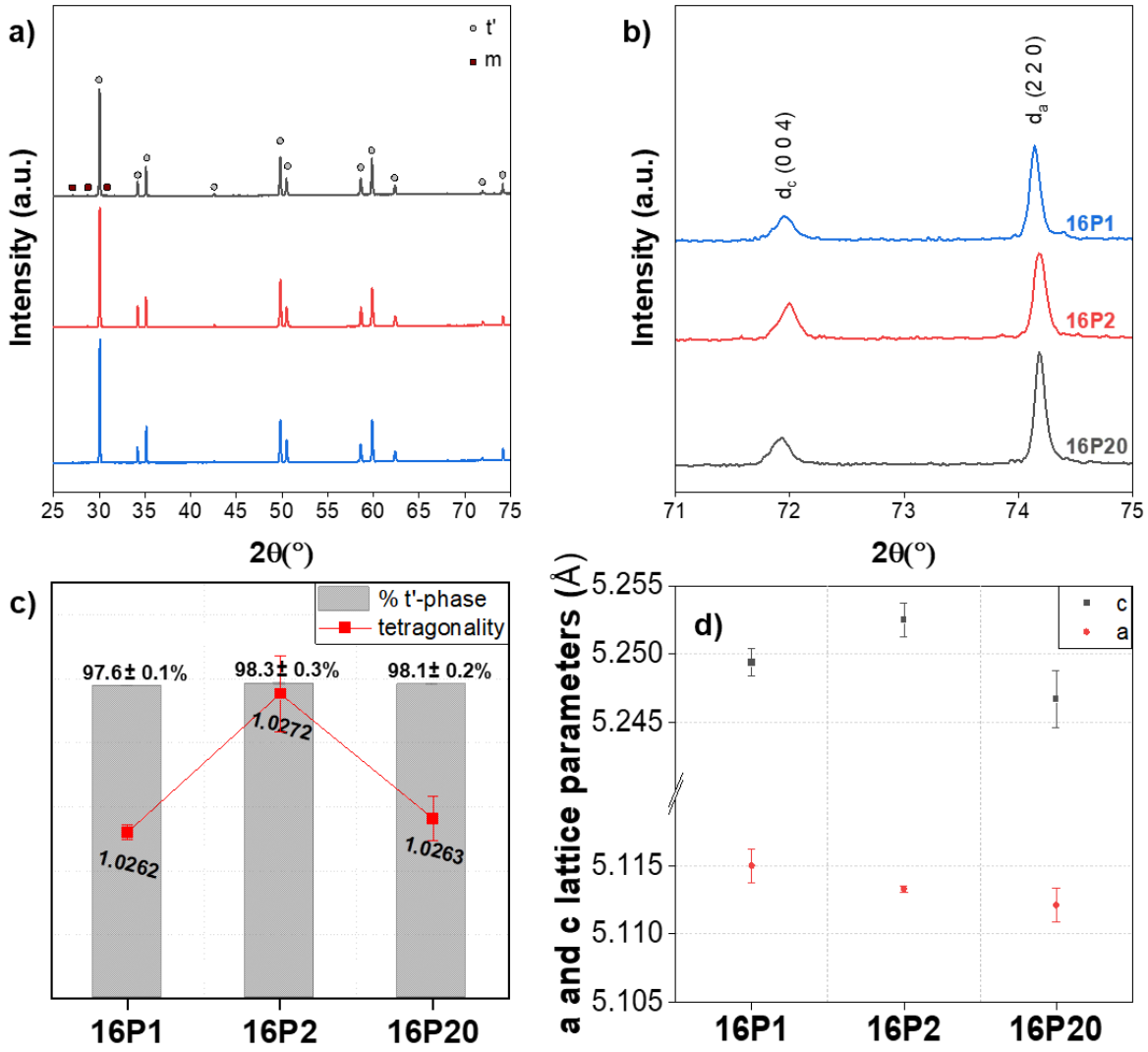


Figure 4.7 XRD patterns of (a) 16P1, 16P2, and 16P20 dense samples. Moreover, (b) highlights the characteristic peaks corresponding to *t'*-phase, (c) tetragonality and % *t'*-phase, and (d) lattice parameters of *t'*-phase in 16P1, 16P2, and 16P20.

The results of the *t'*-phase content and the tetragonality associated with the different processing conditions are presented in Fig. 4.7(c), where it is observed that the percentage of non-transformable tetragonal phase synthesized by the two milling processes is close to 98-99 wt.% [3]. This value was determined by Rietveld refinement of the diffraction pattern, considering the presence of the *t'*- and *m*- phase of ZrO_2 and *o*-Ta_2O_5. A maximum amount of 1.7 wt.% of the *m*-ZrO_2 phase and 0.3 wt.% of *o*-Ta_2O_5 was found in the 16P1 sample obtained by planetary ball milling, while the 16P20 sample showed these values at only 0.8 wt.% and 0.1

wt.% for *m*-ZrO_2 and *o*-Ta_2O_5, respectively [3]. (see Fig. S1 and S2 in the supporting information). Furthermore, 16P1, 16P2, and 16P20 sintered samples present tetragonality values of 1.0262, 1.0272, and 1.0263, respectively, which are higher than those reported for the YSZ system, typically around 1.013, as documented in the literature [45] and are similar with the one reported for the 16YTZ system which is around 1.026 [3], [121]. It can also be seen in Fig. 4.7(d) that the lattice parameters have an almost imperceptible alteration with the change of milling method and sintering time. The error for the values of tetragonality is less than ± 0.00025%; and for the percentage of *t'*-phase less than ± 0.2%. The major influence of the comparison of different powder processing routes is expected on the microstructural characteristics of densified ceramics [3].

Figure 4.8 shows the results of microstructural characterization from SEM micrographs recorded at a magnification of 1000x of 16YTZ ceramics after densification by sintering. These micrographs were mainly analyzed for grain size, following the procedure described in ASTM standard E1382. The results from each processing route showed a microstructure composed by equiaxed grains with an average size of 9.4 ± 2.4 μm for 16P1, 8.4 ± 2.8 μm for 16P2, and 14.0 ± 5.4 μm for 16P20 [3]. Although the initial size of the powders that were pressed and sintered was smaller (see Table 2.1), the increase in grain size between 16P1 and 16P20 at the same sintering time can be attributed to the milling process due to the application of higher impact forces, higher energy density, higher collision frequency, and other favorable conditions in high-energy ball milling [3]. The size of the balls used for milling with Emax was smaller (1 mm) than those used in conventional planetary ball milling (10 mm), and by using smaller balls, there are a greater number of contact points between the balls and the material particles being milled, resulting in a smaller particle size. It has been reported in the literature that the use of smaller diameter balls in high-energy ball milling increases fragmentation efficiency, resulting in high surface activation [117] that favors grain growth during sintering [3].

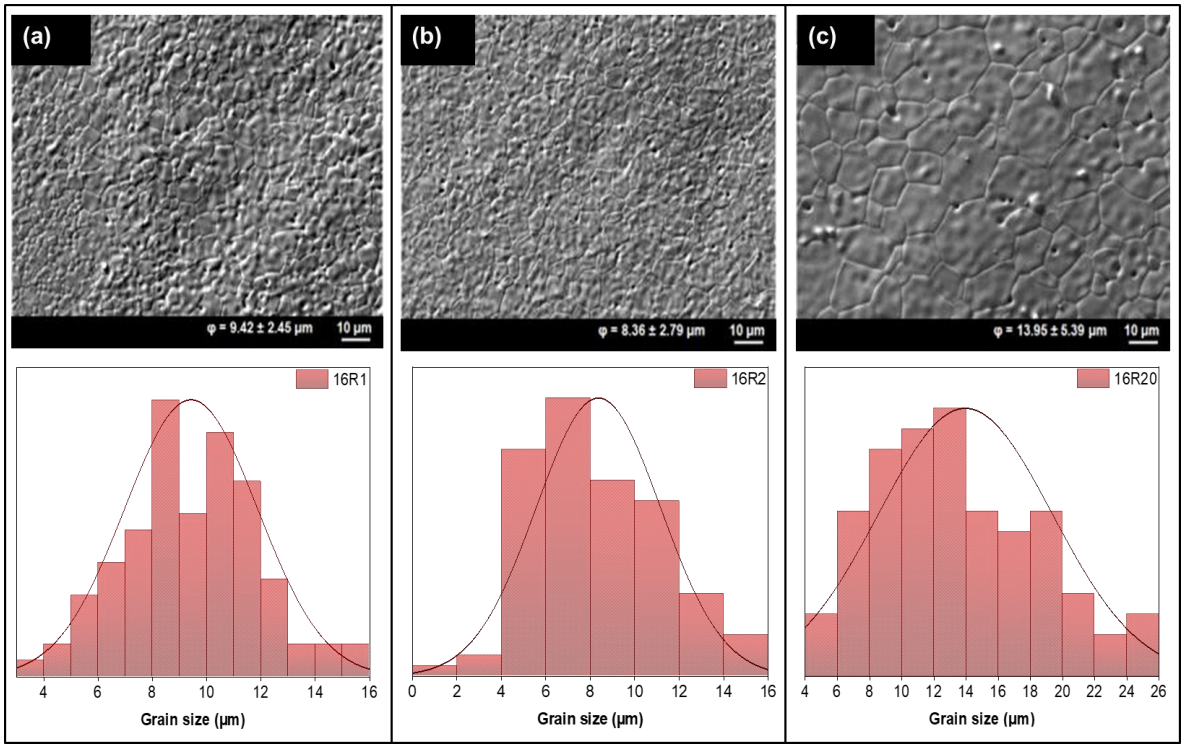


Figure 4.8 Microstructure of samples (a) 16P1, (b) 16P2, and (c) 16P20 with their respective grain size distribution and standard deviation.

The difference in grain size between samples 16P20 (14.0 ± 5.4 µm) and 16P2 (8.4 ± 2.8 µm) is directly related to the sintering time (10 times shorter for 16P2). The higher surface activation produced by the high-energy ball milling process correlates with the transformation to the t′ phase in a shorter time than that required for ceramics that were milled by conventional planetary ball milling [3]. On the other hand, the prolonged exposure time to high temperatures during sintering allows for reorganization of the ceramic particles and further solid-state diffusion processes, which promote grain size growth, as can be seen in Fig. 3(c). Finally, minimal or no porosity is observed in the microstructure revealed by SEM [3].

Typical Raman spectra are shown in Fig. 4.9, where the characteristic vibrational modes of the phases present in the 16YTZ samples processed by the different routes can be identified. In general terms, most of the peaks are associated with the *t'*-ZrO_2 phase and are listed in Table 4.2 along with their corresponding vibrational modes [3]. The Raman signatures of each sample between 150 and 900 cm^{-1} show four characteristic bands at ~ 320, ~ 465, ~ 665, and ~ 805 cm^{-1}, which are consistent with previous reports in the literature associated with the *t'*-ZrO_2

phase [124]. From these Raman spectra, it was not possible to identify all active Raman vibrational modes of the *m*-ZrO_2 phase [3].

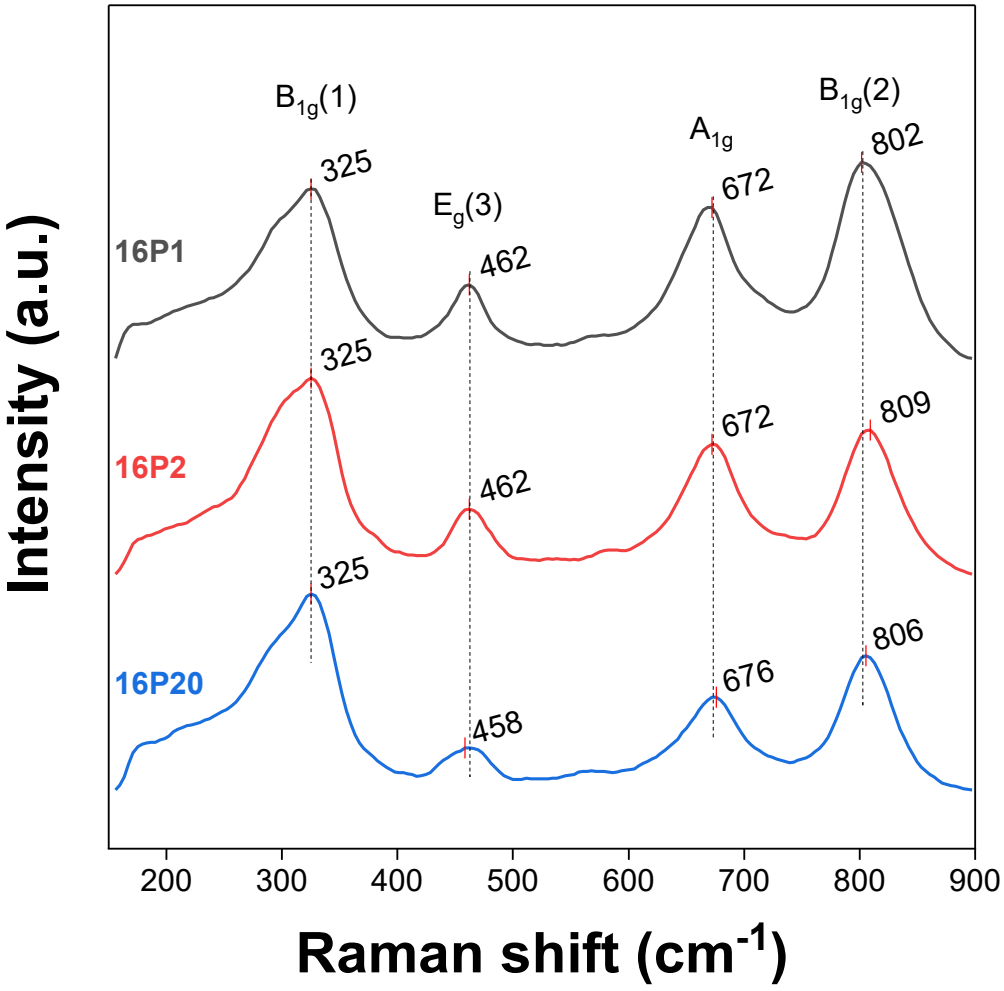


Figure 4.9 Raman spectra of 16P1, 16P2, and 16P20 recorded at room temperature after sintering at 1500 °C.

Table 4.2 Characteristic tetragonal peaks in the Raman spectra of 16P1, 16P2, 16P20 ceramics and their vibrational modes. [3]

	$B_{1g}(1)$	$E_g(3)$	A_{1g}	$B_{1g}(2)$
16P1	325	462	672	802
16P2	325	462	672	809
16P20	325	456	676	806
YTZ [121]	316	458	666	802

4.1.2. Mechanical properties of YTZ system

This microstructural characterization establishes the basis for understanding how these characteristics are reflected in the local mechanical response of ceramics. In this sense, indentation techniques are particularly useful, as they provide information on hardness, elastic modulus, and fracture toughness, properties that are strongly influenced by phase stability, grain size, and dopant distribution. While Vickers microindentation was used to estimate hardness and toughness to compare the results with those reported in the literature, instrumented nanoindentation was applied to representative compositions to record load-displacement curves, identify elasto-plastic deformation events such as pop-ins, and measure crack lengths using AFM images. These results allow a direct correlation to be established between microstructure and mechanical performance at different scales.

To preliminarily evaluate the toughness of the ceramics, Vickers microindentation tests were performed on the five compositions. This technique was selected due to its use in the literature to estimate toughness in ceramic materials. Based on the diagonals of the indentations and the lengths of the radial cracks, the Γ values were calculated using equation 2.3.

Figure 4.10 shows a schematic Vickers indentation illustrating how the diagonal dimensions of the indents and the radial crack lengths were measured for toughness calculation. One of the indentations made in dense ceramics is shown in Figure 4.10(c) as a reference, and the numerical results are shown in Figure 4.11. These are used for comparison with the reported values and those obtained by nanoindentation.

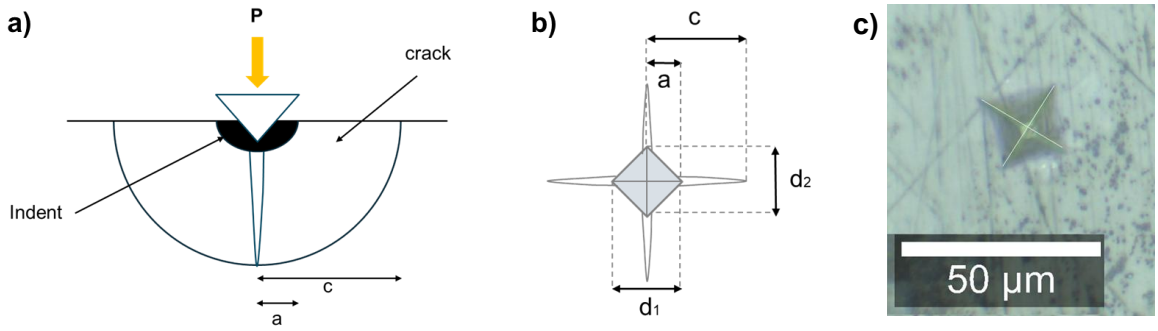


Figure 4.10 Schematic representation of the Vickers indentation method showing (a) the indentation principle with radial cracks, (b) the top view of the imprint with diagonals and crack lengths used for toughness calculations, and (c) indentation made in one of the samples with the characteristic diagonals of Vicker's method, as a reference.

The hardness and toughness results obtained by Vickers microindentation are shown in Figure 4.11(a-b). The hardness values remain in a range between 7.9 and 8.7 GPa, while the toughness values vary between ~43 and 50 J/m^2. Although slight variations are observed between compositions, these differences are not statistically significant with the increase in dopant content.

This indicates that, within the non-transformable tetragonal range of compositions, the mechanical response of the ceramics remains essentially invariant, suggesting that the microstructural modifications induced by doping with Y_2O_3 and Ta_2O_5 do not significantly affect hardness or toughness at the scale evaluated. However, it should be noted that the toughness values achieved exceed the value reported for the 7-8YSZ system, which is around 39 J/m^2 [64] (showed with the dotted line in figure 4.11(b)). It should be noted that the measurements were made by applying loads of 0.3 and 0.5 kgf; in the case of hardness, both loads showed consistent results and the values presented are the result of the average between the two loads, while for toughness, the values obtained at 0.5 kgf are considered, since at this load the cracks developed more clearly and provided more reliable data for analysis than 0.3 kgf.

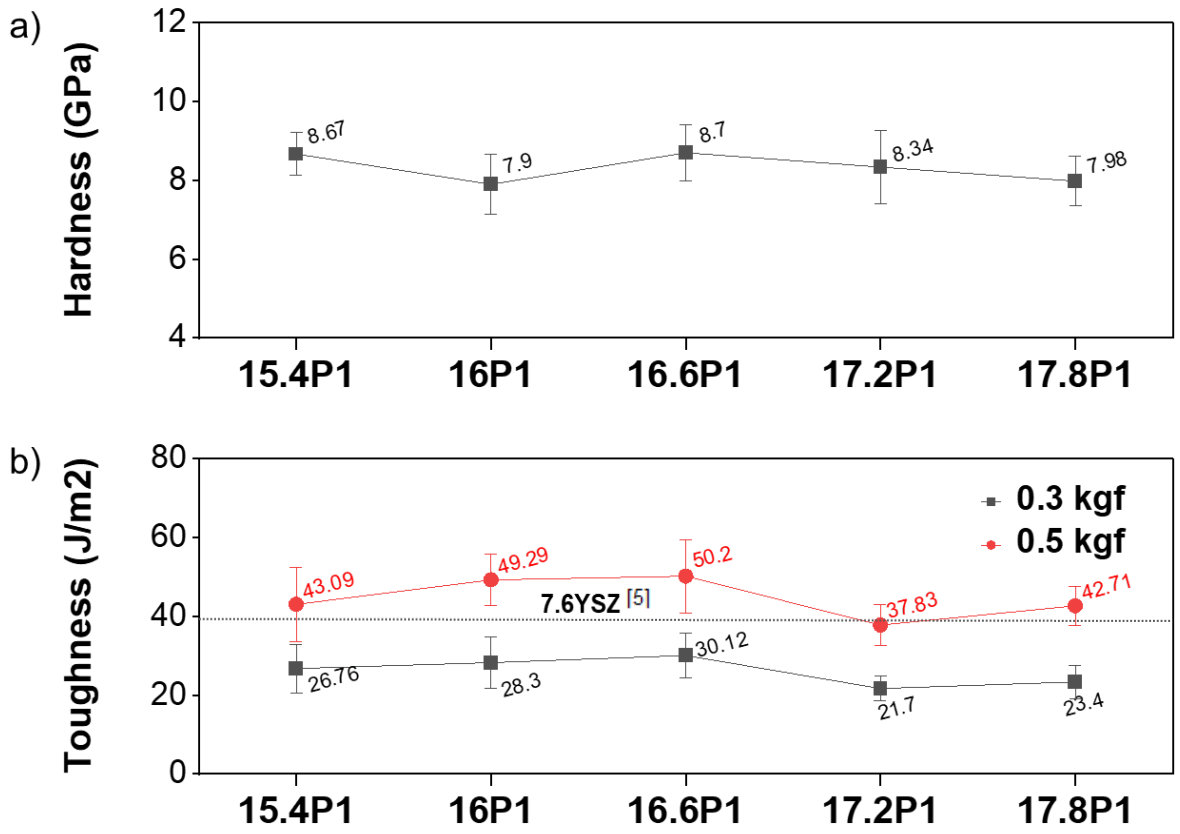


Figure 4.11 Mechanical properties of sintered YTZ ceramics obtained by Vickers microindentation. (a) Hardness as a function of the molar fraction of $YO_{1.5}$ and $TaO_{2.5}$, (b) toughness as a function of load and molar fraction of $YO_{1.5}$ and $TaO_{2.5}$.

Figure 4.12 shows the AFM maps of the indentations made together with three-dimensional reconstructions of the surface in compositions (a) 15.4P1 and (b) 17.2P1. An individual indentation also is showed. In both cases, only indentations from number 1 to number 6 were considered in the analysis, since from the seventh onwards the surface topography did not allow the geometry of the indentation to be clearly identified.

The 3D surface shows a granular topography in which some grains appear higher than others (the higher grains being shown in a lighter tone and the lower grains appearing darker); this contrast can be attributed to the crystallographic orientation of each grain, since during polishing the planes with greater atomic density offer more resistance to abrasion and remain as high areas, while the less compact planes wear down more and form valleys. For instance, in tetragonal PZT ceramics, it was reported that grains oriented in the {001} direction exhibit a faster etching rate, leading to measurable height differences of up to 50 nm after polishing, which correlate directly with domain orientation and surface crystallography [126].

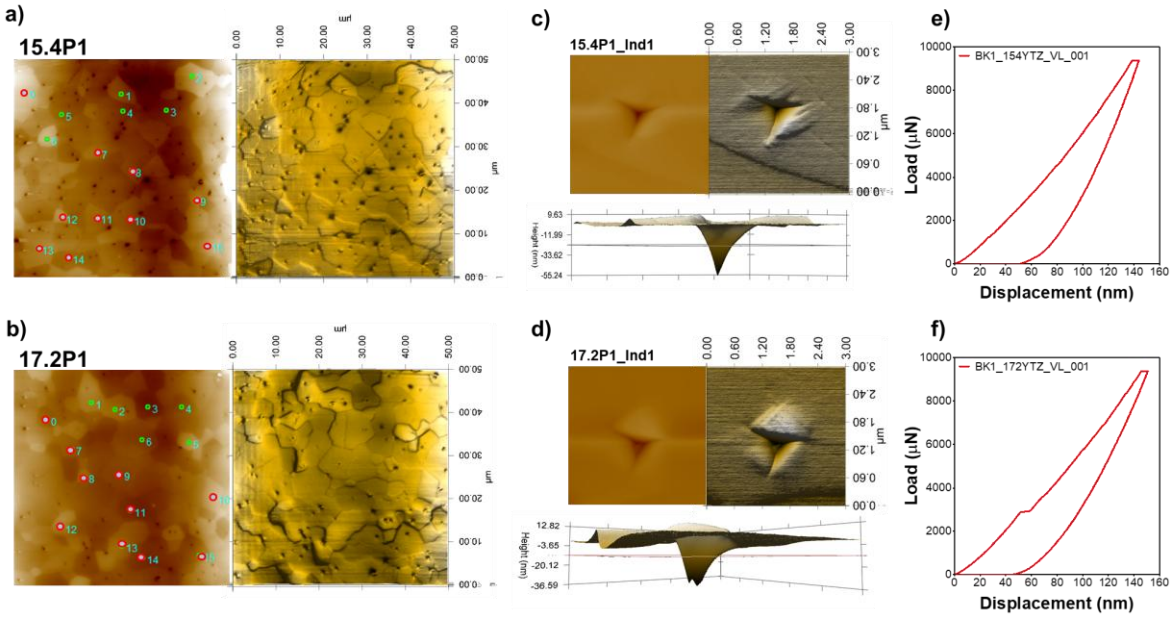


Figure 4.12 AFM map of the indents in the (a) 15.4P1 and (b) 17.2P1 compositions with the respective 3D reconstruction; (c–d) AFM images of indentation number 1 for the 15.4P1 and 17.2P1 compositions: indent topography and 3D reconstruction with residual depth; (e–f) corresponding load–displacement curves obtained under a load of 9.3 mN.

Figures 4.12(c–d) show indentation mark 1 obtained for each composition under a load of 9.3 mN, together with its three-dimensional reconstruction and the residual penetration depth (hf) after unloading. These images display the geometry of the indent and the displacement of material toward the edges, which indicate the presence of plastic deformation and suggest the involvement of the ferroelastic effect in these ceramics, reflected in geometrical features such as the directional lines present in the pile-ups located at the edges of each indentation imprint. At this stage, there is not enough information to provide a

deeper analysis of this phenomenon. An alternative approach could be the use of focused ion beam (FIB) to prepare samples for TEM analysis associated with plastic deformation mechanisms, which can clearly distinguish dislocations from ferroelastic events. However, this topic remains open for discussion in future work.

The 3D reconstruction of the indentation allows us to observe the residual depth remaining after removing the load, information that is complemented by the load-displacement curves shown in figure 4.12(e-f). These curves show the typical response of ceramics under nanoindentation: an initial stage of elastic deformation, progressive penetration under load, and partial recovery during unloading, which defines the residual depth associated with the indentation observed in AFM. In addition, pop-in events are observed, characterized by sudden increases in displacement under constant load, which are associated with crack growth processes or ferroelastic domain switching, characteristic of the mechanical behavior of ceramics under indentation.

Figures 4.13(a-b) and 4.14(a-b) show the sequence of nanoindentations 1 to 6 performed on compositions 15.4P1 and 17.2P1, respectively, under increasing loads ranging from approximately 6 to 9 μN (specific loads are remarked in the figures). The surface morphology and local mechanical response can be analyzed through these series as the applied stress increases.

At low loads, both compositions show indentations with well-defined triangular geometry and low-height pile-ups with relatively uniform distribution around the edges of the indentation, suggesting that the response is dominated by elastic recovery, with only a minor contribution from plastic deformation. As the load increases, the indentations become deeper and the pile-ups become taller and more asymmetrical, evidencing a more pronounced displacement of material and the possible activation of additional deformation mechanisms. At higher loads (8–9 μN), directional formations are observed in sample 15.4P1 in the pile-ups, visible as aligned crests extending from the edges of the imprints. These features are indicative of the onset of ferroelastic switching of tetragonal domains, a mechanism by which domains reorient under shear and compressive stresses, generating local anisotropies in deformation. In sample 17.2P1, this effect is less evident,

suggesting greater tetragonal stability and a lower tendency for domain reorientation under similar loading conditions [9], [59], [64].

A particular behavior is observed in indentation number 6 of sample 15.4P1, where an exceptionally high pile-up appears in comparison with the rest. This response may be due to two factors: either the indentation was generated near a grain boundary, or the grain is favorably oriented to the shear stress, causing an asymmetric redistribution of stresses and localized material deformation in a preferred direction, with no evidence of significant ferroelastic involvement. Taken together, the AFM images, three-dimensional reconstructions, and height profiles reveal the heterogeneous nature of the mechanical response in both compositions, where elastic, plastic, and ferroelastic contributions coexist in varying proportions depending on the applied load and local microstructure.

Figure 4.15(a-b) shows the load–displacement (P–h) curves obtained by nanoindentation in different regions of compositions 15.4P1 and 17.2P1. Each curve represents the local response of an individual indentation point, highlighting variations in stiffness and penetration depth between areas of the same material. These differences are associated with the microstructural heterogeneity characteristic of polycrystalline ceramics, where the crystallographic orientation of the grains, the proximity to grain boundaries, and the presence of local defects govern the stress field under the indenter tip.

In both compositions, the curves display the characteristic features of the nanoindentation process, including an initial elastic region followed by a nonlinear regime typically associated with plastic deformation. Superimposed upon these general trends, several of the curves exhibit distinct discontinuities or “pop-in” events, which are abrupt increases in displacement at nearly constant load. These events correspond to sudden transitions in the deformation mechanism, such as the onset of dislocation motion, ferroelastic switching or fracture associated with the formation of radial cracks beneath the indentation imprint. The presence and magnitude of these pop-ins vary between individual tests, reflecting differences in the local microstructural configuration, grain orientation, and defect distribution at each indentation site.

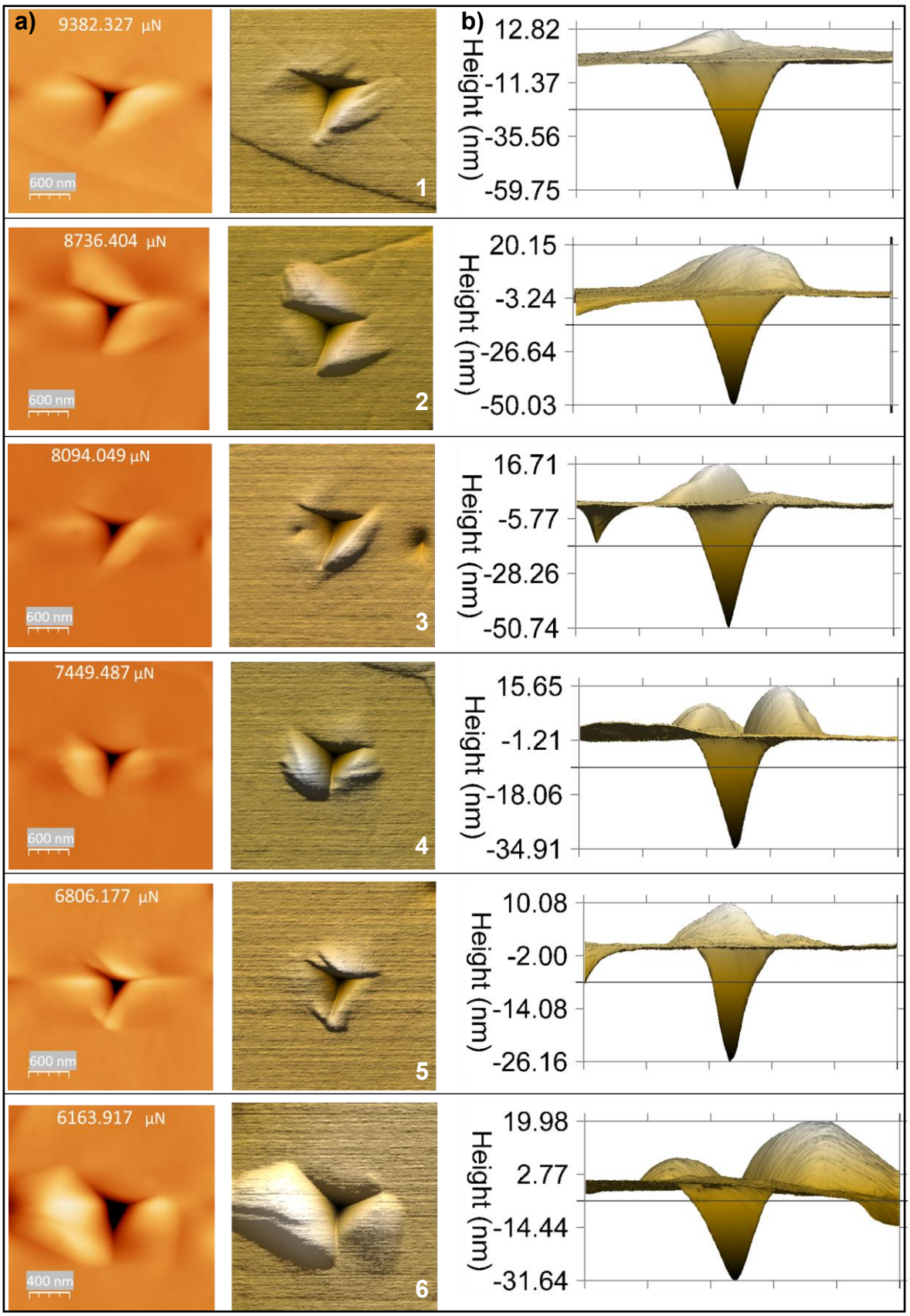


Figure 4.13 AFM of Indentations 1 to 6 performed on the 15.4P1 composition under different applied loads where (a) shows 2D images and 3D reconstructions of each imprint highlighting their geometry and, (b) the corresponding height profiles displaying h_f.

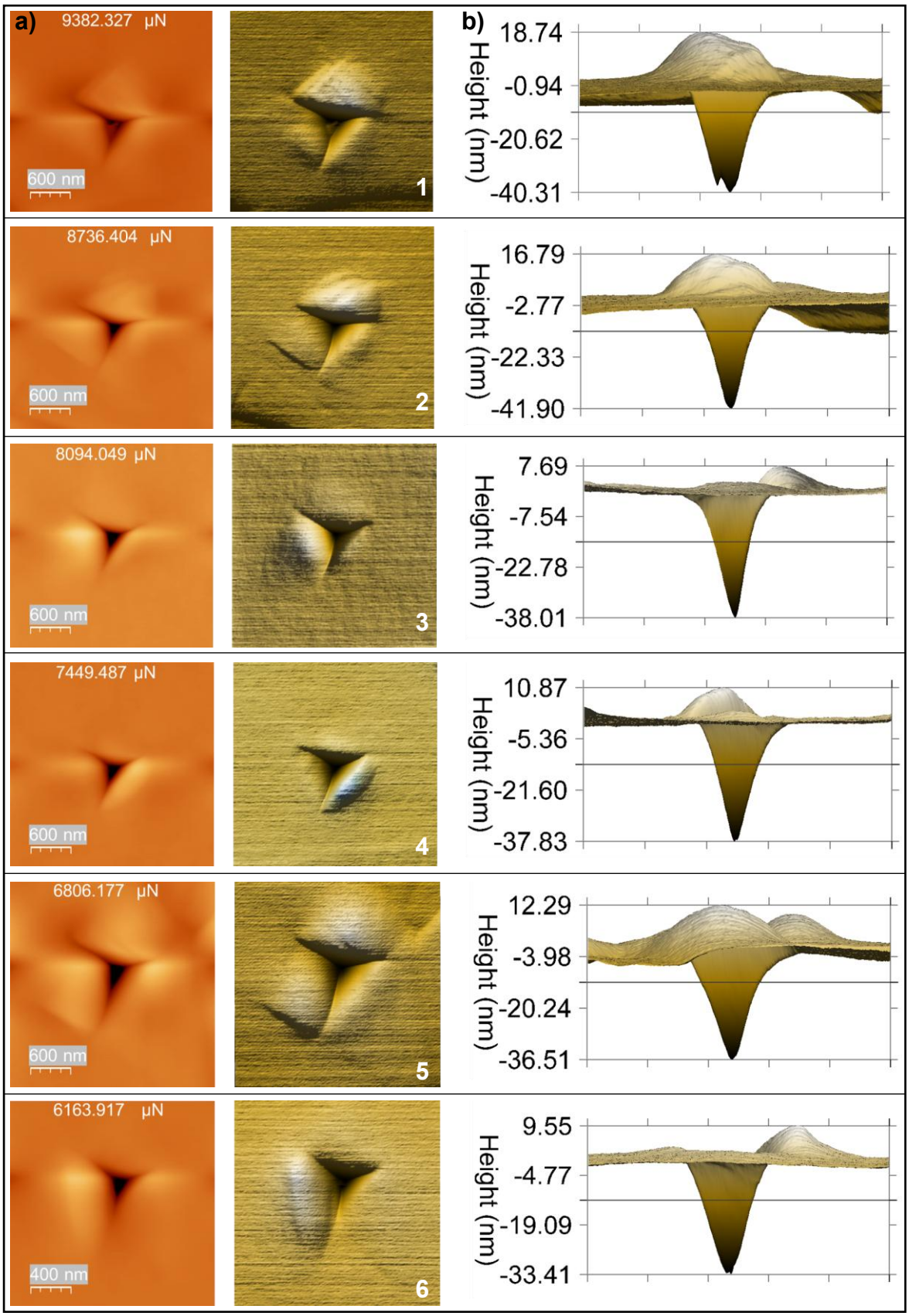


Figure 4.14 AFM of Indentations 1 to 6 performed on the 17.2P1 composition under different applied loads where (a) shows 2D images and 3D reconstructions of each imprint highlighting their geometry and, (b) the corresponding height profiles displaying h_f.

Comparing the two sets of curves, it is evident that the 15.4P1 and 17.2P1 compositions exhibit distinct mechanical responses. The differences in the slope of the loading segment and in the depth of penetration suggest variations in hardness and elastic modulus between both materials.

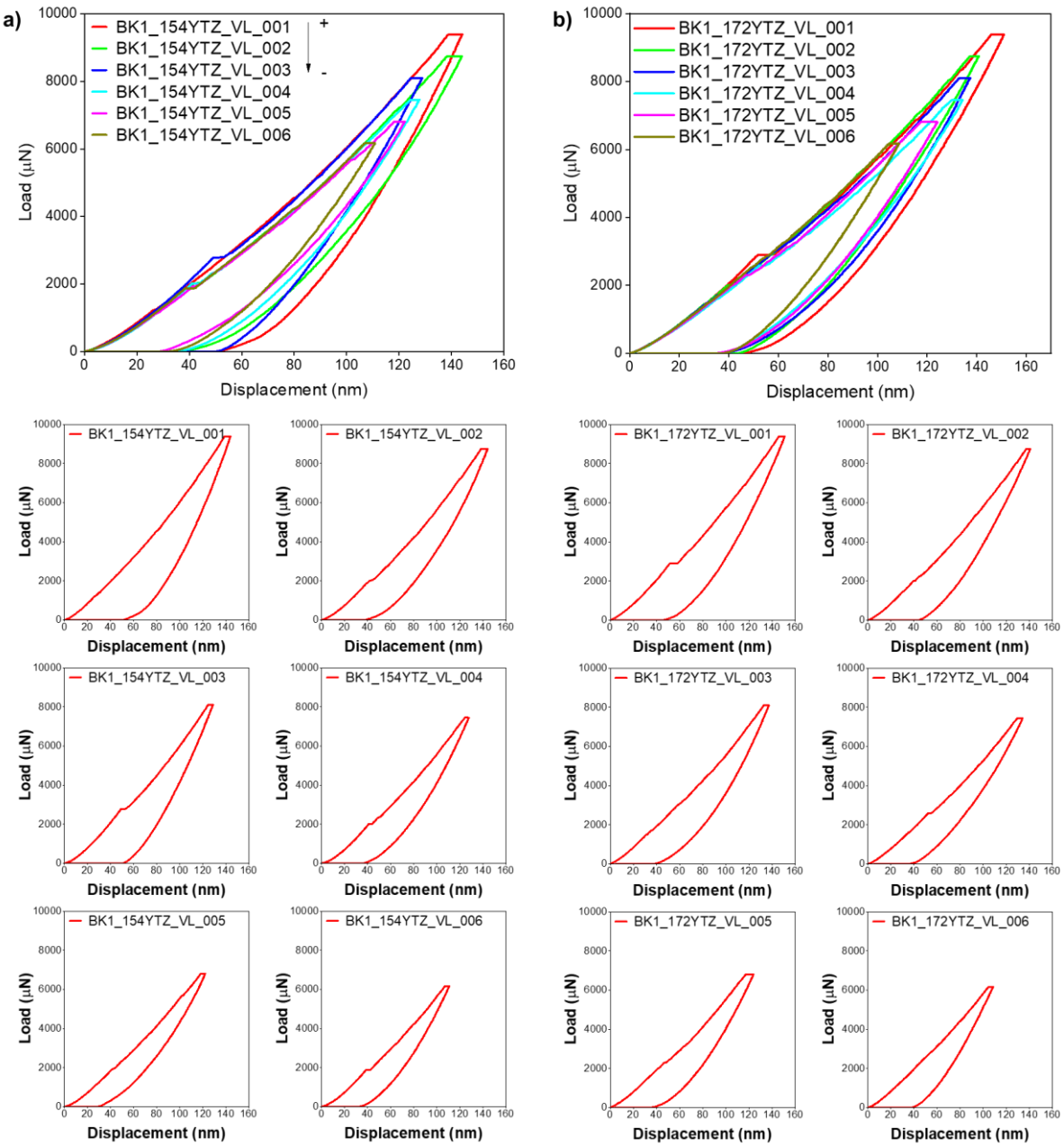


Figure 4.15 Load–displacement (P–h) curves obtained by nanoindentation at different locations on the 15.4P1 and 17.2P1 compositions. Variations in penetration depth and loading slope reflect the influence of local microstructural heterogeneity, whereas the *pop-in* events indicate sudden transitions in the deformation regime associated with the activation of plastic, ferroelastic or fracture mechanisms.

In an effort to explain the differences in behavior between curves with higher or lower maximum penetration or between physical characteristics of the selected samples, associated for example with their tetragonality, the following comments can be made. Curves with lower penetration correspond to tested grains that allow lower plastic deformation, or eventually fewer events of ferroelasticity, or fracture [126]. Regarding the different compositions selected, which present differences in tetragonality, pop-in phenomena are observed, characterized by abrupt increases in displacement under an almost constant load, reflecting local transitions in the deformation regime, linked to the possible emission of dislocations, the activation of ferroelastic switching, or fracture events. Composition 17.2P1 has greater tetragonality, so in the following sections, approximations will be made to elucidate some effects, quantifying not only hardness and elastic modulus values, but also quantifying pop-in events, determining the fracture of both materials, etc.

Figure 4.16 shows a summary of the nanoindentation results for the 15.4P1 and 17.2P1 samples, that depicts the evolution of hardness and reduced modulus of elasticity as a function of the contact penetration depth, as determined by the Oliver and Pharr analysis method [102]. Each data point corresponds to an individual indentation measurement.

Similarly, it can be seen that the reduced elastic modulus remains relatively constant with increasing penetration depth, suggesting that the elastic response of the material is homogeneous at the tested scale. The slight variations observed among data points can be linked to local microstructural heterogeneity, such as grain orientation or residual stress differences.

Comparing the two compositions, 15.4P1 and 17.2P1, the results reveal that both materials possess comparable mechanical responses, although subtle differences in average hardness and modulus values may indicate minor variations in their microstructural constitution or phase distribution. Overall, the figure confirms the reliability of the Oliver and Pharr method [102] in extracting consistent mechanical parameters and highlights the stability of the mechanical behavior of both samples across the explored penetration depth range. However, both compositions and both properties show a dispersion of results, making it

impossible to identify differences associated with differences in tetragonality between the two samples. To identify subtle differences between the two properties and the different compositions, a Weibull statistical analysis was performed, which is presented below.

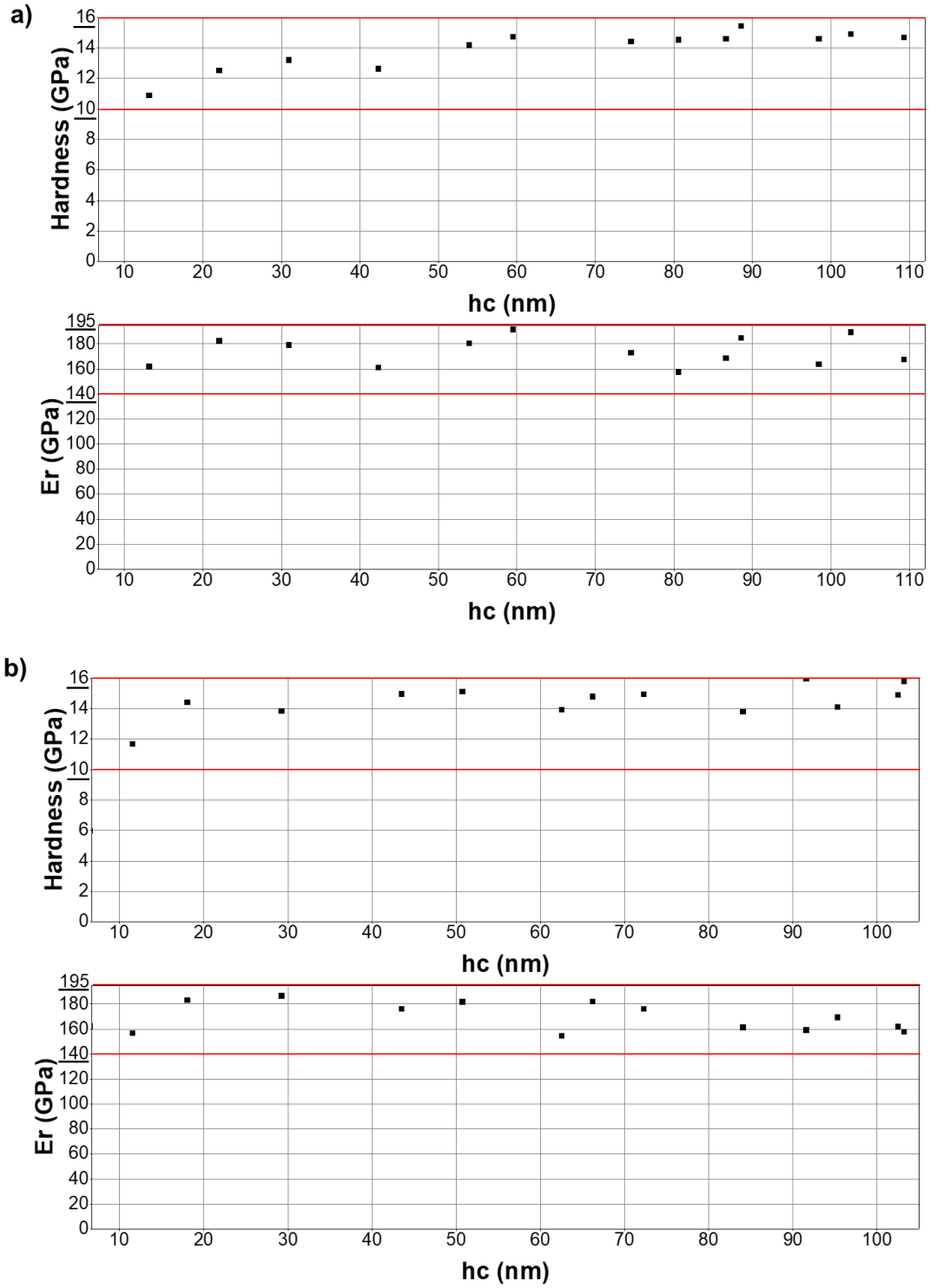


Figure 4.16 Summary of results for hardness and reduced modulus of elasticity as a function of contact penetration depth determined by the Oliver and Pharr method for (a) 15.4P1 and (b) 17.2P1 samples.

Figure 4.17 shows the Weibull statistical analysis of the nanoindentation results for the (a) 15.4P1 and (b) 17.2P1 samples, based on the distributions of hardness and reduced elastic modulus. In both cases, the experimental data exhibit a linear trend when plotted in Weibull coordinates, indicating that the mechanical response of each composition follows a Weibull-type distribution. The red lines correspond to the linear fits of the data, from which the Weibull parameters are extracted. The slope of each linear fit represents the Weibull modulus, which quantifies the degree of scatter in the data, where higher slopes correspond to more homogeneous mechanical behavior, whereas lower slopes indicate greater variability. The intercept at the zero ordinate defines the characteristic Weibull value of the property, corresponding to the most probable hardness or modulus value for the tested material.

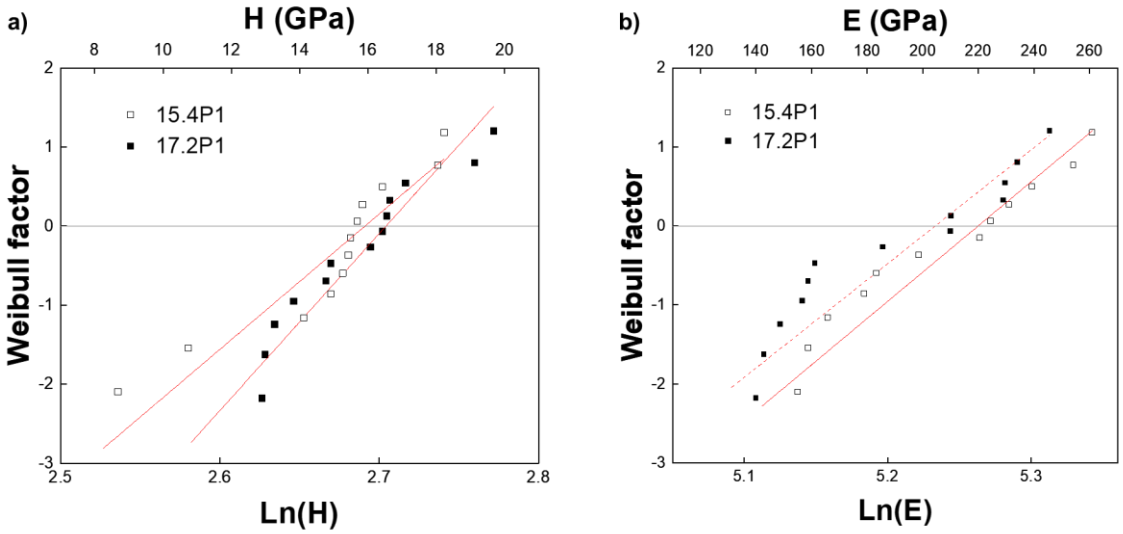


Figure 4.17 Weibull plots of hardness and reduced elastic modulus results for (a) 15.4P1 and (b) 17.2P1 samples.

For the hardness results, the 15.4P1 sample shows a Weibull slope of approximately m_H ≈ 17.13 GPa and a characteristic hardness H_0 ≈ 15.88 GPa, whereas the 17.2P1 composition exhibits m_H ≈ 22.38 and H_0 ≈ 16.50 GPa. Similarly, the reduced elastic modulus data yield slopes of m_E ≈ 15.15 for 15.4P1 and m_E ≈ 14.41 for 17.2P1, with characteristic moduli of E_0 ≈ 205 GPa and E_0 ≈ 220 GPa, respectively. These results are consistent with zirconia-based ceramics showing non-transformable tetragonal structure as it is the case of 7YSZ. These results also highlight the remarkable similarity between both compositions in terms of central values and dispersion, even though the Weibull analysis is particularly

sensitive to subtle variations in mechanical behavior. The nearly overlapping fits confirm that both materials possess a comparable degree of microstructural uniformity and mechanical consistency.

Despite the capability of the Weibull statistics to detect fine differences, the similarity in both the slope and intercept values suggests that the hardness and elastic modulus distributions are nearly identical for 15.4P1 and 17.2P1. Therefore, to further elucidate the origins of the localized deformation phenomena observed during indentation, it becomes necessary to analyze the behavior of the load–displacement curves in the loading regime. This will allow distinguishing whether the observed pop-in events arise from ferroelastic switching, plastic yielding, or fracture processes. The corresponding results are presented in the following figure.

Figure 4.18 presents the load–displacement curves obtained during the loading stage for samples (a) 15.4P1 and (b) 17.2P1, emphasizing the regions corresponding to the onset of the first pop-in events. These curves illustrate the mechanical response of the materials under nanoindentation and allow the quantification of the transition from purely elastic to elastoplastic or fracture-dominated deformation. The analysis focuses on comparing the experimental load–displacement data (blue curves) with the theoretical behavior predicted by the Hertzian contact model (green curves), which describes the purely elastic indentation response of a the Berkovich indenter, modeled in the tip end as a spherical tip. The green Hertzian fits serve as a reference to identify deviations associated with the first pop-in, marking the transition from the elastic regime to the onset of permanent deformation or crack formation.

The difference in penetration depth between the experimental curve and the Hertzian prediction defines a characteristic value denoted as hx, which corresponds to the depth deviation at a given maximum load (Pmax). This parameter quantifies the mechanical discontinuity associated with the initiation of localized damage. The typical h_x values obtained from these analyses lie within the range of a few tens of nanometers, reflecting the sensitivity of the indentation technique to early fracture or plasticity events.

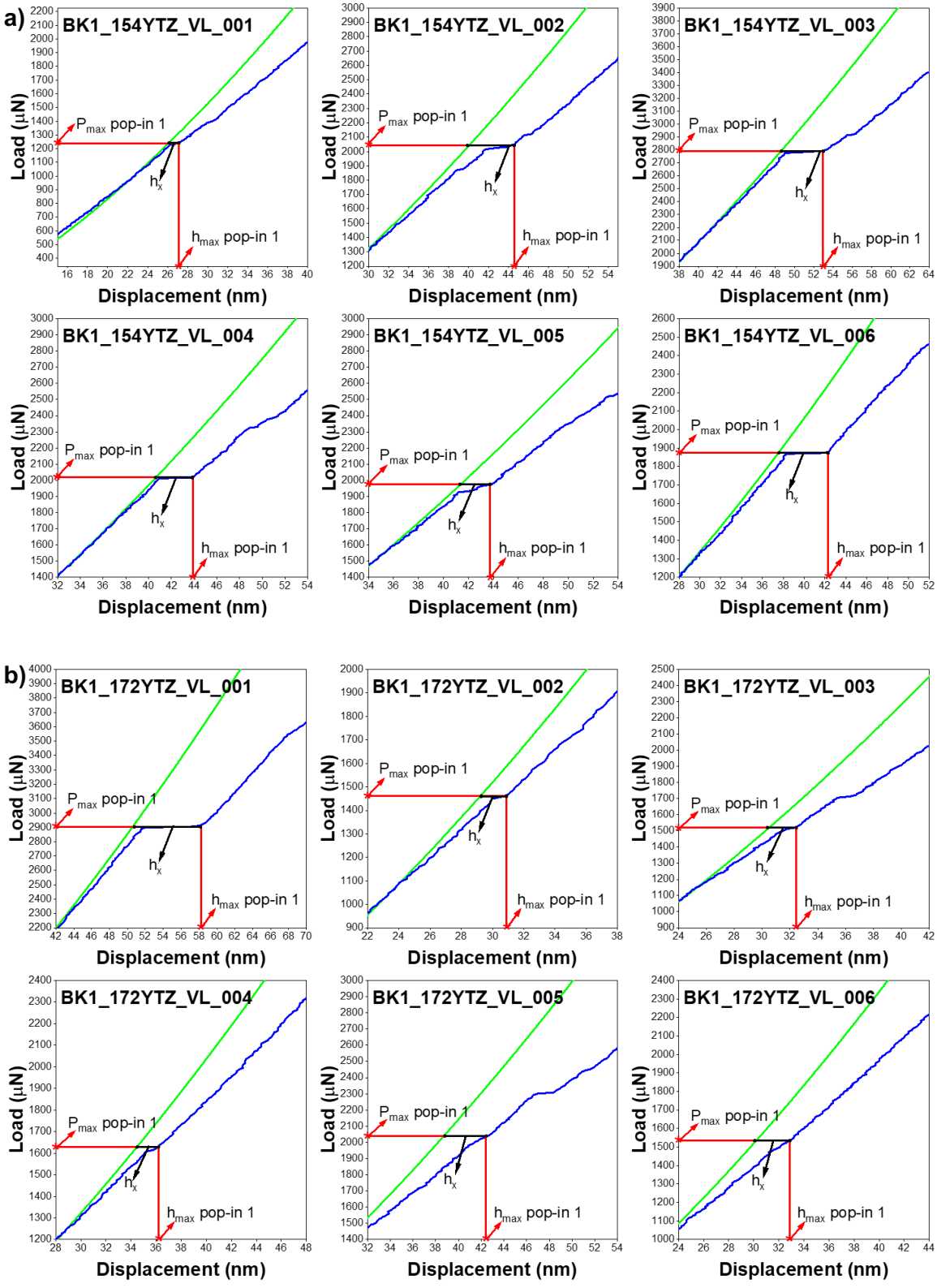


Figure 4.18 Load-displacement curves at the loading stage for (a) 15.4P1 and (b) 17.2P1 samples. Analysis is focused on regions of the appearance of the first pop-in for quantifying the nature of this transition region when compared with a simulated curve using the Hertz equation of a spherical tip.

To analyze the hx values quantified in the previous figure, it is necessary to briefly review the work of Field, Swain, and Dukino published in 2003 [103], in which they describe the quantitative relationship between crack length (c) and additional penetration depth (h_x) generated during the pop-in event in indentation experiments on brittle materials.

Equation 4.2 expresses the differential correlation between the increment in crack length and the corresponding increment in the extra penetration caused by the pop-in phenomenon:

$$\frac{dc}{dh_x} = Q\frac{H_M}{E'} - \sqrt{2} \tag{4.2}$$

Here, Q is an empirical constant proposed by the authors to relate the indentation-induced deformation and fracture parameters, H_M is Meyer's hardness, and E' is the reduced elastic modulus of the material. This expression derives directly from the analytical form of Eq. (8) in the same paper, which connects the total crack length to both the maximum penetration h_m and the additional depth h_x resulting from crack formation. The differential form isolates the term representing the sensitivity of crack extension to the mechanical discontinuity produced by pop-in.

Equation 4.3 provides an alternative experimental route to evaluate the same derivative:

$$\frac{dc}{dh_x} = \frac{dc}{dP^{2/3}} \cdot \frac{dP^{2/3}}{dh_x} \tag{4.3}$$

This reformulation links the variation of crack length and extra penetration to $P^{2/3}$. The choice of the $P^{2/3}$ scaling follows the earlier work of Lawn, Evans, and Marshall [127], who established that the ratio $P/c^{3/2}$ remains constant for a given brittle material under indentation. Hence, Eq. 4.3 enables the determination of the slope $(dc/dP^{2/3})$ from experimental plots of crack length

versus $P^{2/3}$, and of $(dh_x/dP^{2/3})$ from corresponding plots of extra penetration versus $P^{2/3}$. The constant Q can then be extracted by combining these slopes within the framework of Eq. 2.4.

Figure 4.19 shows the experimental correlations obtained for both crack length (c) and extra penetration (hx) as a function of $P^{2/3}$. In both cases, the data exhibit a clear linear behavior, confirming the proportionality predicted by Eqs. (4.2) and (4.3). The slopes extracted from these plots correspond to $(dh_x/dP^{2/3})$ and $(dc/dP^{2/3})$, which can subsequently be used to estimate the empirical constant Q that links indentation load, deformation, and fracture response. The smaller slope obtained for the 15.4P1 composition in the h_x–$P^{2/3}$ data (fig. 4.16(a)) reveal slightly reduced penetration increments for this composition. Similarly, the c–$P^{2/3}$ curve (fig. 4.16(b)) indicates a lower rate of crack extension under increasing load, consistent with a higher apparent fracture resistance supporting the interpretation of a less pronounced crack opening during pop-in events. The Q values obtained for the YTZ ceramics ($Q_{15.4P1} = 1.17$, $Q_{17.2P1} = 0.74$) were close to unity for both compositions. This agreement confirms the internal consistency of the data and indicates that the variations of crack length and extra penetration follow the same mechanical correlation, as expected from the Field–Swain model.

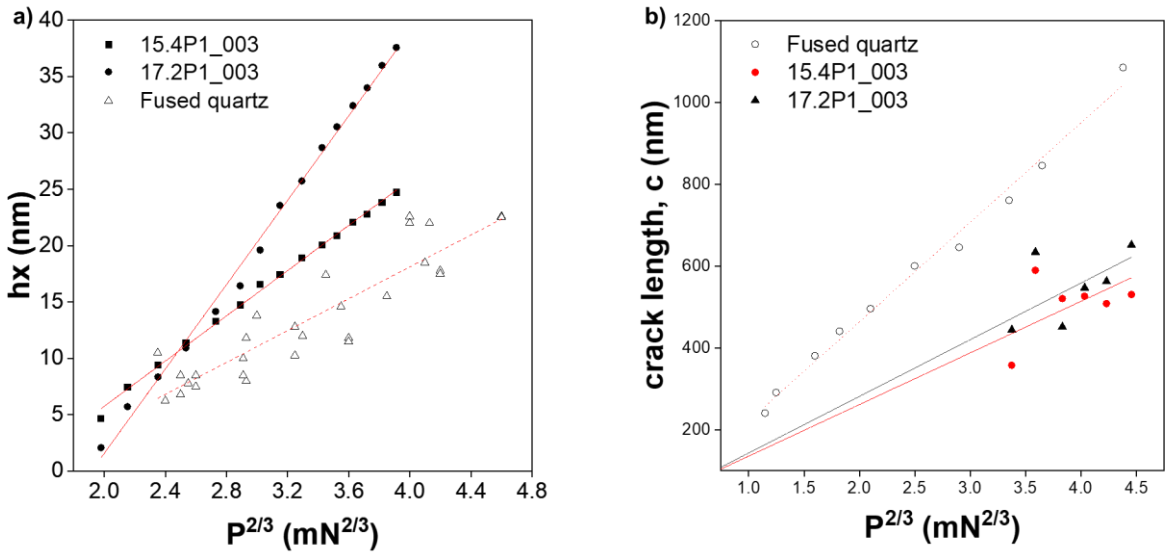


Figure 4.19 Experimental correlations of a) extra penetration (h_x) and b) crack length (c) as a function of $P^{2/3}$ for 15.4P1 and 17.2P1 compositions used to determine the empirical constant Q.

The fracture toughness values calculated by the Eq. 2.2 considering a value of $P = 9.4\,mN$ and $c^{3/2}$ obtained by nanoindentation were $K_{IC,15.4P1} = 2.83$ MPa*m$^{1/2}$and $K_{IC,17.2P1} = 2.48$ MPa*m$^{1/2}$. The higher fracture toughness obtained for the 15.4P1 composition is consistent with its lower slope in the c–$P^{2/3}$ plot and the smaller increments of h_x during pop-in. The internal consistency of the data, confirmed by the Q values close to unity, and the agreement with the Field–Swain correlation, support that the pop-in events in these ceramics are governed by an elastic–brittle fracture mechanism.

4.1.3. Thermal properties of YTZ system

Thermal diffusivity (α), specific heat capacity (C_p), and thermal conductivity (k) are key parameters governing the heat transport capability of ceramic materials. Their combined progress with temperature and composition provides valuable comprehension into the phonon-scattering mechanisms that control the insulation efficiency of Zr-based ceramics for thermal barrier coatings applications. The thermal properties of the YTZ system were evaluated at 25, 100 and 200 °C for the five compositions, as shown in Figure 4.17, and in an extended range from 25 to 1000 °C for the 15.4P1 and 17.2P1 compositions, as shown in Figure 4.18.

As shown in Figure 4.20(a), all compositions exhibited a slight decrease in thermal diffusivity with increasing temperature, which is typical of oxide ceramics and reflects enhanced anharmonic phonon–phonon scattering at elevated temperatures [128]. The 17.8P1 sample consistently showed the highest diffusivity across the measured range, which can be attributed to its higher densification and lower porosity. In contrast, the other compositions grouped closely together within the uncertainty range.

The substitution of Zr^{4+} ions (91.2 g, 0.79 Å) by Y^{3+} (88.9 g, 1.02 Å) and Ta^{5+} (180.95 g, 0.68 Å) introduces mass and strain-field disorder, which disrupts the periodicity of the cation sublattice and shortens the phonon mean free path, so reducing α. Similar effects have been reported for co-doped zirconias within the ZrO_2–$YTaO_4$ quasi-binary system [18], [45], [70]. At higher temperatures(Fig. 4.21(a)), diffusivity tends to stabilize, indicating that the phonon

mean free path approaches its minimum theoretical value, as also observed for Y/Ta co-doped t′-zirconias [59].

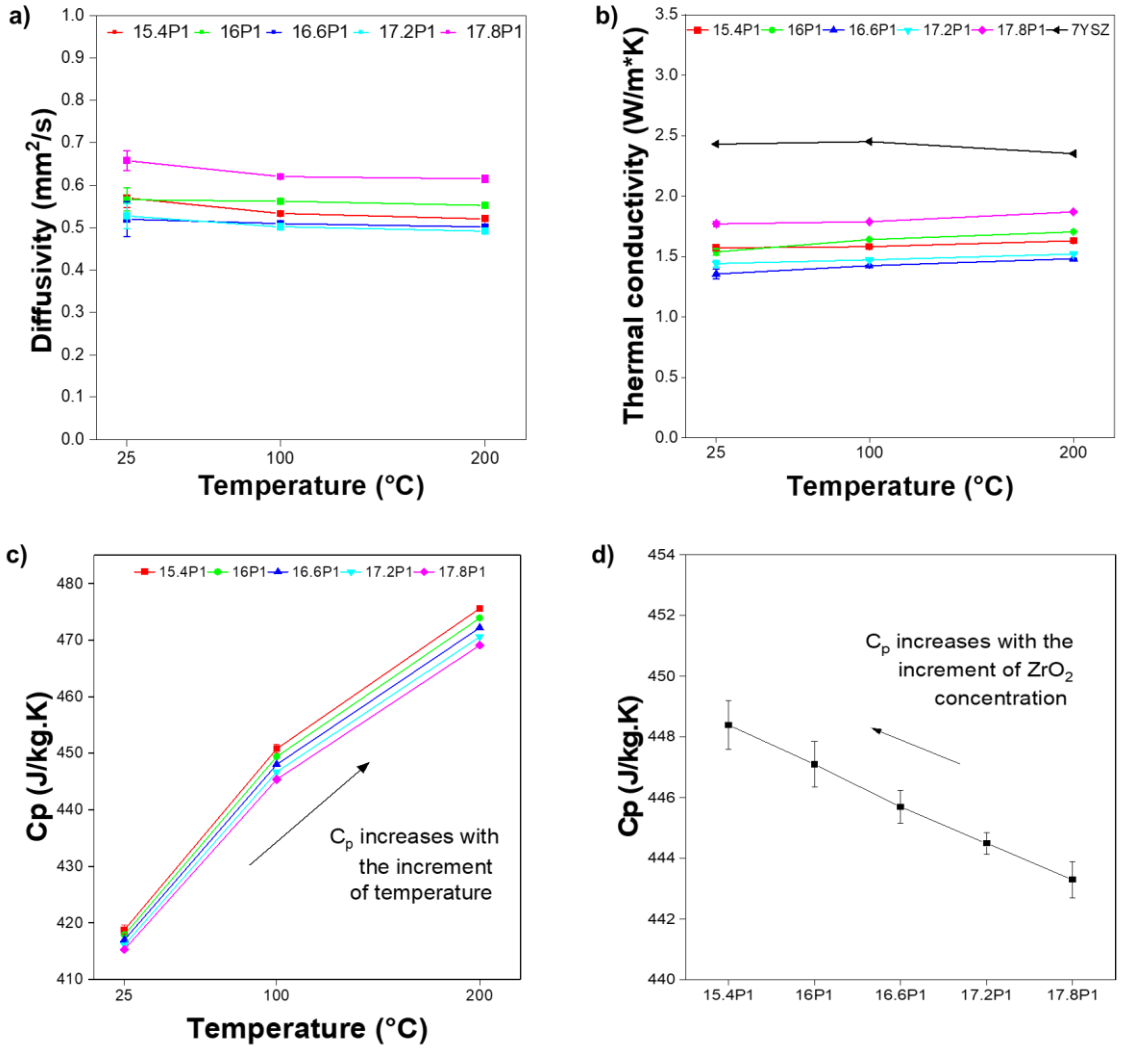


Figure 4.20 Thermal properties of the YTZ system evaluated at 25, 100, and 200 °C for the five compositions: (a) thermal diffusivity; (b) thermal conductivity including 7YSZ as a reference; (c) C_p as a function of temperature; and (d) Cp as a function of ZrO_2 content.

The specific heat values shown in Figures 4.20(c-d) exhibit two clear trends. First, C_p increases with temperature for all compositions, consistent with the progressive excitation of vibrational modes in the lattice according to the Debye model [70]. As temperature rises, additional phonon states become thermally active, and Cp asymptotically approaches the Dulong–Petit limit.

Second, C_p also increases slightly with the ZrO_2 content, as illustrated in Figure 4.20(d). This effect is correlated to the lighter atomic mass of Zr compared with Ta and to the enhanced vibrational degrees of freedom of the zirconia-rich

lattice. As the ZrO_2 fraction increases, the cation sublattice becomes more ordered and less affected by the mass contrast and local lattice distortions introduced by the dopants, enabling a higher capacity for thermal energy storage. At higher temperatures (Fig. 4.21(c)), this trend persists, confirming that the vibrational contribution dominates over electronic or microstructural effects in the studied range. Nevertheless, the increase in C_p does not necessarily imply higher thermal conductivity, as the overall heat transport is mainly governed by the mobility of phonons, which is limited by strong scattering due to mass disorder and lattice strain [8][69].

The thermal conductivities calculated from diffusivity, density and C_p, following the Eq. 2.5 are presented in Figure 4.20(b). All compositions display low and nearly temperature-independent values in the range of 1.3–1.9 $W \cdot m^{-1} \cdot K^{-1}$, well below those of conventional 7YSZ (≈ 2.5 $W \cdot m^{-1} \cdot K^{-1}$). This behavior confirms that the main mechanism governing heat transport is phonon scattering caused by mass and elastic field fluctuations among Zr^{4+}, Y^{3+} and Ta^{5+} cations [18], [70]. The large atomic mass contrast (ΔM ≈ 90 g between Ta and Zr) and the ionic radius mismatch generate localized lattice distortions that effectively scatter phonons and reduce their mean free path.

In the high-temperature range (Fig. 4.21(b)), both 15.4P1 and 17.2P1 maintain conductivities between 1.3 and 1.8 $W \cdot m^{-1} \cdot K^{-1}$, with minimal variation up to 1000 °C. This quasi-invariant behavior reflects the fact that the system operates near the phonon minimum mean free path limit, where additional temperature increases no longer significantly change k. Moreover, since charge neutrality is achieved by the balanced substitution of Y^{3+} and Ta^{5+} for Zr^{4+}, oxygen vacancies are not required; thus, the low thermal conductivity arises from mass fluctuation scattering rather than from vacancy scattering, as occurs in 7YSZ [18].

The values obtained here are consistent with those reported for the 16Y–16Ta (16YTZ) composition, which also exhibits conductivities below 2 $W \cdot m^{-1} \cdot K^{-1}$ over a wide temperature range [70]. This agreement reinforces the reproducibility of the mass–strain scattering mechanism and the stability of the t′-phase as an efficient thermal insulator.

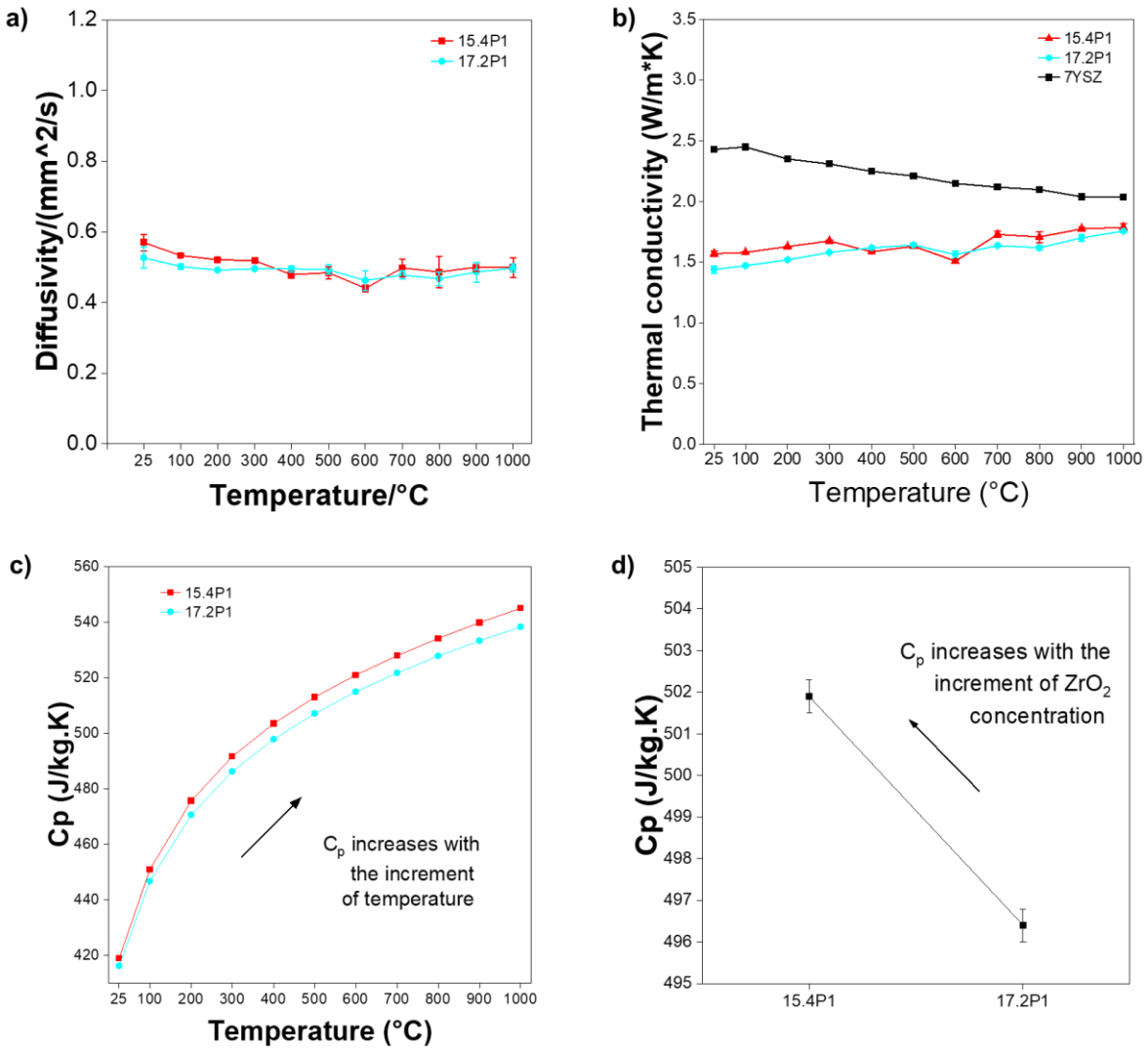


Figure 4.21 Thermal properties of the YTZ system are evaluated from 25 to 1000 °C for the five compositions: (a) thermal diffusivity; (b) thermal conductivity including 7YSZ as a reference; (c) C_p as a function of temperature; and (d) C_p as a function of ZrO_2 content.

Overall, these results demonstrate that co-doping with Y_2O_3 and Ta_2O_5 effectively suppresses phonon transport through combined mass contrast, ionic size mismatch, and strain-field effects, achieving stable and low k values without compromising phase stability. When correlated with the previously discussed microstructural observations, this behavior confirms that lattice disorder, rather than porosity or grain size, dominates the thermal transport response of the ZrO_2–Y_2O_3–Ta_2O_5 system, highlighting its potential as a next-generation thermal barrier ceramic.

CHAPTER 5: Results – Coatings

This chapter presents the results of the coating deposition and characterization processes carried out using the Suspension Plasma Spray (SPS) technique with a SinplexPro cascaded torch (see Figure 5.1). It begins with the characterization of the stainless-steel substrate (AISI 304L), confirming its single-phase austenitic structure and composition consistent with ASTM standards. Although not typically used in thermal barrier systems, this substrate served as a stable platform for the preliminary coating trials.

Subsequently, preliminary experiments using commercial 7YSZ powder were conducted to optimize spraying parameters with this plasma torch. Among the conditions evaluated, the coating obtained at a stand-off distance of 60 mm and a spray time of 4 min (sample S2) exhibited the most homogeneous and columnar microstructure, as well as the highest tetragonal phase content. These parameters were therefore selected as the reference condition for the deposition of 16YTZ coatings.

Coatings of 16YTZ were produced under the optimized conditions using mechanoactivated powders (16E30 and 16E40). The results demonstrated that particle size strongly influenced deposition rate, thickness, and porosity, while XRD analyses confirmed the predominance of $t' + c$ phases (83–90 wt%) and a low amount of monoclinic phase. Overall, the SPS process proved effective in producing dense, homogeneous coatings with high tetragonal phase content, features desirable for thermal barrier coating applications.

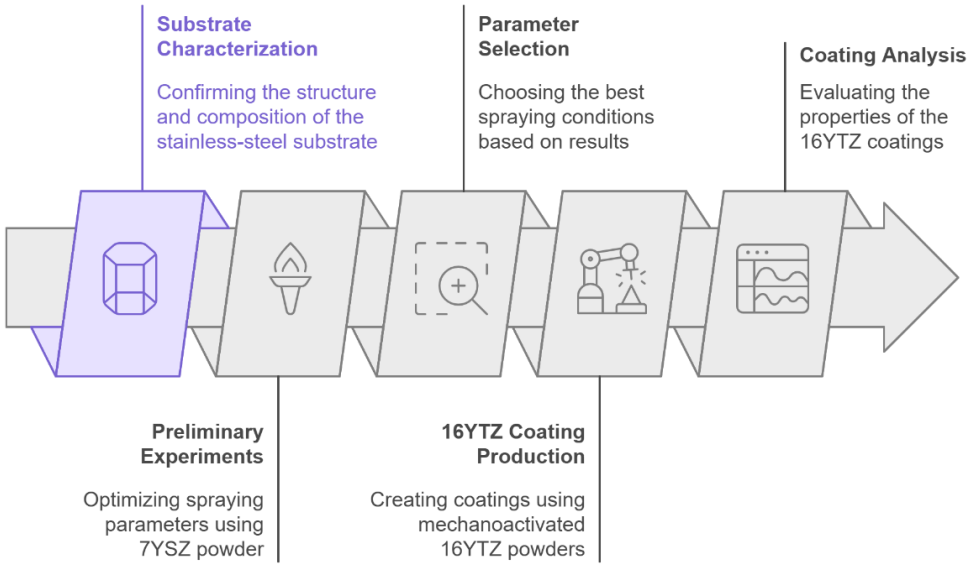


Figure 5.1 Scheme of the YTZ coating developed in this chapter.

5.1. Characterization of the substrate

The substrate used for coating deposition was analyzed by X-ray diffraction (XRD) and energy-dispersive spectroscopy (EDS) to confirm its phase composition and chemical nature. The XRD pattern (Figure 5.2) revealed the presence of a single face-centered cubic (γ) austenitic phase, with characteristic reflections at 2θ ≈ 43.69°, 50.89°, and 74.82°, corresponding to the (111), (002), and (022) planes of stainless steel. The ref. code used for the refinement was the ICSD 98-010-8132.

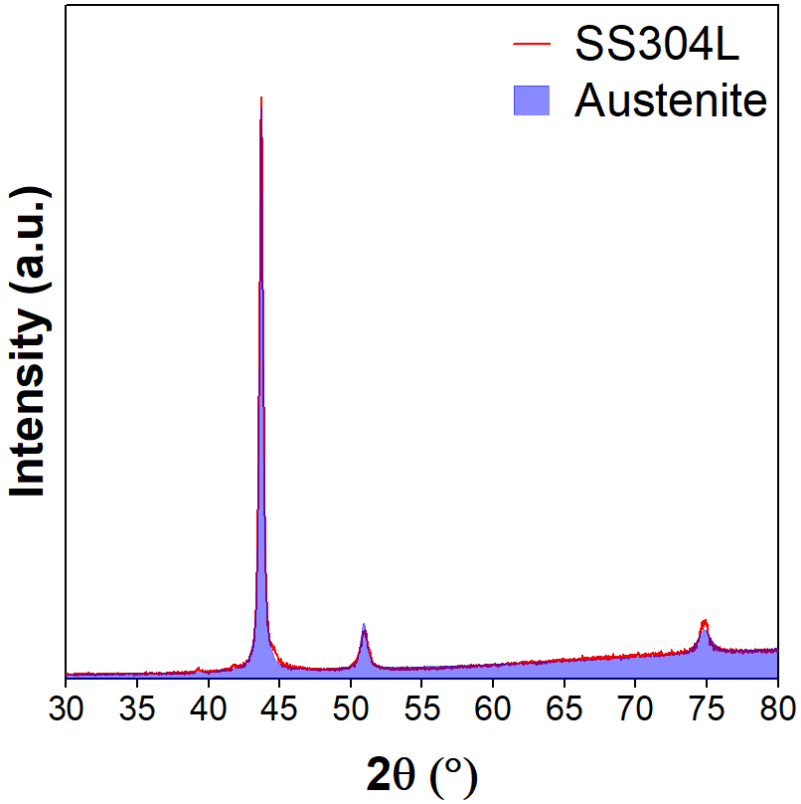


Figure 5.2 XRD pattern of the stainless-steel substrate showing the characteristic peaks of the face-centered cubic (γ) austenitic phase corresponding to AISI 304L. No secondary phases were detected.

The EDS analysis (Figure 5.3) indicated a composition of approximately Fe 67.0 wt%, Cr 18.0 wt%, Ni 7.2 wt%, and minor amounts of Mn, Si, and S, consistent with the nominal ranges defined for AISI 304L stainless steel (UNS S30403). According to ASTM A240/A240M-22, this alloy typically contains 18–20 wt% Cr, 8–12 wt% Ni, ≤2 wt% Mn, and ≤1 wt% Si, with the balance Fe.

Therefore, both the diffraction and compositional results confirm that the substrate corresponds to an austenitic stainless-steel grade 304L.

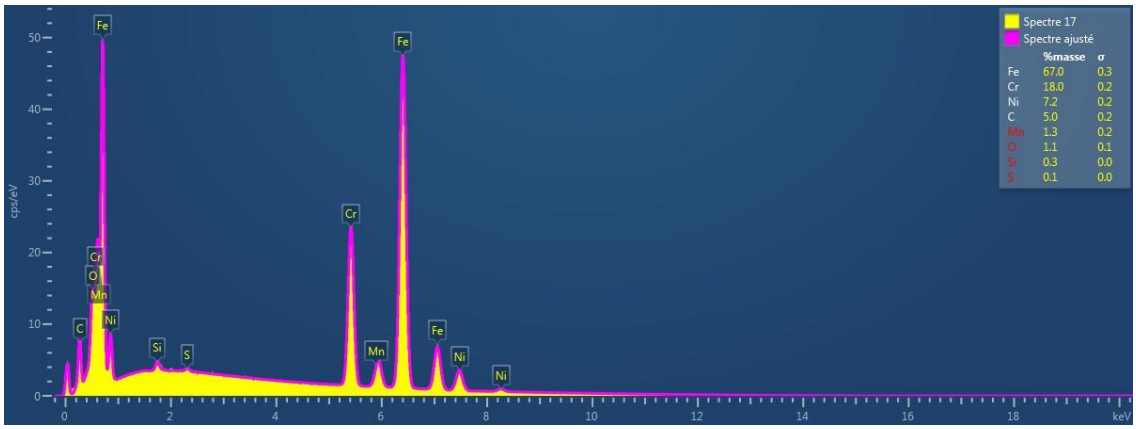


Figure 5.3 EDS spectrum of the substrate showing the main peaks of Fe, Cr, and Ni, confirming the chemical composition consistent with austenitic stainless-steel grade 304L.

Although AISI 304L stainless steel is not typically used in thermal barrier coating (TBC) systems, it was selected in this study as an accessible and stable substrate to conduct a preliminary evaluation of the YTZ coatings. The initial plan included transferring the process to a nickel-based superalloy to simulate a real TBC configuration; however, this stage could not be completed within the timeframe of this work. Nevertheless, the use of 304L provided representative information about the coating's behavior and valuable insight for future optimization on Ni-based alloys. The following section presents the preliminary deposition trials using YSZ coatings and phase stability and microstructure of the 16YTZ coatings.

5.2. Preliminary deposition trials using YSZ coatings

Before the deposition of the YTZ coatings, a series of preliminary depositions were carried out using suspensions prepared from commercial 7YSZ powder (Marion Technologies – Ref: 140.036.001). The objective of these exploratory tests was to identify the operating conditions that allowed obtaining a continuous and visually homogeneous coating using a SinplexPro cascaded plasma torch with a YSZ suspension. The last one was formulated with 20 wt.% solids and 2 wt.% dispersant, and the average particle size of the YSZ powder was approximately 700 nm. Table 5.1 summarizes the parameters used for each YSZ sample (S1–S5).

The coatings were sprayed using the SinplexPro-180 torch with an Ar/He plasma gas mixture (40/20 L min^{-1}) and a 9 mm nozzle diameter. The stand-off distance (SOD) varied from 60 mm to 100 mm [3], while the spraying time remained constant at 2 min, except for sample S2, where it was extended to the double in order to compare with the coating sample S1. After confirming that a uniform coating could still be obtained after 4 min, the parameters used for S2 were considered as a reference for the first deposits prepared with 16YTZ suspensions.

Table 5.1 Experimental parameters used for the preliminary YSZ coatings deposited from suspensions prepared with commercial YSZ powder.

Sample	Particle size (nm)	Plasma gas mixture	Gases ratio (L/min)	Nozzle diameter (mm)	Stand-off distance (mm)	Spray time (min)
S1	700	Ar/He	40/20	9	60	2
S2					60	4
S3					70	2
S4					80	2
S5					100	2

Figure 5.4(a) shows the XRD patterns of the coatings obtained under these conditions. All samples displayed the characteristic peaks of the tetragonal phase of zirconia, although slight quantity of m-ZrO_2 was detected. Among them, sample S2 exhibited the highest tetragonal phase content (75%), suggesting that the combination of SOD = 60 mm and spraying time = 4 min provided sufficient particle melting without inducing excessive thermal decomposition.

The corresponding SEM micrographs (Figure 5.4(b)) reveal a clear dependence of the coating morphology on the spraying parameters. Samples S1, S3, and S5 showed heterogeneous structures with partially melted regions and interlamellar porosity, indicative of incomplete melting or limited particle flattening during impact [26], [129]. In contrast, samples S2 and S4 exhibited more homogeneous and compact microstructures, characterized by better splat coalescence and reduced porosity.

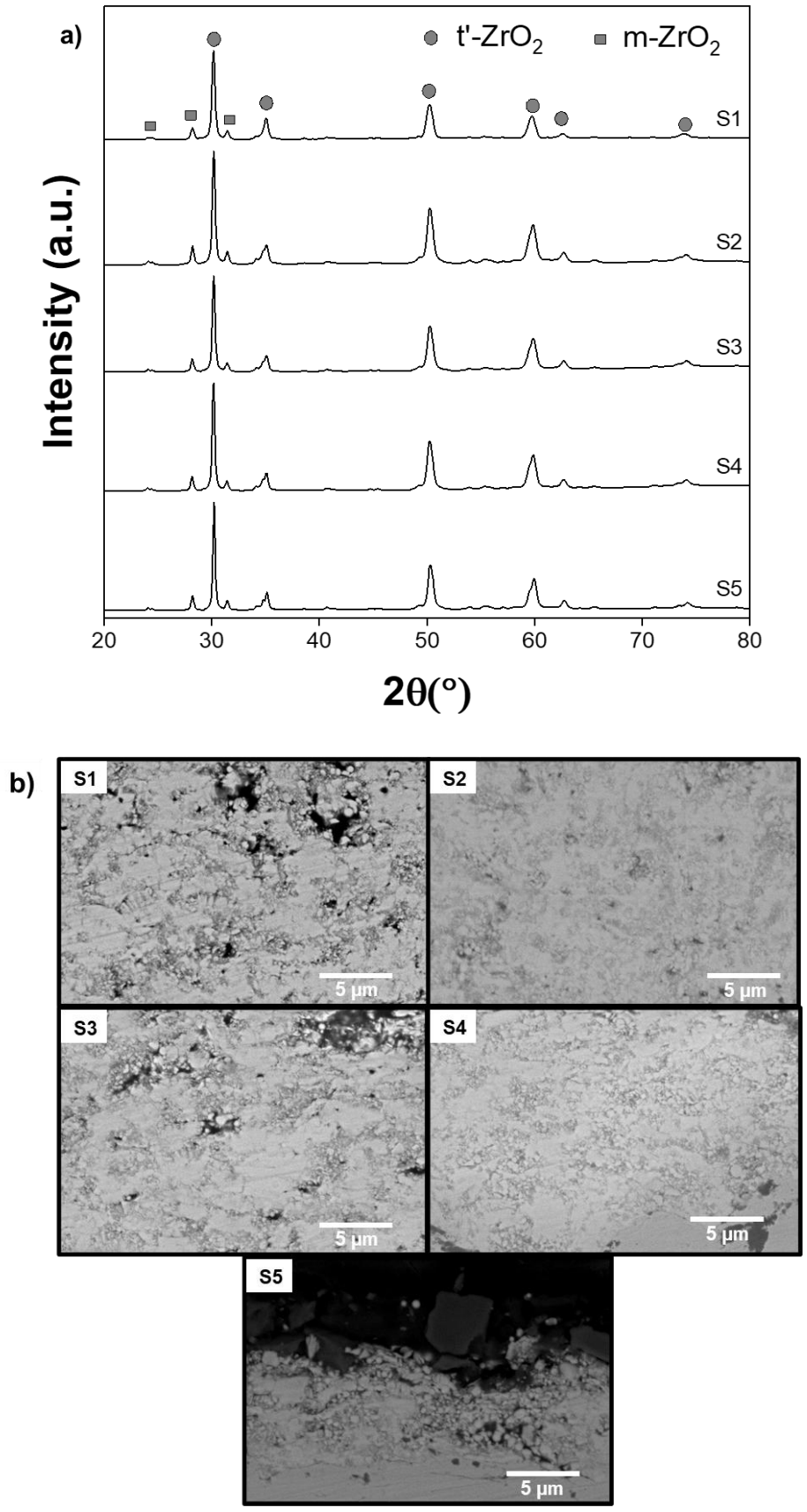


Figure 5.4 (a) XRD patterns and (b) cross-sectional SEM micrographs of YSZ coatings deposited under different spraying conditions (samples S1–S5).

Among all coatings, sample S2 presented the most uniform and dense morphology, indicating an optimal balance between particle temperature and impact velocity. This condition favored efficient deposition, leading to good splat cohesion and improved surface continuity. Moreover, the XRD results confirmed that this microstructural improvement was accompanied by a greater retention of the tetragonal phase.

Therefore, the parameters corresponding to sample S2 were selected as the reference condition for subsequent coatings prepared with 16YTZ suspensions, since it appears that these parameters result in a stable deposition process capable of producing dense coatings with a predominantly tetragonal structure.

5.3. Phase stability and microstructure of 16YTZ coatings

After selecting the optimal spraying parameters from the YSZ preliminary tests (sample S2), the next step involved applying these conditions to the deposition of the 16YTZ coatings. The objective was to verify if the optimized parameters would also allow obtaining homogeneous and adherent coatings with this new composition. Maintaining constant the torch configuration and the suspension formulation ensured a consistent comparison between both systems, isolating the influence of the powder composition and particle characteristics.

Due to the complexity of obtaining the non-transformable tetragonal phase of the 16YTZ powder, coatings were deposited using the mechanoactivated feedstock (16E30 (D50 ~700 nm) and 16E40 (D50 ~450 nm), i.e. without the calcination treatment for solid state reaction, see Fig. 2.3) under the conditions specified in Table 2.2 shown in the chapter 2. Table 5.2 shows the characteristics of the coatings as a function of stand-off distance and feedstock powders used [3]. A change in deposition rate was observed based on the particle size of the feedstock, while the spraying parameters remained constant. The deposit made with larger particles (sample A1) shows a higher deposition rate, resulting in a coarser coating (130 µm) with greater roughness (7.64 ± 0.02 µm). This suggests that larger particles may be more effectively directed towards the substrate. In

contrast, the lower deposition rate of the B samples, which is the same regardless of the stand-off distance, might be explained by the vaporization of the smaller particles in the plasma jet or because the small particles might be bouncing off the surface, which would reduce the amount of deposited material [3].

Table 5.2 Characteristics of the coatings obtained using 16E30 and 16E40 powder feedstock. [3]

Coating	Feedstock	Stand-off distance, mm	Deposition rate, µm/min	Thickness, µm	Roughness, µm	Porosity, %
A1	16E30	60	33	130	7.64 ± 0.02	4.75 ± 0.04
B1	16E40	60	22	89	6.16 ± 0.06	6.28 ± 0.75
B2		70	21	85	6.22 ± 0.26	13.61 ± 0.58
B3		80	22	86	6.10 ± 0.06	17.48 ± 0.62

XRD patterns of the coatings deposited under the different conditions are shown in Fig. 5.5(a-b). These diffraction patterns were analyzed using the same criteria as applied to the dense samples. Quantification results for the *t'*-phase, along with their respective tetragonality values, lattice parameters, and *t'*+*c* zirconia phases are shown in Fig. 5.5(c-d). Phase identification was performed through Rietveld refinement of the XRD patterns (see Fig. 5.6), where the additional phases to *t'*-phase, such as ZrO_2 (monoclinic, space group: P 1 21/c 1; cubic, space group: F m -3 m), Y_2O_3 (cubic, space group: I a -3), and Ta_2O_5 (orthorhombic, space group: P m m 2) were identified [3]. Rietveld refinements were carried out using structural information from the following references: *o*-Ta_2O_5 (ICSD collection code: 66366) [130], *c*-Y_2O_3 (ICSD collection code: 27772) [131], *c*-ZrO_2 (ICSD collection code: 89429) and *m*-ZrO_2 (ICSD collection code: 60900) [3], [132]. For this study, a tetragonal structure was employed for YTZ [133], with Ta and Y atoms incorporated at 16 at.% each (see the annex 2,Table A2.2). The results show the presence of less than 10 wt.% of the *m*-ZrO_2 phase, and the rest is a combination of mainly tetragonal and cubic phases. For comparative purposes between the coatings deposited by different conditions, the content of tetragonal and cubic phases is reported together, since both are of interest for TBCs. In general, the *t'*+ *c*-phases account for about 83-90 wt.% [3].

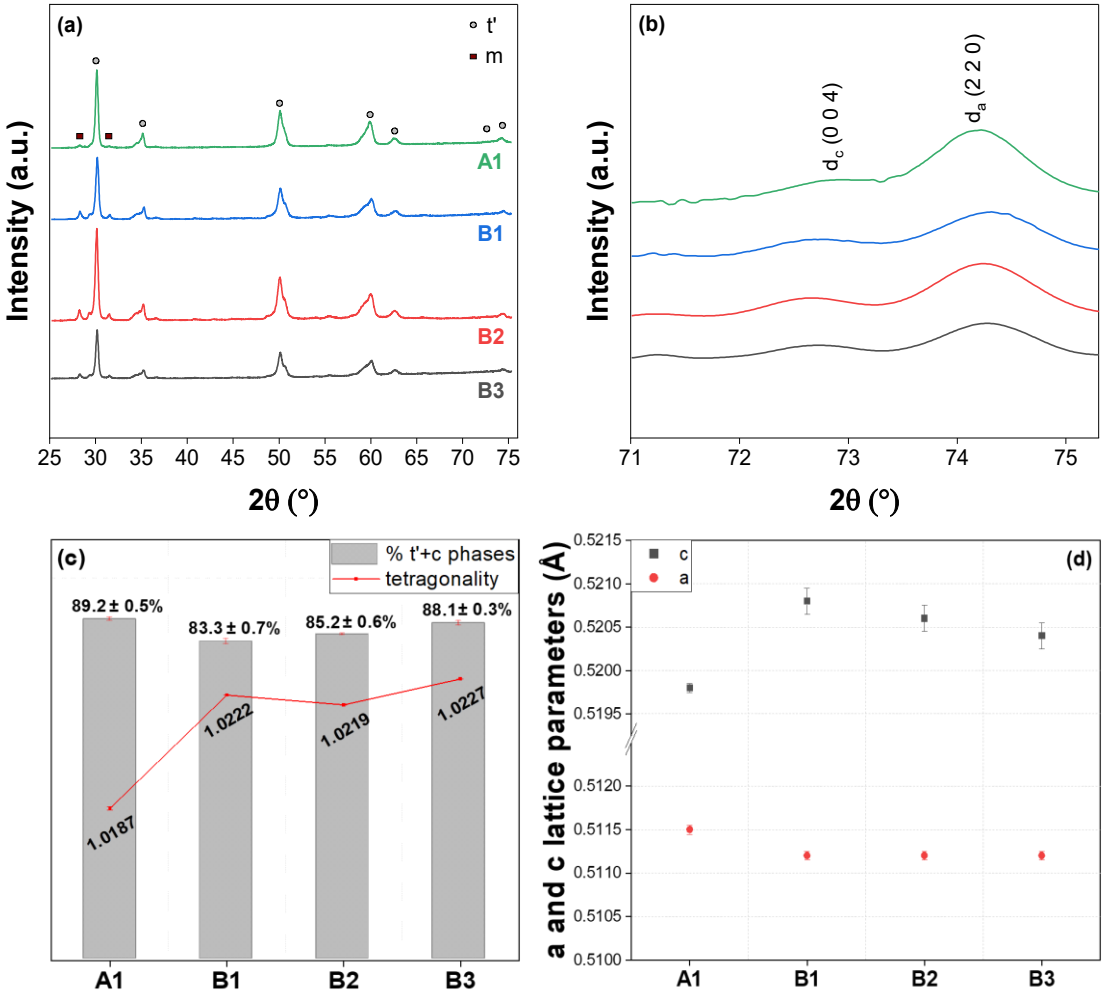


Figure 5.5 (a) XRD patterns of A1 and B1-B3 coatings obtained by SPS technique, (b) characteristic peaks corresponding to *t'*-phase, (c) values of tetragonality and % *t'*-phase, and (d) lattice parameters of *t'*-phase of A1 and B1-B3 coatings.

Although these *t'*+*c*-phase contents are lower than in the sintered samples, and some differences are observed depending on the spraying parameters, the results are very interesting because they demonstrate the feasibility of having a reactive spraying process, that promotes the synthesis of zirconia phases with potential applications in TBCs [3]. More specifically, an increase in the particle size distribution of the starting powder correlates with a higher proportion of the tetragonal and cubic phases in the coating. For instance, coating A1 (prepared with powder of D50 ~700 nm) showed more *t'*+*c*-phases (89.2 ± 0.5 wt.%) than in B coatings (prepared with powder of D50 ~450 nm) [3]. Furthermore, for the same particle size distribution (B coatings), the stand-off distance does not seem to influence the tetragonality value (~1.022) but increases

the *t'*+c-phase percentage (from 83.3 to 88.1 wt.%). However, although the maximum amount of *t'*+*c* phase is reached at a stand-off distance of 60 mm for the A1 coating, it is observed to exhibit a lower tetragonality (~1.019). As mentioned above, the tetragonality value is significant because it directly correlates with the fracture toughness through the activation of a ferroelasticity mechanism [3].

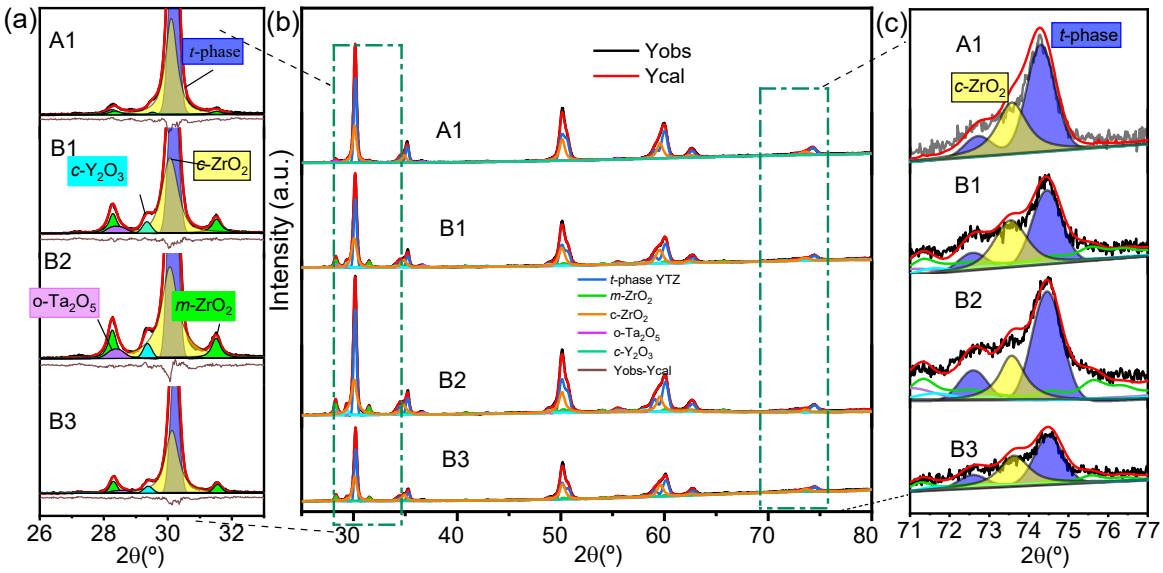


Figure 5.6 Rietveld refinement of XRD patterns for phases quantification in the coatings: (a) close-up of the fit within the 2θ = 26-30° range, (b) full refinement fit overview, and (c) last peaks of the diffraction pattern to determine the tetragonality of the system and the lattice parameters.

The A1 coating deposition condition (with powder of D50 ~ 700 nm) shows lower tetragonality and higher percentage of *t'*+*c*-phases. This result may be attributed to the larger particle size, which favors the stability of the *t'*+*c*-phases at room temperature, but with reduced unit cell distortion [3]. The condition with the feedstock of D50 ~ 450 nm (B1, B2 and B3 coatings), presents higher tetragonality and lower percentage of *t'*-phase, which may indicate that it has smaller particles that induce more internal stresses, which increases the structural distortion (higher tetragonality) and promotes the transformation to other phases (such as the monoclinic and cubic phase). Further study of these ferroelasticity phenomena with transmission electron microscopy, atomic force microscopy and nanoindentation techniques is required [3].

Figure 5.7 shows the microstructure results of the coatings, from which porosity percentages were determined through image analysis. Additionally, roughness and thickness values are shown in Table 5.2. Coatings A1 and B1, obtained at the same stand-off distance, present the lowest porosity (5% and 6%, respectively), with a slightly lower percentage for coating A1 [3]. In contrast, the coating B3 obtained at the highest stand-off distance (80 mm) presents the highest porosity values of 17%. Coatings A1 and B1 present a morphology resembling a columnar structure, which is promising for thermal barrier applications, since columnar deposits imply a pore architecture that results in low thermal conductivity values, potentially lower than those of *t'*-YSZ coatings with the same microstructure [3], [134].

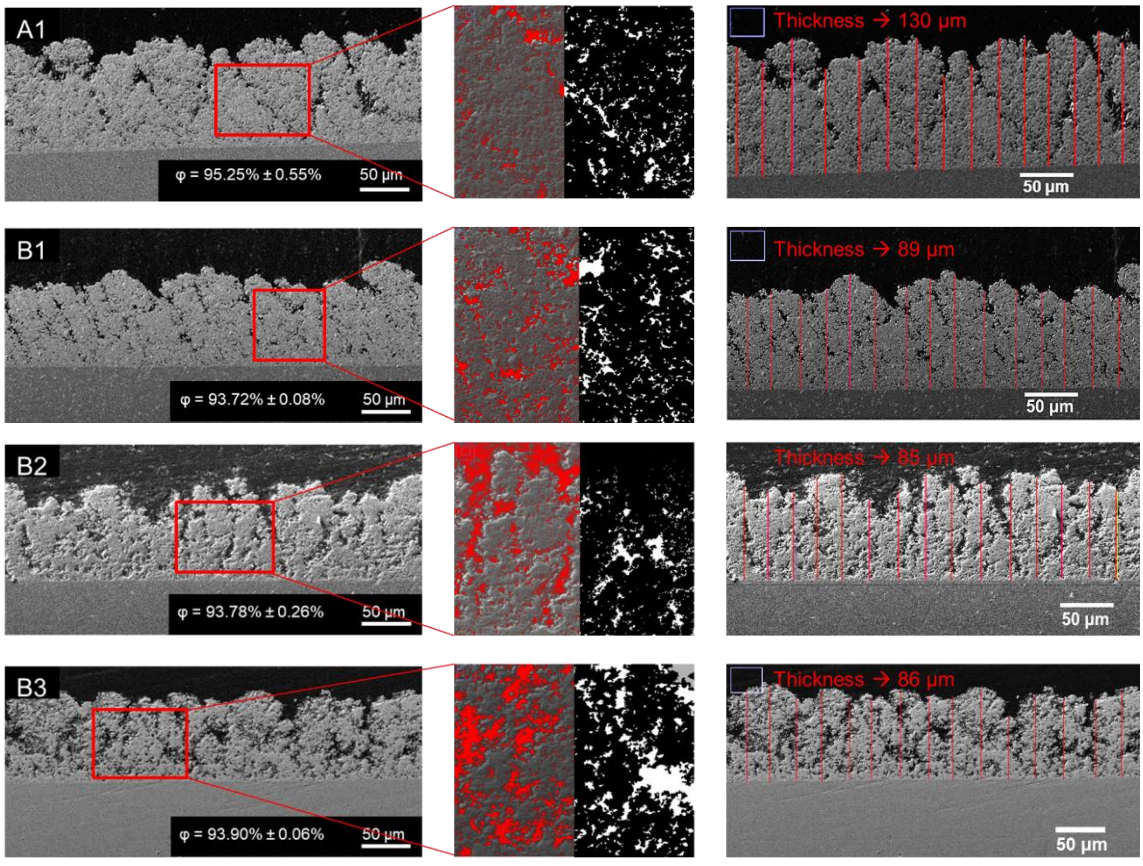


Figure 5.7 SEM images of the cross sections of the coatings made by SPS process.

Overall, reaching 89.2 ± 0.5wt.% of *t'*+*c*-phases, together with a low porosity of less than 5% is a highly positive outcome for this experimental setup. This is related to the fact that the coating showed a tetragonality value of 1.0187, which is higher than that of the YSZ (1.0116) [3], [135].

On the other hand, this research shows that the coatings manufactured by SPS exhibit certain advantages compared to those manufactured by APS [3], [118]. First, SPS-manufactured coatings possess *t'*-phase in their as-sprayed condition, and no further heat treatment is needed to achieve the *t'*-phase [118]. Second, coatings obtained by SPS present a homogeneous microstructure, and no half-molten particles or microcracks are observed. Thirdly, coatings manufactured by SPS can reach a lower porosity, 4.751%, than those manufactured by APS, 9.3% [3], [118]. Finally, the microstructure and the high tetragonality reached by the coatings manufactured by SPS can bring about a higher thermal shock resistance, lower thermal conductivity, and improved mechanical properties [24], [25] than those manufactured by APS [3], [118].

The decision to use 304L stainless steel as a substrate was mostly practical, but it has an important consequence: it behaves very differently from the Ni-based superalloys used in actual turbine components. Because 304L has a lower thermal expansion coefficient (~ 16.9×10^{-6} K^{-1} at ~100 °C) in comparison with a Inconel 718 Ni-based superalloy (~ 13×10^{-6} K^{-1} at ~100 °C) [26], the ceramic coating experiences a stronger thermal mismatch during cooling, which translates into higher residual tensile stresses in the layer.

These stresses can influence how the coating adheres, how cracks appear, and how stable the layer remains under repeated heating and cooling. Recognizing this difference is important because the trends and behaviors observed in this work will serve as a basis for the next step: applying the optimized conditions to Ni-based substrates, where the stress state and overall compatibility with the ceramic layer will be closer to real service conditions.

Building on this, the results presented in this chapter should also serve as a foundation for future experimental designs that incorporate the spray parameters described in Table 2.2, allowing these conditions to be refined so that coatings with the desired phase and microstructural characteristics can be reliably obtained for thermal barrier applications [3].

LIMITATIONS AND FUTURE WORKS

Limitations

The deposition of YTZ-based compositions by SPS had not been previously reported in the literature, which required an exploratory, trial-and-error approach to define suitable spray parameters and limited the possibility of building upon established processing windows.

Thermal and mechanical characterizations in dense ceramics were mostly performed under steady-state conditions, without extensive in-situ, high-temperature, or long-term thermal cycling experiments, restricting the evaluation of degradation mechanisms and long-term stability.

The SPS coatings were deposited on stainless steel instead of a Ni-based superalloy, preventing a realistic assessment of thermo-mechanical compatibility, TGO growth, or adhesion behavior under conditions representative of actual thermal barrier coating systems.

The microstructural analysis relied primarily on 2D techniques such as SEM and XRD, without complementary 3D or orientation-resolved methods (e.g., full EBSD mapping, FIB-SEM), which limited the resolution of fine defects, texture development, and ferroelastic domain structures.

Future works

Develop a systematic SPS parameter map for YTZ compositions, building on the exploratory results of this thesis to establish optimized conditions for columnar/feathery architectures and improved thermal performance.

Evaluate coatings deposited on Ni-based superalloys to determine thermo-mechanical compatibility, TGO evolution, oxidation resistance, and thermal-shock behavior under service-like conditions.

Produce SPS coatings using all the YTZ compositions synthesized in this work, allowing a direct correlation between chemical composition, microstructure, and properties at coating levels.

Extend thermal and mechanical testing to high-temperature and cyclic conditions, including in-situ measurements and thermal fatigue. Future work should

include the direct determination of Young's modulus and fracture toughness of the coatings to assess thermal stress development under service-relevant conditions.

Apply advanced 3D and crystallographic characterization techniques such as full EBSD orientation mapping and FIB-SEM serial sectioning to obtain a deeper understanding of porosity networks, microstructural anisotropy, and ferroelastic domain behavior.

Incorporate numerical modeling and simulations (i.e. DFT calculations) to quantitatively evaluate dopant effects, stress distribution, and microstructure-property relationships in YTZ systems.

CONCLUSIONS

The characterization of the precursors and powders of the YTZ system established the appropriate conditions for obtaining the non-transformable tetragonal phase (t′). The thermal preheating at 1000 °C affected only Ta_2O_5, while ZrO_2 and Y_2O_3 maintained their stable phases; however, this preheating was not decisive for the subsequent formation of the t′-phase. All precursors showed a strong tendency to agglomerate, highlighting the need for an efficient milling process to achieve submicrometric particle sizes.

For the 16YTZ composition, high-energy ball milling proved to activate the system more effectively, enabling the formation of the t′-phase with only 2 h of sintering, unlike the 20 h required when using conventional planetary milling. Extending the sintering time beyond this did not produce significant improvements in tetragonality or phase purity.

The five YTZ compositions (15.4–17.8 mol%) exhibited similar particle-size distributions after planetary ball milling and, after sintering at 1500 °C, all showed predominance of the t′-phase with slight variations in tetragonality associated with the total dopant content. High-energy ball milling was the most efficient technique for obtaining fine, homogeneous powders suitable for use as raw material in SPS suspensions.

The five dense ceramics of the YTZ system (15.4P1, 16P1, 16.6P1, 17.2P1, and 17.8P1), sintered at 1500 °C for 20 h, exhibited an effective stabilization of the non-transformable tetragonal phase (t′), with t′ fractions close to 98–99 wt.% across all compositions. Tetragonality increased progressively with total dopant content, confirming the combined influence of Y^{3+} and Ta^{5+} on lattice distortion and phase stability. Microstructural analysis revealed equiaxed, highly densified grains (>99% densification), with grain size increasing gradually as dopant concentration increased due to enhanced grain boundary mobility driven by Y/Ta segregation.

SEM, EBSD, and Raman analyses confirmed the dominance of t′-ZrO_2, the absence of preferred crystallographic texture, and the consistency between surface and bulk microstructures. The comparison of milling routes in

16YTZ composition showed that high-energy ball milling produces finer particles, greater surface activation, and enables t′-phase formation with significantly shorter sintering times compared to conventional planetary ball milling.

Mechanically, the ceramics exhibited stable Vickers hardness values (7.9–8.7 GPa) and toughness values of ~43–50 J/m^2. Nanoindentation results for the two extreme compositions showed characteristic nano-hardness values of $H_0 \approx$ 15.9 GPa for 15.4P1 and $H_0 \approx$ 16.5 GPa for 17.2P1, together with characteristic reduced Young's moduli of $E_0 \approx$ 205 GPa and $E_0 \approx$ 220 GPa, respectively. The load–displacement curves revealed deformation governed by the interplay of elasticity, localized plasticity, and ferroelastic events, and Weibull analysis indicated homogeneous and comparable mechanical distributions across samples.

Thermally, all compositions displayed low thermal diffusivity and low thermal conductivity (1.3–1.9 W·m^{-1}·K^{-1}), below that of 7YSZ and nearly temperature-independent up to 1000 °C. This behavior is governed by strong phonon scattering from mass contrast and lattice strain introduced by Y and Ta co-doping, rather than microstructural effects or porosity.

During the SPS process, the mixture of oxide powders underwent phase transformations in the plasma jet, resulting in t′ + c phase contents between 80 and 90% in the coatings. This transformation level is directly influenced by the spray parameters. Since no prior reports exist on spraying this ternary YTZ system using SPS, these results open new possibilities for future applications of this technique.

Some of the conditions evaluated produced relatively uniform, columnar-like microstructures, indicating promising potential for further optimization. In particular, coatings deposited with Ar/He = 40/20 slpm, 500 A, 60 mm stand-off distance, and feedstock powders obtained by high-energy ball milling (~700 nm, 1700 rpm) exhibited very low porosity (<5%) and a tetragonality of 1.0187, lower than that of the dense ceramics but still higher than typical YSZ coatings.

Overall, the results demonstrate that the YTZ system exhibits high phase stability, dense and homogeneous microstructures, robust mechanical

performance, and excellent thermal insulation, positioning it as a strong candidate for next-generation thermal barrier ceramics. At the coating level, the SPS process proved capable of producing YTZ layers with high t′ + c phase content (80–90%), low porosity, and uniform—sometimes columnar—microstructures, confirming that reactive synthesis in the plasma jet is feasible for this system. Together, the dense ceramics and SPS coatings reveal a coherent material response across all processing scales, establishing YTZ as a promising route for advanced thermal-barrier applications and opening the door to future optimization studies in both bulk and coating forms.

REFERENCES

[1] L. Guo, W. He, W. Chen, Z. Xue, J. He, Y. Guo, Y. Wu, L. Gao, D. Li, Z. Zhang, L. Wei, Y. Gao, T. Zhang, J. Qiao, Q. Li and H. Guo, “Progress on high-temperature protective coatings for aero-engines,” *Surf. Sci. Technol.*, vol. 1, no. 1, 2023, Art. No. 6, doi: 10.1007/s44251-023-00005-6.

[2] D.R. Clarke, M. Oechsner and N.P. Padture, “Thermal-barrier coatings for more efficient gas-turbine engines,” *MRS Bull.*, vol. 37, no. 10, pp. 891-898, 2012, doi: 10.1557/mrs.2012.232.

[3] C. Galeano-Camacho, I. Bedoya-Trujillo, S. Pérez, H. Ageorges, and J. Muñoz-Saldaña, "Analysis of the t′ + c phase content from ZrO_2–16 mol.% Y_2O_3–16 mol.% Ta_2O_5 mechanoactivated powder mixtures in coatings deposited by suspension plasma spraying," *J. Therm. Spray Technol.*, vol. 34, pp. 783–794, 2025, doi: 10.1007/s11666-025-01946-0.

[4] J.R. Davis, Ed. *Handbook of thermal spray technology*, Materials Park, OH: ASM Int., 2004.

[5] K.A. Omran, M. Sayed, M.A. El-Meniawi, E.M. Sallam, and S.M. Naga, “A review on thermal barrier coatings,” *Egypt. Int. J. Eng. Sci. Technol.*, vol. 36, pp. 1-6, 2021, doi: 10.21608/eijest.2021.79363.1070.

[6] J.J. Swab, “Role of oxide additives in stabilizing zirconia for coating applications,” Army Res. Lab., Durh., NC, Rep. ARL-TR-2591, 2001.

[7] W. Ma and H. Dong, “Ceramic thermal barrier coating materials,” in *Thermal Barrier Coatings*. Cambridge, U.K.: Woodhead Publ., 2011: pp. 25–52, doi: 10.1533/9780857090829.1.25.

[8] S. Bose, *High temperature coatings*, Manchester, CT: Elsevier Sci. and Technol. Books, Jan. 2007.

[9] M. C. Gurak, “Studies of the yttrium tantalate-zirconium oxide quasi-binary,” Ph.D. thesis, School of Eng. Appl. Sci., Harvard Univ., Cambridge, MA, 2017. [Online]. Available: http://nrs.harvard.edu/urn-3:HUL.InstRepos:40046543.

[10] D.B. Marshall, “Transformation toughening of ceramics,” Air Force Office of Sci. Res., Bolling Air, DC, Rep. AD-A248 903, 1992.

[11] J. Kim, “Effect of Ta_2O_5, Nb_2O_5, and HfO_2 Alloying on the Transformability of Y_2O_3-Stabilized Tetragonal ZrO_2,” *J. Amer. Ceram. Soc.*, vol. 73, no. 1, pp. 115-120, 1990, doi: 10.1111/j.1151-2916.1990.tb05100.x.

[12] J. Li, Q. Zhou, L. Yang, Y. Zhou, J. Zhao, J. Huang, and Y. Wei, “Ferroelastic deformation mechanism and mechanical properties of [001]-oriented YSZ film by indentation,” J. Alloys Compd., vol. 889, 2022, Art. no. 161557, doi: 10.1016/j.jallcom.2021.161557.

[13] J. Wang, L. Chen, M. Wang, C. Zhang, Y. Yu, J. Sun, X. Chen, Y. Wang, P. Liu and Q. Jing, "Influence of Gd_2O_3 substitution on thermal and mechanical

properties of ZrO_2–Ta_2O_5–Y_2O_3," *J. Eur. Ceram. Soc.*, vol. 41, pp. 1654–1663, 2021, doi: 10.1016/j.jeurceramsoc.2020.10.011.

[14] R.L. Jones, R.F. Reidy, and D. Mess, “Scandia, yttria-stabilized zirconia for thermal barrier coatings,” *Surf. Coat. Technol.*, vol. 82, pp. 70-76, 1996, doi: 10.1016/0257-8972(95)02646-0.

[15] N. M. Abdul-Jabbar, A. N. Fernandez, R. W. Jackson, D. Park, W. D. Summers, and C. G. Levi, "Interactions between zirconia–yttria–tantala thermal barrier oxides and silicate melts," *Acta Mater.*, vol. 185, pp. 171–180, 2020, doi: 10.1016/j.actamat.2019.11.060.

[16] M. Gurak, Q. Flamant, L. Laversenne, and D. R. Clarke, "On the yttrium tantalate–zirconia phase diagram," *J. Eur. Ceram. Soc.*, vol. 38, pp. 3317–3324, 2018, doi: 10.1016/j.jeurceramsoc.2018.03.012.

[17] S. Raghavan, H. Wang, W. D. Porter, R. B. Dinwiddie, and M. J. Mayo, "Thermal properties of zirconia co-doped with trivalent and pentavalent oxides," *Acta Mater.*, vol. 49, pp. 169-179, 2001, doi: 10.1016/s1359-6454(00)00295-0.

[18] Y. Shen, R. M. Leckie, C. G. Levi, and D. R. Clarke, "Low thermal conductivity without oxygen vacancies in equimolar $YO_{1.5}$ + $TaO_{2.5}$- and $YbO_{1.5}$ + $TaO_{2.5}$-stabilized tetragonal zirconia ceramics," *Acta Mater.*, vol. 58, pp. 4424–4431, 2010, doi: 10.1016/j.actamat.2010.04.040.

[19] P. L. Fauchais, J. V. R. Heberlein, and M. I. Boulos, *Thermal Spray Fundamentals: From Powder to Part,* New York, NY: Springer, 2014.

[20] S. Mahade, R. Li, N. Curry, S. Björklund, N. Markocsan, and P. Nylén, "Isothermal oxidation behavior of $Gd_2Zr_2O_7$/YSZ multilayered thermal barrier coatings," *Int. J. Appl. Ceram. Technol.*, vol. 13, pp. 443–450, 2016, doi: 10.1111/ijac.12527.

[21] B. Liang and C. Ding, "Thermal shock resistances of nanostructured and conventional zirconia coatings deposited by atmospheric plasma spraying," *Surf. Coat. Technol.*, vol. 197, pp. 185–192, 2005, doi: 10.1016/j.surfcoat.2004.08.225.

[22] X. Chen, H. Honda, S. Kuroda, H. Araki, H. Murakami, M. Watanabe, and Y. Sakka, "Highly segmented thermal barrier coatings deposited by suspension plasma spray: Effects of spray process on microstructure," *J. Therm. Spray Technol.*, vol. 25, pp. 1638–1649, 2016, doi: 10.1007/s11666-016-0469-6.

[23] J. Lee, S. Lee, H. N. Han, W. Kim and N. M. Hwang, "Yttrium oxyfluoride coatings deposited by suspension plasma spraying using coaxial feeding," *Coatings*, vol. 10, 2020, Art. no. 481, doi: 10.3390/coatings10050481.

[24] W. Fan and Y. Bai, "Review of suspension and solution precursor plasma sprayed thermal barrier coatings," *Ceram. Int.*, vol. 42, pp. 14299–14312, 2016, doi: 10.1016/j.ceramint.2016.06.063.

[25] E. Meillot, S. Vincent, C. Caruyer, D. Damiani, and J.-P. Caltagirone, "Modelling the interactions between a thermal plasma flow and a continuous liquid jet in a suspension spraying process," *J. Phys. D: Appl. Phys.*, vol. 46, 2013, Art. no. 224017, doi: 10.1088/0022-3727/46/22/224017.

[26] A. G. Gonzalez Hernandez, “Étude du comportement à haute température de revêtements nanostructurés élaborés par projection thermique (combustion et plasma) à partir de poudres et de suspensions”, Ph.D. thesis, Faculté Sci. Tech., Univ. de Limoges, France; Univ. de Antioquia, Medellín, 2014. [Online]. Available: https://theses.hal.science/tel-03336283

[27] G. Darut, H. Ageorges, A. Denoirjean, and P. Fauchais, "Tribological performances of YSZ composite coatings manufactured by suspension plasma spraying," *Surf. Coat. Technol.*, vol. 217, pp. 172–180, 2013, doi: 10.1016/j.surfcoat.2012.12.008.

[28] A. G. González, H. Ageorges, O. Rojas, E. López, F. M. Hurtado, F. Vargas, "Efecto de la microestructura y de la microdureza sobre la resistencia al desgaste de recubrimientos elaborados por proyección térmica por plasma atmosférico a partir de circona-alúmina, circona-itria y circona-ceria," *Bol. Soc. Esp. Ceram. Vidrio*, vol. 54, pp. 124–132, 2015, doi: 10.1016/j.bsecv.2015.05.005.

[29] Y. Yao, D. Wu, X. Zhao, and F. Yang, "Premature failure induced by non-equilibrium grain-boundary tantalum segregation in air-plasma sprayed ZrO_2−$YO_{1.5}$−$TaO_{2.5}$ thermal barrier coatings," *Int. J. Miner. Metall. Mater.*, vol. 29, pp. 2189–2200, 2022, doi: 10.1007/s12613-021-2394-z.

[30] F.-L. Toma, S. Gruber, A. Selbmann, S. Tkachenko, O. Kunze, K. Zabransky, C. Leyens, L. Čelko, and M. Tajmar, "Performance of suspension sprayed YSZ thermal barrier coatings on Inconel 718 substrates produced by laser powder bed fusion," in *Proc. Int. Thermal Spray Conf. (ITSC)*, 2022, pp. 645–653, doi: 10.31399/asm.cp.itsc2022p0645.

[31] H. G. Scott, "Phase relationships in the zirconia–yttria system," *J. Mater. Sci.*, vol. 10, pp. 1527–1535, 1975, doi: 10.1007/bf01031853.

[32] R. C. Garvie, R. H. Hannink, and R. T. Pascoe, "Ceramic steel?," *Nature*, vol. 258, no. 5537, pp. 703–704, 1975, doi: 10.1038/258703a0.

[33] E. C. Subbarao, H. S. Maiti, and K. K. Srivastava, "Martensitic transformation in zirconia," *Phys. Status Solidi A*, vol. 21, pp. 9–40, 1974, doi: 10.1002/pssa.2210210102.

[34] R. C. Garvie, "The occurrence of metastable tetragonal zirconia as a crystallite size effect," *J. Phys. Chem.*, vol. 69, pp. 1238–1243, 1965, doi: 10.1021/j100888a024.

[35] J. A. Muñoz Tabares, “Una visión general de los cerámicos de circona – estructura, propiedades y aplicaciones,” *Revista Colomb. Mater.*, vol. 2, no. 2, 2012, doi: 10.17533/udea.rcm.11289

[36] D.-J. Kim and T.-Y. Tien, "Phase stability and physical properties of cubic and tetragonal ZrO_2 in the system ZrO_2–Y_2O_3–Ta_2O_5," *J. Amer. Ceram. Soc.*, vol. 74, pp. 3061–3065, 1991, doi: 10.1111/j.1151-2916.1991.tb04302.x.

[37] D. J. Green, R. H. J. Hannink, and M. V. Swain, *Transformation Toughening of Ceramics*. Boca Raton, FL: CRC Press, 1989.

[38] S. G. Heinze, A. R. Natarajan, C. G. Levi, and A. Van der Ven, "Crystallography and substitution patterns in the ZrO_2–$YTaO_4$ system," *Phys. Rev. Mater.*, vol. 2, 2018, Art. no. 073607, doi: 10.1103/PhysRevMaterials.2.073607.

[39] G. M. Wolten, "Diffusionless phase transformations in zirconia and hafnia," *J. Amer. Ceram. Soc.*, vol. 46, pp. 418–422, 1963, doi: 10.1111/j.1151-2916.1963.tb11768.x.

[40] S. Fabris, A. T. Paxton, and M. W. Finnis, "Free energy and molecular dynamics calculations for the cubic–tetragonal phase transition in zirconia," *Phys. Rev. B*, vol. 63, 2001, Art. no. 094101, doi: 10.1103/PhysRevB.63.094101.

[41] P. M. Kelly and L. R. F. Rose, "The martensitic transformation in ceramics – its role in transformation toughening," *Prog. Mater. Sci.*, vol. 47, pp. 463-557, 2002.

[42] A. G. Evans and R. M. Cannon, "Overview no. 48: Toughening of brittle solids by martensitic transformations," *Acta Metall.*, vol. 34, pp. 761–800, 1986, doi: 10.1016/0001-6160(86)90052-0.

[43] J. Chevalier, L. Gremillard, A. V. Virkar, and D. R. Clarke, "The tetragonal–monoclinic transformation in zirconia: Lessons learned and future trends," *J. Amer. Ceram. Soc.*, vol. 92, pp. 1901–1920, 2009, doi: 10.1111/j.1551-2916.2009.03278.x.

[44] A. H. Heuer, N. Claussen, W. M. Kriven, and M. Rühle, "Stability of tetragonal ZrO_2 particles in ceramic matrices," *J. Amer. Ceram. Soc.*, vol. 65, pp. 642–650, 1982, doi: 10.1111/j.1151-2916.1982.tb09946.x.

[45] F. M. Pitek, “A Study of the Zirconia–Yttria–Tantala System as a Potential Thermal Barrier Oxide,” Ph.D. thesis, Univ. of Calif., Santa Barbara, CA, 2006. [Online]. Available: https://www.proquest.com/dissertations-theses/study-zirconia-yttria-tantala-system-as-potential/docview/305349149/se-2.

[46] W. D. Kingery, H. K. Bowen, and D. R. Uhlmann, *Introduction to Ceramics*, 2nd ed. New York, NY: Wiley, 1976.

[47] P. G. Klemens, "Phonon scattering by oxygen vacancies in ceramics," *Phys. B*, vol. 263-264, pp. 102-104, 1999, doi: 10.1016/S0921-4526(98)01202-2.

[48] A. G. Evans, D. R. Clarke, and C. G. Levi, "The influence of oxides on the performance of advanced gas turbines," *J. Eur. Ceram. Soc.*, vol. 28, pp. 1405–1419, 2008, doi: 10.1016/j.jeurceramsoc.2007.12.023.

[49] J. R. Brandon and R. Taylor, "Phase stability of zirconia-based thermal barrier coatings. Part I: Zirconia–yttria alloys," *Surf. Coat. Technol.*, vol. 46, pp. 75–90, 1991, doi: 10.1016/0257-8972(91)90151-L.

[50] R. Vassen, X. Cao, F. Tietz, D. Basu, and D. Stöver, "Zirconates as new materials for thermal barrier coatings," *J. Amer. Ceram. Soc.*, vol. 83, pp. 2023–2028, 2000, doi: 10.1111/j.1151-2916.2000.tb01506.x.

[51] M. A. Helminiak, “Factors Affecting the Lifetime of Thick Air Plasma Sprayed Thermal Barrier Coatings,” M.S. thesis, Fac. Swanson Sch. Eng., Pittsburgh, PA, 2008. [Online]. Available: http://d-scholarship.pitt.edu/id/eprint/6586.

[52] R. A. Miller, J. L. Smialek and R. G. Garlick, "Phase stability in plasma-sprayed partially stabilized zirconia yttria," in *Proc. First Int. Conf. Sci. Technol. Zirconia*, 1981, pp. 241-253.

[53] E.C. Subbarao, “Zirconia - an overview,” *Adv. Ceram.*, vol. 1, pp. 1-24, 1981.

[54] S. Krämer, J. Yang, C. G. Levi, and C. A. Johnson, "Thermochemical interaction of thermal barrier coatings with molten CaO–MgO–Al_2O_3–SiO_2 (CMAS) deposits," *J. Amer. Ceram. Soc.*, vol. 89, pp. 3167–3175, 2006, doi: 10.1111/j.1551-2916.2006.01209.x.

[55] G. Witz, V. Shklover, W. Steurer, S. Bachegowda, and H. P. Bossmann, "Phase evolution in yttria-stabilized zirconia thermal barrier coatings studied by Rietveld refinement of X-ray powder diffraction patterns," *J. Amer. Ceram. Soc.*, vol. 90, pp. 2935–2940, 2007, doi: 10.1111/j.1551-2916.2007.01785.x.

[56] P. Li, I.-W. Chen, and J. E. Penner-Hahn, "Effect of dopants on zirconia stabilization—An X-ray absorption study: I, trivalent dopants," *J. Amer. Ceram. Soc.*, vol. 77, pp. 118–128, 1994, doi: 10.1111/j.1151-2916.1994.tb06964.x.

[57] R. H. J. Hannink, P. M. Kelly, and B. C. Muddle, "Transformation toughening in zirconia-containing ceramics," *J. Amer. Ceram. Soc.*, vol. 83, pp. 461–487, 2000, doi: 10.1111/j.1151-2916.2000.tb01221.x.

[58] A. Heuer, R. Chaim, and V. Lanteri, "Review: Phase transformations and microstructural characterization of alloys in the system Y_2O_3–ZrO_2," *Adv. Ceram.*, vol. 24, pp. 3-17, 1988.

[59] C. Mercer, J. R. Williams, D. R. Clarke, and A. G. Evans, "On a ferroelastic mechanism governing the toughness of metastable tetragonal-prime (t′) yttria-stabilized zirconia," in *Proc. R. Soc. A*, vol. 463, pp. 1393–1408, 2007, doi: 10.1098/rspa.2007.1829.

[60] J. L. Smialek and R. A. Miller, "Revisiting the birth of 7YSZ thermal barrier coatings: Stephan Stecura," *Coatings*, vol. 8, 2018, Art. no. 255, doi: 10.3390/coatings8070255.

[61] R. Vaßen, M. O. Jarligo, T. Steinke, D. E. Mack, and D. Stöver, "Overview on advanced thermal barrier coatings," *Surf. Coat. Technol.*, vol. 205, pp. 938–942, 2010, doi: 10.1016/j.surfcoat.2010.08.151.

[62] X. Q. Cao, R. Vassen, and D. Stoever, "Ceramic materials for thermal barrier coatings," *J. Eur. Ceram. Soc.*, vol. 24, pp. 1–10, 2004, doi: 10.1016/S0955-2219(03)00129-8.

[63] S. Raghavan, H. Wang, R. B. Dinwiddie, W. D. Porter, R. Vaßen, D. Stöver, and M. J. Mayo, "Ta_2O_5/Nb_2O_5 and Y_2O_3 co-doped zirconias for thermal barrier coatings," *J. Amer. Ceram. Soc.*, vol. 87, pp. 431–437, 2004, doi: 10.1111/j.1551-2916.2004.00431.x.

[64] T. A. Schaedler, R. M. Leckie, S. Krämer, A. G. Evans, and C. G. Levi, "Toughening of nontransformable t′-YSZ by addition of titania," *J. Amer. Ceram. Soc.*, vol. 90, pp. 3896–3901, 2007, doi: 10.1111/j.1551-2916.2007.01990.x.

[65] S. Raghavan, H. Wang, R. B. Dinwiddie, W. D. Porter, and M. J. Mayo, "The effect of grain size, porosity and yttria content on the thermal conductivity of nanocrystalline zirconia," *Scr. Mater.*, vol. 39, pp. 1119–1125, 1998, doi: 10.1016/S1359-6462(98)00290-5.

[66] P. G. Klemens and M. Gell, "Thermal conductivity of thermal barrier coatings," *Mater. Sci. Eng. A*, vol. 245, pp. 143–149, 1998, doi: 10.1016/S0921-5093(97)00846-0.

[67] J. Wu, X. Wei, N. P. Padture, P. G. Klemens, M. Gell, E. García, P. Miranzo, and M. I. Osendi, "Low-thermal-conductivity rare-earth zirconates for potential thermal-barrier-coating applications," *J. Amer. Ceram. Soc.*, vol. 85, pp. 3031–3035, 2002, doi: 10.1111/j.1151-2916.2002.tb00574.x.

[68] A. K. Bhattacharya, V. Shklover, W. Steurer, G. Witz, H. P. Bossmann, and O. Fabrichnaya, "Ta_2O_5–Y_2O_3–ZrO_2 system: Experimental study and preliminary thermodynamic description," *J. Eur. Ceram. Soc.*, vol. 31, pp. 249–257, 2011, doi: 10.1016/j.jeurceramsoc.2010.09.009.

[69] D. Wu, Y. Yao, X. Shan, F. Yang, X. Zhao, and P. Xiao, "Equimolar $YO_{1.5}$ and $TaO_{2.5}$ co-doped ZrO_2 as a potential CMAS-resistant material for thermal barrier coatings," *J. Amer. Ceram. Soc.*, vol. 104, pp. 1132–1145, 2021, doi: 10.1111/jace.17514.

[70] A. M. Limarga, S. Shian, R. M. Leckie, C. G. Levi, and D. R. Clarke, "Thermal conductivity of single- and multi-phase compositions in the ZrO_2–Y_2O_3–Ta_2O_5 system," *J. Eur. Ceram. Soc.*, vol. 34, pp. 3085–3094, 2014, doi: 10.1016/j.jeurceramsoc.2014.03.013.

[71] C. A. Macauley, A. N. Fernandez, J. S. Van Sluytman, and C. G. Levi, "Phase equilibria in the ZrO_2–$YO_{1.5}$–$TaO_{2.5}$ system at 1250 °C," *J. Eur. Ceram. Soc.*, vol. 38, pp. 4523–4532, 2018, doi: 10.1016/j.jeurceramsoc.2018.06.010.

[72] S. Shian, P. Sarin, M. Gurak, M. Baram, W. M. Kriven, and D. R. Clarke, "The tetragonal–monoclinic, ferroelastic transformation in yttrium tantalate and effect of zirconia alloying," *Acta Mater.*, vol. 69, pp. 196–202, 2014, doi: 10.1016/j.actamat.2014.01.054.

[73] C. Laberty-Robert, F. Ansart, C. Deloget, M. Gaudon, and A. Rousset, "Dense yttria stabilized zirconia: Sintering and microstructure," *Ceram. Int.*, vol. 29, pp. 151–158, 2003, doi: 10.1016/S0272-8842(02)00099-8.

[74] D. Baither, M. Bartsch, B. Baufeld, A. Tikhonovsky, A. Foitzik, M. Rühle, and U. Messerschmidt, "Ferroelastic and plastic deformation of t′-zirconia single crystals," *J. Amer. Ceram. Soc.*, vol. 84, pp. 1755–1762, 2001, doi: 10.1111/j.1151-2916.2001.tb00911.x.

[75] A. H. Heuer, "Transformation toughening in ZrO_2-containing ceramics," *J. Amer. Ceram. Soc.*, vol. 70, pp. 689–698, 1987, doi: 10.1111/j.1151-2916.1987.tb04865.x.

[76] A. V. Virkar, "Role of ferroelasticity in toughening of zirconia ceramics," Key Eng. Mater., vols. 153–154, pp. 183–210, 1998, doi: 10.4028/www.scientific.net/KEM.153-154.183.

[77] E. Bakan and R. Vaßen, "Ceramic top coats of plasma-sprayed thermal barrier coatings: Materials, processes, and properties," *J. Therm. Spray Technol.*, vol. 26, pp. 992–1010, 2017, doi: 10.1007/s11666-017-0597-7.

[78] C. Suryanarayana, "Mechanical alloying and milling," *Prog. Mater. Sci.*, vol. 46, pp. 1-184, 2001, doi: 10.1016/S0079-6425(99)00010-9.

[79] V. K. Vaishnavi, A. Dasgupta, C. Ghosh, and S. K. Sinha, "Analysis of structural transformation in nanocrystalline Y_2O_3 during high energy ball milling," *J. Alloys Compd.*, vol. 900, 2022, Art. no. 163550, doi: 10.1016/j.jallcom.2021.163550.

[80] R. Cuenca Alvarez, “Contribution à l’élaboration de dépôts composites par projection plasma d’arc de poudres élaborées par mecanofusion”, Ph.D. thesis, Faculté Sci. Univ. de Limoges, France, 2003. [Online].

[81] M. H. Staia, S. Kossman, V. Contreras, D. Chicot, A. Iost, and A. Van Gorp, " Recubrimientos nanoestructurados de circonia estabilizada con itria (YSZ) depositados mediante termorrociado por plasma por suspensión," *Bol. Soc. Esp. Ceram. Vidrio*, vol. 58, pp. 151–160, 2019, doi: 10.1016/j.bsecv.2018.10.003.

[82] L. K. Wei, S. Z. Abd Rahim, M. M. Al Bakri Abdullah, A. T. M. Yin, M. F. Ghazali, M. F. Omar, O. Nemeș, A. V. Sandu, P. Vizureanu, and A. E. Hadj Abdellah, "Producing metal powder from machining chips using ball milling process: A review," *Mater.*, vol. 16, 2023, Art. no. 4635, doi: 10.3390/ma16134635.

[83] Retsch, *The Art of Milling – An Expert Guide to Neutral-to-Analysis Size Reduction and Homogenization in the Laboratory*. (2017). [Online]. Available: https://www.retsch.com/files/5771/expert-guide-milling.pdf.

[84] C.-J. Chan, F. F. Lange, M. Rühle, J.-F. Jue, and A. V. Virkar, "Ferroelastic domain switching in tetragonal zirconia single crystals—Microstructural aspects," *J. Amer. Ceram. Soc.*, vol. 74, pp. 807–813, 1991, doi: 10.1111/j.1151-2916.1991.tb06929.x.

[85] D. R. Clarke and C. G. Levi, "Materials design for the next generation thermal barrier coatings," *Annu. Rev. Mater. Res.*, vol. 33, pp. 383–417, 2003, doi: 10.1146/annurev.matsci.33.011403.113718.

[86] R. Vaßen, E. Bakan, D. E. Mack, and O. Guillon, "A perspective on thermally sprayed thermal barrier coatings: Current status and trends," *J. Therm. Spray Technol.*, vol. 31, pp. 685–698, 2022, doi: 10.1007/s11666-022-01330-2.

[87] Z. Y. Wei, G. H. Meng, L. Chen, G. R. Li, M. J. Liu, W. X. Zhang, L. N. Zhao, Q. Zhang, X. D. Zhang, C. L. Wan, Z. X. Qu, L. Chen, J. Feng, L. Liu, H. Dong, Z. B. Bao, X. F. Zhao, X. F. Zhang, L. Guo, L. Wang, B. Cheng, W. W. Zhang, P. Y. Xu, G. J. Yang, H. N. Cai, H. Cui, Y. Wang, F. X. Ye, Z. Ma, W. Pan, M. Liu, K. S. Zhou, and C. J. Li, "Progress in ceramic materials and structure design toward advanced thermal barrier coatings," *J. Adv. Ceram.*, vol. 11, pp. 985–1068, 2022, doi: 10.1007/s40145-022-0581-7.

[88] Y. Yamazaki, "Correlation between the mechanical properties and splat microstructures of an air plasma sprayed thermal barrier coating," *J. Solid Mech. Mater. Eng.*, vol. 2, pp. 1275–1286, 2008, doi: 10.1299/jmmp.2.1275.

[89] M. Gupta, “Design of Thermal Barrier Coatings A modelling approach,” Ph.D. thesis, Univ. West, Trollhättan, Sweden, 2014. [Online]. Available: https://api.semanticscholar.org/CorpusID:29086039.

[90] P. G. Montavon, “Elaboration de dépôts à gradients de propriétés par projection plasma de suspension de particules submicroniques,” Ph.D. thesis, Faculté Sci. Tech., Univ. de Limoges, France, 2008. [Online]. Available: https://theses.fr/2008limo4071.

[91] X. Ma and P. Ruggiero, "Practical aspects of suspension plasma spray for thermal barrier coatings on potential gas turbine components," *J. Therm. Spray Technol.*, vol. 27, pp. 591–602, 2018, doi: 10.1007/s11666-018-0700-8.

[92] O. Tingaud, R. Etchart-Salas, V. Rat, J.-F. Coudert, H. Ageorges, A. Grimaud, A. Denoirjean, P. Fauchais, G. Montavon, and S. Alexandre, "Suspension plasma spraying of zirconia coatings: Process and coating structure," presented at the 18th Int. Symp. Plasma Chem., Kyoto, Japan, Aug. 2007. Paper hal-00262292.

[93] K. Vanevery, M. J. M. Krane, R. W. Trice, H. Wang, W. Porter, M. Besser, D. Sordelet, J. Ilavsky, and J. Almer, "Column formation in suspension plasma-sprayed coatings and resultant thermal properties," *J. Therm. Spray Technol.*, vol. 20, pp. 817–828, 2011, doi: 10.1007/s11666-011-9632-2.

[94] L. Pawlowski, "Suspension and solution thermal spray coatings," *Surf. Coat. Technol.*, vol. 203, pp. 2807–2829, 2009, doi: 10.1016/j.surfcoat.2009.03.005.

[95] O. Aranke, M. Gupta, N. Markocsan, X. H. Li, and B. Kjellman, "Microstructural evolution and sintering of suspension plasma-sprayed columnar thermal barrier coatings," *J. Therm. Spray Technol.*, vol. 28, pp. 198–211, 2019, doi: 10.1007/s11666-018-0778-z.

[96] A. Ganvir, N. Curry, S. Björklund, N. Markocsan, and P. Nylén, "Characterization of microstructure and thermal properties of YSZ coatings obtained by axial

suspension plasma spraying (ASPS)," *J. Therm. Spray Technol.*, vol. 24, pp. 1195–1204, 2015, doi: 10.1007/s11666-015-0263-x.

[97] S. Lokachari, K. Leng, A. Rincon Romero, N. Curry, G. Brewster, A. Norton, and T. Hussain, "Processing–microstructure–properties of columns in thermal barrier coatings: A study of thermo-chemico-mechanical durability," *ACS Appl. Mater. Interfaces*, vol. 16, pp. 10646–10660, 2024, doi: 10.1021/acsami.3c16681.

[98] B. Bernard, A. Quet, L. Bianchi, A. Joulia, A. Malié, V. Schick, and B. Rémy, "Thermal insulation properties of YSZ coatings: Suspension plasma spraying (SPS) versus electron beam physical vapor deposition (EB-PVD) and atmospheric plasma spraying (APS)," *Surf. Coat. Technol.*, vol. 318, pp. 122–128, 2017, doi: 10.1016/j.surfcoat.2016.06.010.

[99] Y. Zhao, L. Wang, J. Yang, D. Li, X. Zhong, H. Zhao, F. Shao, and S. Tao, "Thermal aging behavior of axial suspension plasma-sprayed yttria-stabilized zirconia (YSZ) thermal barrier coatings," *J. Therm. Spray Technol.*, vol. 24, pp. 338–347, 2015, doi: 10.1007/s11666-014-0206-y.

[100] B. H. Toby, "R factors in Rietveld analysis: How good is good enough?," *Powder Diffr.*, vol. 21, pp. 67–70, 2006, doi: 10.1154/1.2179804.

[101] L. B. McCusker, R. B. Von Dreele, D. E. Cox, D. Louër, and P. Scardi, "Rietveld refinement guidelines," *J. Appl. Crystallogr.*, vol. 32, pp. 36–50, 1999, doi: 10.1107/S0021889898009856.

[102] W. C. Oliver and G. M. Pharr, "An improved technique for determining hardness and elastic modulus using load and displacement sensing indentation experiments," *J. Mater. Res.*, vol. 7, no. 6, pp. 1564–1583, 1992, doi: 10.1557/JMR.1992.1564.

[103] J. S. Field, M. V. Swain, and R. D. Dukino, "Determination of fracture toughness from the extra penetration produced by indentation-induced pop-in," *J. Mater. Res.*, vol. 18, pp. 1412–1419, 2003, doi: 10.1557/JMR.2003.0194.

[104] G. Kühn and O. Kubaschewski, “Metallurgical thermochemistry,” in *Kristall. Tech.*, vol. 24, Oxford, U.K.: Pergamon Press, 1979.

[105] C. E. Wicks and F. E. Block, “Thermodynamic Properties of 65 Elements: Their Oxides, Halides, Carbides and Nitrides.”, *U.S. Dept. Int.*, Bull. no. 605, 1963. Available: https://digital.library.unt.edu/ark:/67531/metadc12759/.

[106] C. Ruelle, S. Goutier, V. Rat, A. Keromnes, C. Chazelas, and É. Meillot, “Study of the electric arc dynamics in a cascaded-anode plasma torch,” *Surf. Coat. Technol.*, vol. 462, 2023, Art. no. 129493, doi: 10.1016/j.surfcoat.2023.129493

[107] SinplexPro Universal Plasma Spray Guns - Product Data Sheet, Oerlikon Metco, DSE-0061.7, 2021.

[108] R. Zhukovskii, C. Chazelas, V. Rat, A. Vardelle, and R. Molz, "Model of a non-transferred arc cascaded-anode plasma torch: The two-temperature

formulation," *J. Phys. D: Appl. Phys.*, vol. 55, 2022, Art. no. 105201, doi: 10.1088/1361-6463/ac2cec.

[109] N. Terao, "Structure des oxides de tantale," *Jpn. J. Appl. Phys.*, vol. 6, no. 1, pp. 21–34, 1966.

[110] T. Ikeya and M. Senna, "Change in the structure during amorphization and crystallization of Ta_2O_5 under mechanical stressing. A comparative study with Nb2O5," *J. Non-Cryst. Solids*, vol. 113, pp. 51–57, 1989.

[111] D. Gouvêa, "Thermodynamic of solid-state sintering: Contributions of grain boundary energy," *J. Eur. Ceram. Soc.*, vol. 44, 2024, Art. no. 116677, doi: 10.1016/j.jeurceramsoc.2024.116677.

[112] W. S. Eldesouky, A. Abd El-Kareem, H. M. Abd El-Aziz, and E. S. Mosa, "Preparation and stabilization of monoclinic zirconia by yttria through mechanical alloying," *Arab J. Nucl. Sci. Appl.*, vol. 56, pp. 166–174, 2023, doi: 10.21608/AJNSA.2022.161293.1634.

[113] A. Sari, M. Keddam, and A. Guittoum, "Effect of iron impurity on structural development in ball-milled ZrO_2–3 mol% Y_2O_3," *Ceram. Int.*, vol. 41, pp. 1121–1128, 2015, doi: 10.1016/j.ceramint.2014.09.038.

[114] C. Luo, C. Li, K. Cao, J. Li, J. Luo, Q. Zhang, Q. Q. Zhou, F. Zhang, L. Gu, L. Yang, and Y. Zhou, "Ferroelastic domain identification and toughening mechanism for yttrium tantalate–zirconium oxide," *J. Mater. Sci. Technol.*, vol. 127, pp. 78–88, 2022, doi: 10.1016/j.jmst.2022.04.007.

[115] J. A. Krogstad, M. Lepple, Y. Gao, D. M. Lipkin, and C. G. Levi, "Effect of yttria content on the zirconia unit cell parameters," *J. Amer. Ceram. Soc.*, vol. 94, pp. 4548–4555, 2011, doi: 10.1111/j.1551-2916.2011.04862.x.

[116] M. F. R. P. Alves, L. Q. B. de Campos, B. G. Simba, C. R. M. da Silva, K. Strecker, and C. dos Santos, "Microstructural characteristics of 3Y-TZP ceramics and their effects on the flexural strength," *Ceramics*, vol. 5, pp. 798–813, 2022, doi: 10.3390/ceramics5040058.

[117] J. Rios, A. Restrepo, A. Zuleta, F. Bolívar, J. Castaño, and E. Correa, "Effect of ball size on the microstructure and morphology of Mg powders processed by high-energy ball milling," *Metals*, vol. 11, 2021, Art. no. 1621, doi: 10.3390/met11101621.

[118] D. Chen, J. Lu, C. Sun, Q. Wang, and X. Ning, "Microstructure and thermal cycling behavior of Ta_2O_5 and Y_2O_3 co-doped ZrO_2 coatings," *J. Therm. Spray Technol.*, vol. 32, pp. 1327–1337, 2023, doi: 10.1007/s11666-022-01525-7.

[119] T.A. Schaedler, “Phase Evolution in the $YO_{1.5}$-TiO_2-ZrO_2 System and Effects on Ionic Conductivity and Toughness,” Ph.D. dissertation, Univ. of Calif., Santa Barbara, CA, 2006.

[120] A. V. Virkar and R. L. K. Matsumoto, "Ferroelastic domain switching as a toughening mechanism in tetragonal zirconia," *J. Amer. Ceram. Soc.*, vol. 69, no. 10, 1986, Art. no. 1986, doi: 10.1111/j.1151-2916.1986.tb07341.x.

[121] X. Niu, M. Xie, F. Zhou, R. Mu, X. Song, and S. An, "Substituent influence of yttria by gadolinia on the tetragonal phase stability for Y_2O_3–Ta_2O_5–ZrO_2 ceramics at 1300 °C," *J. Mater. Sci. Technol.*, vol. 30, pp. 381–386, 2014, doi: 10.1016/j.jmst.2013.12.008.

[122] A. Naumenko, N. Berezovska, M. Biliy, and O. V. Shevchenko, "Vibrational analysis and Raman spectra of tetragonal zirconia," Phys. Chem. Solid State, vol. 9, pp. 121-125, 2008.

[123] O. V. Rambadey, M. Gupta, A. Kumar, and P. R. Sagdeo, "Analysis of structural disorder on Raman spectra of semiconductors," *J. Appl. Phys.*, vol. 133, 2023, Art. no. 131101, doi: 10.1063/5.0145442.

[124] C. Barrett, Z. Stein, J. Hernandez, R. Naraparaju, U. Schulz, L. Tetard, and S. Raghavan, "Detrimental effects of sand ingression in jet engine ceramic coatings captured with Raman-based 3D rendering," *J. Eur. Ceram. Soc.*, vol. 41, pp. 1664–1671, 2021, doi: 10.1016/j.jeurceramsoc.2020.09.050.

[125] *Hysitron TI 950 TriboIndenter® User Manual,* Hysitron Inc., Minneapolis, MN, 2015.

[126] J. Muñoz-Saldaña, M. J. Hoffmann, and G. A. Schneider, "Ferroelectric domains in coarse-grained lead zirconate titanate ceramics characterized by scanning force microscopy," *J. Mater. Res.*, vol. 18, pp. 1777–1784, 2003, doi: 10.1557/JMR.2003.0247.

[127] B. R. Lawn, A. G. Evans, and D. B. Marshall, "Elastic/plastic indentation damage in ceramics: The median/radial crack system," *J. Amer. Ceram. Soc.*, vol. 63, pp. 574–581, 1980, doi: 10.1111/j.1151-2916.1980.tb10768.x.

[128] M. R. Winter and D. R. Clarke, "Thermal conductivity of yttria-stabilized zirconia–hafnia solid solutions," *Acta Mater.*, vol. 54, pp. 5051–5059, 2006, doi: 10.1016/j.actamat.2006.06.038.

[129] P. Fauchais, M. Fukumoto, A. Vardelle, and M. Vardelle, "Knowledge concerning splat formation: An invited review," *J. Therm. Spray Technol.*, vol. 13, pp. 337–360, 2004, doi: 10.1361/10599630419670.

[130] H.-U. Hummel, R. Fackler, and P. Remmert, "Tantaloxide durch Gasphasenhydrolyse, Druckhydrolyse und Transportreaktion aus 2H-TaS_2: Synthesen von TT-Ta_2O_5 und T-Ta_2O_5 und Kristallstruktur von T-Ta_2O_5," *Chem. Ber.*, vol. 125, pp. 551–556, 1992, doi: 10.1002/cber.19921250304.

[131] A. Fert, "Structure de quelques oxydes de terres rares," *Bull. Soc. Fr. Minéralogie Cristallogr.*, vol. 85, pp. 267–270, 1962, doi: 10.3406/bulmi.1962.5577.

[132] R. E. Hann, P. R. Suitch, and J. L. Pentecost, "Monoclinic crystal structures of ZrO_2 and HfO_2 refined from X-ray powder diffraction data," *J. Amer. Ceram. Soc.*, vol. 68, pp. C-285–C-286, 1985, doi: 10.1111/j.1151-2916.1985.tb11534.x.

[133] N. Igawa and Y. Ishii, "Crystal structure of metastable tetragonal zirconia up to 1473 K," *J. Amer. Ceram. Soc.*, vol. 84, pp. 1169–1171, 2001, doi: 10.1111/j.1151-2916.2001.tb00808.x.

[134] C. A. Macauley, “Phase Equilibria and Toughness of Zirconia-Based Thermal Barrier Coatings,” Ph.D. dissertation, Univ. of California, Santa Barbara, CA, 2016.

[135] A. Loganathan and A. S. Gandhi, "Effect of high-temperature aging on the fracture toughness of ytterbia-stabilized t′ zirconia," *Scr. Mater.*, vol. 67, pp. 285–288, 2012, doi: 10.1016/j.scriptamat.2012.05.001.

[136] D. Wang, Y. Guo, K. Liang, and K. Tao, "Crystal structure of zirconia by Rietveld refinement," *Sci. China Ser. A Math.*, vol. 42, pp. 80–86, 1999, doi: 10.1007/BF02872053.

[137] D. Asmi and I. M. Low, “Manufacture of graded ceramic matrix composites using infiltration techniques,” in *Adv. Ceram. Matrix Compos.*, Cambridge, UK: Woodhead Publishing, 2014, pp. 109–140, doi: 10.1533/9780857098825.1.109.

ANNEXES

ANNEX 1

1. Methodology

1.1. XRD pattern analysis by Rietveld Method

$$\chi^2(GOF) = R_{wp}^2 / R_{exp}^2 \quad (\text{Eq. S1})$$

Where, for phase analysis, values of GOF less than 4 are acceptable to consider a good fit of the model to the data [137].

The values of R_{wp}^2 and R_{exp}^2 are estimates using Eq. S2 and S3

$$R_{wp}^2 = \sum_i w_i (y_{C,i} - y_{O,i})^2 / \sum_i w_i (y_{O,i})^2 \quad (\text{Eq. S2})$$

$$R_{exp}^2 = N / \sum_i w_i (y_{O,i})^2 \quad (\text{Eq. S3})$$

Where R_{wp} is the weighted profile R-factor, R_{exp} is the expected R factor, $y_{C,i}$, are the intensity values simulated by the model (with C indicating computed values), $y_{O,i}$, are the observed intensity values, w_i is the weight ($w_i = 1/\sigma^2[y_{O,i}]$), and N is the number of data points [100].

Table A1.1.1 Structural information used for the Rietveld refinement

Crystal system	**ZrO_2 Tetragonal** [133]	**ZrO_2 Cubic (Doped)** [136]	**ZrO_2 Monoclinic** [132]	**Ta_2O_5, Orthorhombic** [130]	**Y_2O_3 Cubic** [131]
Space group	P 42/n m c	F m -3 m	P 1 21/c 1	P m m 2	I a -3
Space group number	137	225	14	25	206
a (Å)	3.612	5.135	5.151	3.894	10.5500
b (Å)	3.612	5.135	5.203	43.997	10.5500
c (Å)	5.212	5.135	5.316	6.209	10.5500
Alpha (°)	90	90	90	90	90
Beta (°)	90	90	99.196	90	90
Gamma (°)	90	90	90	90	90

Table A1.1.2 Modified structural information for 16YTZ, according to ZrO_2 tetragonal [133]

No.	**Name**	**Elem.**	**X**	**Y**	**Z**	**Biso**	**sof**	**Wyck.**
1	O1	O	0.25	0.25	0.049	1.84	1	4d
2	ZR1	Zr	0.75	0.25	0.25	0.993	0.68	2b
3	Y1	Y	0.75	0.25	0.25	0.993	0.16	2b
4	TA1	Ta	0.75	0.25	0.25	0.993	0.16	2b

Table A1.1.3 Structural information for ZrO_2, Cubic (Y-Doped) [136]

No.	Name	Elem.	X	Y	Z	Biso	sof	Wyck.
1	O1	O	0.25	0.25	0.25	1.57	1	8c
2	ZR1	Zr	0	0	0	0.72	1	4a

Table A1.1.4 Structural information for ZrO_2, Monoclinic [132]

No.	Name	Elem.	X	Y	Z	Biso	sof	Wyck.
1	O1	O	0.5509	0.2548	0.0173	7	1	4e
2	O2	O	0.063	0.3289	0.3476	7	1	4e
3	ZR1	Zr	0.2742	0.0389	0.2095	7	1	4e

Table A1.1.5 Structural information for Y_2O_3. Cubic [131]

No.	Name	Elem.	X	Y	Z	Biso	sof	Wyck.
1	O1	O	0.1	0.361	0.127	0.5	1	48e
2	Y1	Y	0.2814	0	0.25	0.5	1	24d
3	Y2	Y	0	0	0	0.5	1	8a

Table A1.1.6 Structural information for Ta_2O_5, Orthorhombic [130]

No.	Name	Elem.	X	Y	Z	Biso	sof	Wyck.
1	TA1	Ta	0	0.2909	0.5151	0.5	1	2g
2	O1	O	0.5	0.119	0.518	0.5	1	2h
3	O2	O	0.5	0.045	0.409	0.5	1	2h
4	O3	O	0.5	0.5	0.009	0.5	1	1d
5	O4	O	0.5	0.419	0.026	0.5	1	2h
6	O5	O	0.5	0.332	0.046	0.5	1	2h
7	O6	O	0.5	0.256	0.951	0.5	1	2h
8	O7	O	0.5	0.17	0.036	0.5	1	2h
9	O8	O	0.5	0.078	0.023	0.5	1	2h
10	O9	O	0.5	0	0.005	0.5	1	1c
11	TA2	Ta	0	0	0	0.5	1	1a
12	TA3	Ta	0	0.3779	0.5228	0.5	1	2g
13	O10	O	0.5	0.381	0.502	0.5	1	2h
14	TA4	Ta	0	0.2073	0.546	0.5	1	2g
15	TA5	Ta	0	0.1196	0.5552	0.5	1	2g
16	TA6	Ta	0	0.043	0.4654	0.5	1	2g
17	TA7	Ta	0	0.5	0.0123	0.5	1	1b
18	TA8	Ta	0	0.4136	0.0467	0.5	1	2g
19	TA9	Ta	0	0.3314	0.0603	0.5	1	2g
20	TA10	Ta	0	0.254	0.9548	0.5	1	2g
21	TA11	Ta	0	0.1643	0.0451	0.5	1	2g
22	TA12	Ta	0	0.0786	0.013	0.5	1	2g
23	TA13	Ta	0	0.4569	0.551	0.5	1	2g
24	O11	O	0	0.198	0.256	0.5	0.9474	2g
25	O12	O	0	0.5	0.712	0.5	0.9474	1b

Table A1.1.6 Structural information for Ta_2O_5, Orthorhombic [130] (*cont.*)

No.	Name	Elem.	X	Y	Z	Biso	sof	Wyck.
26	O13	O	0	0.463	0.162	0.5	0.9474	2g
27	O14	O	0	0.419	0.37	0.5	0.9474	2g
28	O15	O	0	0.415	0.724	0.5	0.9474	2g
29	O16	O	0	0.375	0.197	0.5	0.9474	2g
30	O17	O	0	0.341	0.726	0.5	0.9474	2g
31	O18	O	0	0.331	0.372	0.5	0.9474	2g
32	O19	O	0	0.296	0.834	0.5	0.9474	2g
33	O20	O	0	0.273	0.242	0.5	0.9474	2g
34	O21	O	0.5	0.211	0.51	0.5	1	2h
35	O22	O	0	0.213	0.87	0.5	0.9474	2g
36	O23	O	0.5	0.307	0.531	0.5	1	2h
37	O24	O	0	0.159	0.359	0.5	0.9474	2g
38	O25	O	0	0.04	0.132	0.5	0.9474	2g
39	O26	O	0	0.081	0.321	0.5	0.9474	2g
40	O27	O	0	0.124	0.131	0.5	0.9474	2g
41	O28	O	0	0.161	0.732	0.5	0.9474	2g
42	O29	O	0	0.08	0.681	0.5	0.9474	2g
43	O30	O	0	0	0.327	0.5	0.95	1a
44	O31	O	0	0	0.689	0.5	0.95	1a
45	O32	O	0.5	0.458	0.549	0.5	1	2h
46	O33	O	0	0.5	0.355	0.5	0.9474	1b
47	O34	O	0	0.25	0.601	0.5	0.9474	2g

1.2. Results

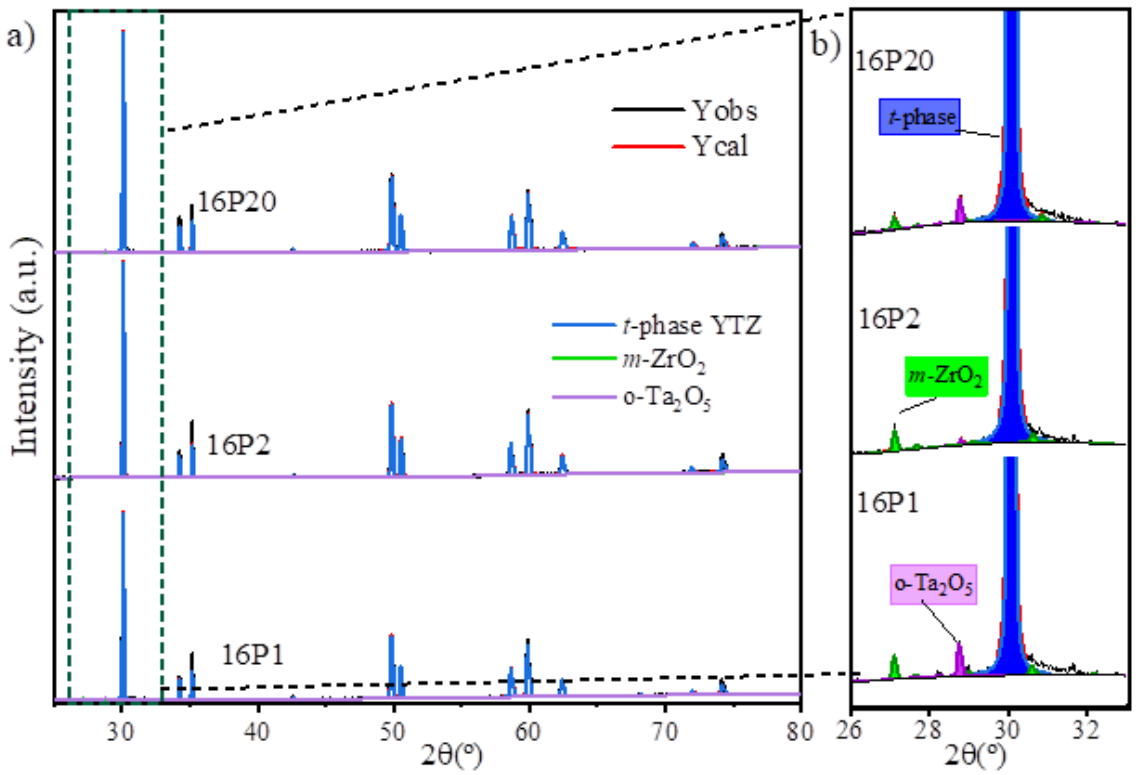


Figure A1.2.1 XRD patterns of the coatings obtained after adjusting using the Rietveld method

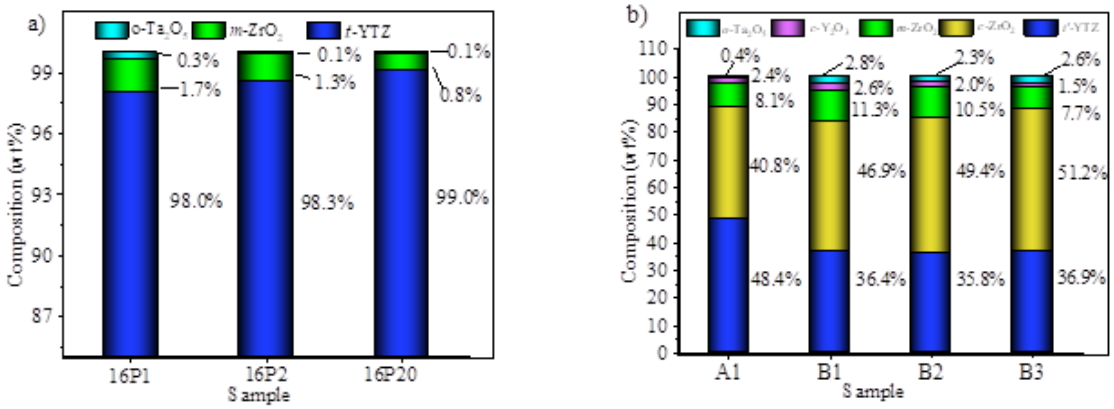


Figure A1.2.2 a) Phase quantification (wt.%) in dense ceramics, b) phase quantification (wt.%) in coatings obtained by Rietveld's method.

Table A1.2.1 Parameters obtained in Rietveld refinement for dense ceramics (16P1, 16P2 and 16P20) and for coatings (A1, B2, B2 and B3).

Sample	R_{exp}	R_{wp}	χ^2
16P1	3.0	8.3	7.6
16P2	2.9	8.7	9.0
16P20	2.9	8.3	8.0
A1	3.4	5.4	2.5
B1	3.4	4.7	1.9
B2	3.2	5.2	2.6
B3	3.6	4.8	1.8

ANNEX 2

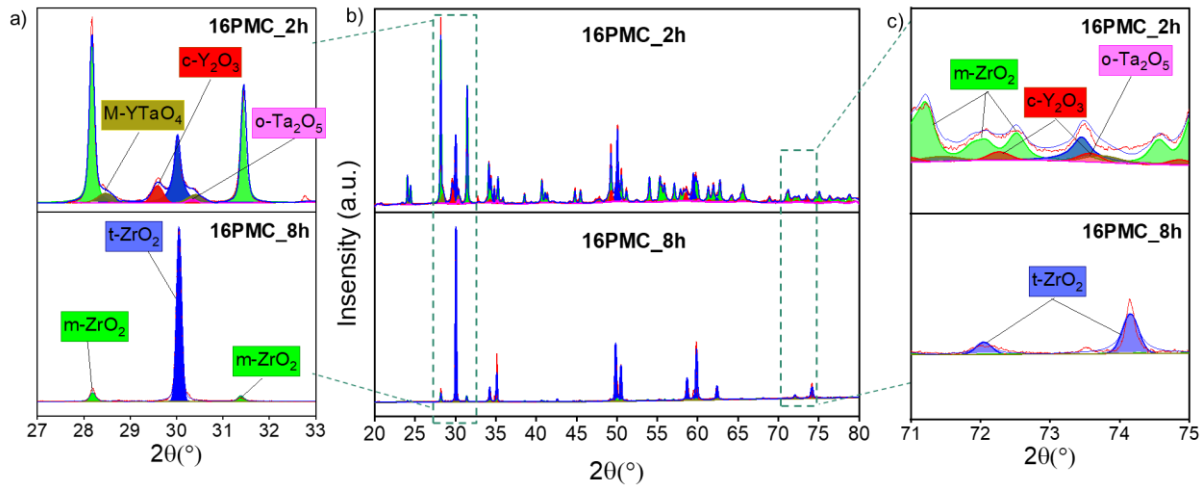


Figure A2.1 Phase composition evolution of 16YTZ after 2 and 8 h of sintering at 1500 °C. In section a) highlights the characteristic peaks between 2θ = 27.5° and 32.5° showing the evolution of the phase contributions between the two sintering times, b) X-ray diffraction patterns and Rietveld refinement results for the 16YTZ ceramic sintered at 1500 °C for 2 h (top) and 8 h (bottom). The color-coded curves correspond to the individual crystalline phases identified in the refinement: t-ZrO_2, m-ZrO_2, c-Y_2O_3, M-$YTaO_4$ and o-Ta_2O_5 and c) Deconvolution of last peaks in the region between 2θ = 71° and 75°, highlighting the presence of minority phases such as c-Y_2O_3, o-Ta_2O_5 and m-ZrO_2 after 2 h. The refinement of the complete XRD patterns confirms that even after 8 h of sintering, considerable quantity of monoclinic phase remain, indicating that full stabilization of the t′-phase has not yet been achieved under these conditions.

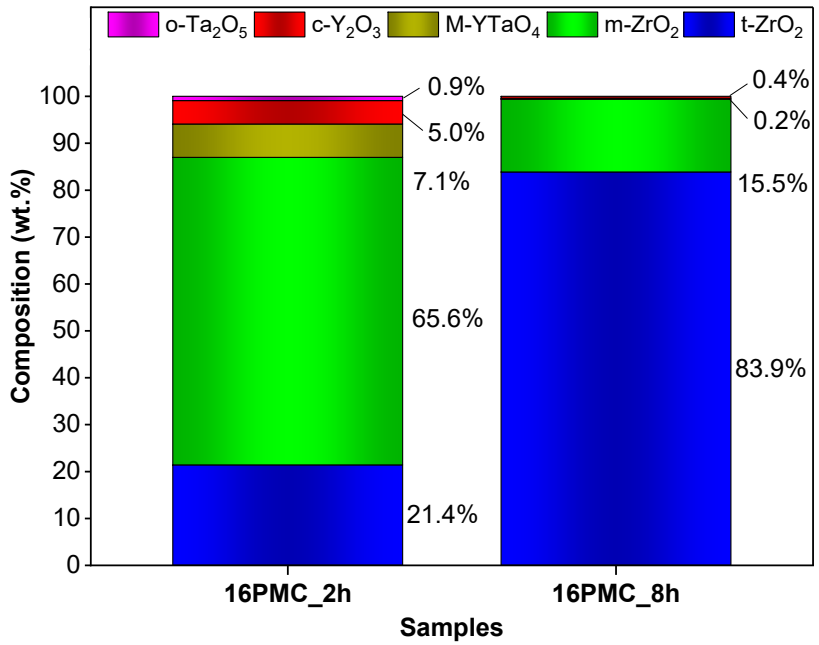


Figure A2.2 Phase quantification (wt.%) in powders sintered at 1500 °C for 2 h and 8 h, based on Rietveld refinement results. The identified crystalline phases include t-ZrO_2 (blue), m-ZrO_2 (green), c-Y_2O_3 (red), M-$YTaO_4$ (gold) and o-Ta_2O_5 (magenta).

Table A2.1 Mass percentages of each phase present in the 16YTZ composition after sintering at 2 and 8 h at 1500 °C.

(wt.%)	**t-ZrO_2**	**m-ZrO_2**	**o-Ta_2O_5**	**c-Y_2O_3**	**M-$YTaO_4$**
16PMC_2h	21.4	65.6	0.9	5.0	7.1
16PMC_8h	83.7	15.5	0.0	0.4	0.2

ANNEX 3

VITA OF MARIA CATALINA GALEANO CAMACHO

August 27, 1992 Born: Bogotá, Colombia

EDUCATION

2016 Bachelor of Mechanical Engineering

Libre University, Colombia

2019 Master's degree in Science of Materials

Centro de Investigación y de Estudios Avanzados del IPN – CINVESTAV, Mexico

2025 Doctorate of Philosophy in Science of Materials and Ceramics Materials and Surface Treatments

Centro de Investigación y de Estudios Avanzados del IPN – CINVESTAV, Mexico / University of Limoges, France

PROFESSIONAL EMPLOYMENT

2020-2021 Materials and Processes Engineer

Van Damme Heicopters, Inc. United States.

2021 Project Manager

Colombian Aerospace Industry Federation, Bogotá, Colombia

2022 "Delfín" Program Mentor, CENAPROT

Centro de Investigación y de Estudios Avanzados del IPN – CINVESTAV, Mexico (Summer)

2023 **"**Cordées de la Recherche" Program Mentor, IRCER

University of Limoges, France

2024 "Clubes de Ciencia" Program Mentor, Clubes de Ciencia México, Oaxaca Edition

Blaise Pascal Institute, Mexico

2024 Professor of Composite Materials

Libre Univeristy, Bogotá, Colombia (remote)

2025 Professor in Engineering

Arkansas State University, Campus Querétaro, Mexico

PUBLICATIONS

C. Galeano-Camacho, I. Bedoya-Trujillo, S. Pérez, H. Ageorges, and J. Muñoz-Saldaña, "Analysis of the t′ + c phase content from ZrO_2–16 mol.% Y_2O_3–16 mol.% Ta_2O_5 mechanoactivated powder mixtures in coatings deposited by suspension plasma spraying," *J. Therm. Spray Technol.*, vol. 34, pp. 783–794, 2025, doi: 10.1007/s11666-025-01946-0.

M. C. Galeano Camacho, H. Ageorges, and J. Muñoz-Saldaña, “Processing and Suspension Plasma Spray Deposition of ZrO_2-Based Ceramic Materials for Thermal Barrier Coatings,” in *Proc. Int. Thermal Spray Conf. (ITSC)*, 2024, pp. 75–82, doi: 10.31399/asm.cp.itsc2024p0075.

PRESENTATIONS

Galeano-Camacho, C. Ageorges, H., and Muñoz-Saldaña J., Synthesis and Characterization of Zirconia-Yttria-Tantala (YTZ) Ceramics for Thermal Barrier Coatings Applications, Presented at the International Materials Research Congress, Cancun, Mexico, August 2023. **Poster**

Galeano-Camacho, C. Ageorges, H., and Muñoz-Saldaña J., Synthèse et traitement de la poudre de Zircone-Yttria-Tantala (YTZ) comme matière première pour les dépôts par plasma de revêtements à barrière thermique, Presented at the Colloque Poudres et Matériaux Frittés, Le Creusot, France, December 2023. **Oral**

Galeano-Camacho, C. Ageorges, H., and Muñoz-Saldaña J., Processing and Suspension Plasma Spray Deposition of ZrO_2-Based Ceramic Materials for Thermal Barrier Coatings, Presented at the International Thermal Spray Conference, Milan, Italy, April 2024. **Oral**

Galeano-Camacho, C. Ageorges, H., and Muñoz-Saldaña J., Influence of spray parameters onto the physicochemical properties of Zirconia-Yttria-Tantala coatings deposited by SPS, Presented at the International Materials Research Congress, Cancun, Mexico, August 2024. **Oral**

Galeano-Camacho, C. Ageorges, H., and Muñoz-Saldaña J., Influencia de la distancia de rociado en las propiedades mecánicas, térmicas y microestructurales de recubrimientos de Zirconia-Itria-Tantala desarrollados mediante la técnica de plasma por suspensión - SPS, X National Symposium and III Latin American Meeting of Surface Engineering and Tribology 2024, Queretaro, Mexico, October 2024. **Oral**

Galeano-Camacho, C. Ageorges, H., and Muñoz-Saldaña J., Effect of Spray Distance on the Microstructure, Phase Transformation and Microhardness of ZrO_2-x$YO_{1.5}$-x$TaO_{2.5}$ (YTZ) Coatings Deposited by Suspension Plasma Spraying (SPS), Presented at the ASM Symposium: Navigating a Greener Sky, Limoges, France, November 2024. **Poster**